UC San Diego
UC San Diego Electronic Theses and Dissertations

Title
Suppression of Electronic Defects at the Oxide-SiGe Interface Using Intuitive and Counter-Intuitive Techniques

Permalink
https://escholarship.org/uc/item/7906m091

Author
Kavrik, Mahmut Sami

Publication Date
2019

Peer reviewed|Thesis/dissertation

UNIVERSITY OF CALIFORNIA SAN DIEGO

Suppression of Electronic Defects at the Oxide-SiGe Interface Using Intuitive and Counter Intuitive Techniques

A dissertation submitted in partial satisfaction of the requirements for the degree

Doctor of Philosophy

in

Materials Science and Engineering

by

Mahmut Sami Kavrik

Committee in Charge:

    Professor Andrew C. Kummel, Chair
    Professor Peter Asbeck
    Professor Prabhakar Bandaru
    Professor Brian Maple
    Professor Yuan Taur

2019

The dissertation of Mahmut Sami Kavrik is approved, and it is acceptable in quality and form for publication on microfilm and electronically:

_____

_____

_____

_____

_____

Chair

University of California, San Diego

2019

DEDICATION

To those who serve humanity

EPIGRAPH

It does not make sense!

TABLE OF CONTENTS

Investigation of Oxide/SiGe Interface with Advanced Characterization Techniques

LIST OF SYMBOLS AND ABBREVIATIONS

Å	angstrom
ALD	atomic layer deposition
AR-PES	Angular resolved photo emission spectroscopy
BE	binding energy
CB	conduction band
C_{max}	maximum capacitance
C-V	capacitance voltage
CVD	chemical vapor deposition
DFT	density functional theory
DI	deionized
D_{it}	density of interface traps
DOS	density of states
e	electron
E_f	Fermi level
EDS	Energy dispersive x-ray spectroscopy
EELS	Electron energy loss spectroscopy
ER-PES	Energy resolved photo emission spectroscopy
EOT	equivalent oxide thickness
FGA	forming gas anneal
G-V	conductance voltage
h	Planck's constant

I	electric current
IPA	isopropylalcohol
KE	kinetic energy
MOSCAP	metal oxide semiconductor capacitor
MOSFET	metal oxide semiconductor field effect transistor
N_{bt}	border trap density
nm	nanometer
PAW	projector augmented wave
PBE	Perdew-Burke-Emzerhof
PDA	post deposition anneal
PP	pseudo potential
PES	Photo emission spectroscopy
SRC	Semiconductor Research Corporation
STEM	Scanning transmission microscopy
TDMAH	tetrakis(dimethylamino)hafnium
TMA	trimethylaluminum
V	volts
VASP	Vienna ab-initio simulation package
VB	valence band
V_{fb}	flatband voltage
V_{th}	threshold voltage
Φ_{spec}	spectrometer work function

LIST OF FIGURES

ACKNOWLEDGEMENTS

This dissertation would not be possible without the contributions and support from colleagues, friends and the family members in the past five years.

First and the foremost, I would like to thank my advisor Prof. Andrew Kummel for his guidance and great support for the projects I proposed and worked on. Endless discussions we had about the projects anytime by using all means of advanced communication technology were great inspiration. It is a pleasure to work him most of the time especially after the morning coffee hour. His endless demands had me learn and gain invaluable knowledge and hands on skills in addition to establish collaborations by travelling to other research institutions all over the continent. Not only in science I advanced with his supervision, as a non-native speaker I also developed critical skills of presentation and communication thorough attending numerous conferences every year. One most important thing that I learned from Prof. Kummel is his vision on conducting research with great collaborations he establishes. It is certainly a great experience I had which shaped my research career.

I gratefully acknowledge our colleges and collaborators for their contributions;

Prof. Yuan Taur, for critical and fruitful discussions on interface state model

Prof. Paul McIntyre, for critical reviews and insights on collaborated research articles

Prof. Peter Asbeck, for invaluable discussion and assistance on ferroelectric characterization

Prof. Prabhakar Bandaru, for the insightful discussion in class and being in my committee

Prof. Brian Maple, for kindly being part of the committee

Prof. Moon Kim, for STEM-EELS experiments and discussions

Prof. Alan Seabaugh, for allowing me to use their clean room at University of Notre Dame

Prof. Suman Datta, for allowing me to use their lab for at University of Notre Dame

Dr. Vincent Hou, for great help and insight into EELS analysis

Dr. Toshihiro Aoki, for helping STEM-EELS experiments at UC Irvine

Dr. Peter Ercius, for help with STEM-EELS experiment at Molecular Foundry at LBL

Dr. Eli Rotenberg, for the ER-PES experiments at ALS and data analysis

Dr. Aaron Bostwick for ER-PES experiments at ALS and data analysis

Dr. Kechao Tang for providing software for interface defect density analysis

Dr. Evgueni Chagarov, for collaboration on DFT modelling of SiGe/HfO$_2$ interface

Dr. Qingxiao Wang for providing STEM-EELS characterization of control devices

  In past two years, I had a great pleasure to work with small group of people closely, Emily Thomson, Victor Wang, Harshil Kashyap and Jake Millhiser on various projects. The last project was specifically challenging due to complexity and the scale of the project within limited time and budget requiring focused team effort. In less than six months, the team built up multi-purpose integrated hot wall ALD reactor cluster system which mimics multimillion industrial tool. It consists of chemical process dedicated five reactor chambers (Oxide, Plasma, Nitride, Low work function, Metal ALD and analyzer chambers) separated from each other to limits cross contamination. This advanced tool was named CoExist with the analogy of the all chambers coexisting and working together. It was significant experience on working such complex and demanding project with such a great team. In conjunction with this, I would like to mention contributions from Team Cat members (CAD); Manon

Chapter II is part or in full a reprint from materials published in *Appl. Mater. Inter*, 2018 with title "Ultra-Low Defect Density at sub 0.5 nm HfO$_2$/SiGe Interfaces via Selective Oxygen Scavenging", <u>M. S. Kavrik</u>, E. Thomson, E. Chagarov, K. Tang, S. Ueda, V. Hou, T. Aoki, M. Kim, B. Fruhberger, Y. Taur, P. McIntyre, A. Kummel. The dissertation author was the primary investigator and author of this paper.

Chapter III is part or in full a reprint from materials published in *Appl. Mater. Inter*, 2018 with title "Ultra-Low Defect Density at sub 0.5 nm HfO$_2$/SiGe Interfaces via Selective Oxygen Scavenging", <u>M. S. Kavrik</u>, E. Thomson, E. Chagarov, K. Tang, S. Ueda, V. Hou, T. Aoki, M. Kim, B. Fruhberger, Y. Taur, P. McIntyre, A. Kummel. The dissertation author was the primary investigator and author of this paper.

Chapter IV is part or in full is a reprint from materials submitted (in review) to *Appl. Mater. Inter* with the title "Engineering high-k/SiGe interface with ALD oxide for selective GeO$_x$ reduction" <u>Mahmut S. Kavrik</u>, C. Y. Lee, P. Ercius, Y.C. Liang, J. Cheung, K. Tang, V. Hou, Q. Wang, B. Fruhberger, M. Kim, Y. Taur, P. C. McIntyre and A. C. Kummel. The dissertation author was the primary investigator and author of this paper.

Chapter V is part or in full is a reprint from manuscript currently being prepared for publication with title "Suppression of electronic defects at the SiGe/high-k oxide interface via selective surface oxidation", <u>Mahmut S. Kavrik</u>, A. Bostwick, E. Rotenberg, K. Tang, E. Thomson, V. Hou, T. Aoki, B. Fruhberger, Y. Taur, P.C. McIntyre and A. Kummel. The dissertation author was the primary investigator and author of this paper.

VITA

EDUCATION

2006   Bachelor of Science Education, Selcuk University

2012   Master of Science in Physics, Gebze Institute of Technology

2019   Doctor of Philosophy in Materials Science and Engineering, University of

California San Diego

IEEE – SISC Ed Nicollian award for best student paper (2017)

Fulbright U.S. Fellowship (2013-2015)

PUBLICATIONS

Ultra-Low Defect Density at sub 0.5 nm HfO_2/SiGe Interfaces via Selective Oxygen Scavenging, *Appl. Mater. Inter, 2018.* M. S. Kavrik, E. Thomson, E. Chagarov, K. Tang, S. Ueda, V. Hou, T. Aoki, M. Kim, B. Fruhberger, Y. Taur, P. McIntyre, A. Kummel

Engineering high-k/SiGe interface with ALD oxide for selective GeO_x reduction. (submitted ACS, AMI) Mahmut S. Kavrik, C. Y. Lee, P. Ercius, Y.C. Liang, J. Cheung, K. Tang, V. Hou, Q. Wang, B. Fruhberger, M. Kim, Y. Taur, P. C. McIntyre and A. C. Kummel

Suppression of electronic defects at the SiGe/high-k oxide interface via selective surface oxidation" (in preparation), Mahmut S. Kavrik, A. Bostwick, E. Rotenberg, K. Tang, E. Thomson, V. Hou, T. Aoki, B. Fruhberger, Y. Taur, P.C. McIntyre and A. Kummel

Density-Functional Theory Molecular Dynamics Simulations of a-HfO2/a-SiO2/SiGe and a-HfO2/a SiO2/Ge with a-SiO2 and a-SiO suboxide interfacial layers, Appl. Surf Sci. Vol 443, 2018. E. Chagarov, M. S. Kavrik, Z. Fang, W. Tsai, A. C. Kummel

Low interface trap density in scaled bilayer gate oxides on 2D materials via nanofog low temperature atomic layer deposition, Applied Surface Science Volume 463, 2018. I. Kwak, M. S. Kavrik, Jun Hong Park, L. Grissom, B. Fruhberger and A. C. Kummel

Low temperature thermal ALD TaN$_x$ and TiN$_x$ films from anhydrous N$_2$H$_4$, Appl. Surf. Sci, Volume 462, 2018. Steven Wolf, Michael Breeden, Iljo Kwak, Jun H Park, Mahmut Kavrik, Mehul Naik, Daniel Alvarez, Jeffrey Spiegelman, Andrew C Kummel

Cycling excitation process for light detection and signal amplification in semiconductors, Optical Sensing, imaging: Nanostructured Devices and Applications 2016. Y. Liu, A. Zhang, M. Miah, D. Hall, I. Niaz, L. Yan, Y. Yu, M. S. Kavrik, Y. Lo

Ferromagnetic Resonance in Y$_3$Fe$_5$O$_{12}$ Nanofibers, Appl. Phys. Lett. **99**, 102501 (2011). A. Jalalian, M.S. Kavrik, S.I. Khartsev and A.M. Grishin

Nanolaminate structure, semiconductor device and method of forming nanolaminate structure, **US Patent** App. 15/682,873, 2018, FANG Zi-Wei, LUAN Hong-Fa, W. Tsai, K. Sardashti, M. Clemons, S. Ueda, M. S. Kavrik, I. Kwak, A. Kummel, Hsiang-Pi Chang

Master Thesis, in Physics: Analysis of Magnetic Thin Films with Broadband Ferromagnetic Resonance, Gebze Institute of Technology, TURKEY, 2012

ABSTRACT OF THE DISSERTATION

Suppression of Electronic Defects at the Oxide-SiGe Interface

Using Intuitive and Counter-Intuitive Techniques

by

Mahmut Sami Kavrik

Doctor of Philosophy in Materials Science and Engineering

University of California San Diego, 2019

Professor Andrew C. Kummel, Chair

Novel materials are great demand for boosting transistor performance in scaled integrated electronic circuits especially as the channels approach atomic dimension stretching traditional scaling limits. The high effective carrier mobility of SiGe in p-channel field effect transistors (pFETs) promises enhanced transport for high speed electronics. SiGe is a very convenient alternative channel material because unlike III-V semiconductors, SiGe can be readily grown epitaxially on Si substrates. However, formation of localized surface states in the bandgap hence the trapped charges at the interface during gate oxide deposition on SiGe hinders SiGe integration into pFETs.

Surface passivation prior to gate oxide growth is incapable of preventing GeO_x formation during atomic layer deposition (ALD) due to diffusion of oxidant species which react with the SiGe surface thereby deteriorating the interface. Therefore, control over the structure and composition of high-k gate oxide/SiGe interface with layer by layer ALD oxide growth is not attainable.

ALD reactant species can be utilized to passivate the interface defects during or after oxide deposition by benefiting from facile diffusion through gate oxide. In this dissertation, investigation and suppression of electronic defects at SiGe/high-k oxide interface during and after gate oxide deposition is investigated. Correlations are made between the interface charge trap density (D_{it}) determined by impedance measurements and the chemical - physical structure of the interfaces obtained with advanced nanoscale characterization techniques. In all these studies, unlike ideal layer-by-layer oxide ALD, unconventional oxidation on SiGe is observed during ALD. This non-ideality which is the source of defect formation at the high-k/SiGe interface, is exploited to suppress electronic defects.

Ultra-low defect (9.4×10^{10} cm^{-2}) HfO_2/SiGe interfaces (<0.5nm thick) are formed using selective oxygen scavenging from the SiGe interface using oxygen reactive metal gates or highly reactive ALD precursors. These processes form SiO_x rich and GeO_x deficient interfaces by utilizing the difference in oxidation enthalpy of Si versus Ge. A nearly inverse process is found using a strong oxidant ozone which can readily diffuse to the interfaces, promote GeO_x out diffusion and sublimation leaving SiO_x rich low defect interface.

Chapter I

Investigation of Oxide/SiGe Interface with Advanced Characterization Techniques
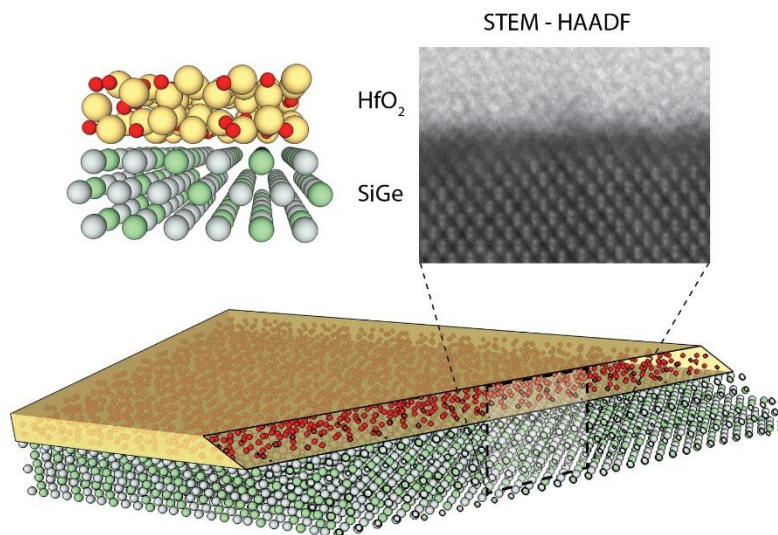
1.1 Introduction

Demand for low-power electronic devices and boost in transistor performance drives research on high-mobility channel materials with high-k dielectric gate oxides for better electrostatic control of channels in transistors beyond the 14 nm node[2]. Compound semiconductors such as SiGe alloys are being investigated for p-type channel material for Si replacement because of their higher mobility[3,4] and tunability of the band gap. In current complementary metal–oxide–semiconductor (CMOS) transistors, SiGe[2,5] is employed in stressor layers, however, the integration of SiGe as a top surface channel is hindered by poor interface formation between the gate oxide and SiGe primarily due to GeO_x formation[6,7].

1

Theoretical calculations with density functional theory (DFT).[8] showed that a defect-free band gap prior to forming gas anneal (passivation of Ge and Si dangling bonds by atomic hydrogen) can be established with a monolayer Si-O interfaces between SiGe and HfO_2 high-k gate oxides. The main challenge is the binary atom termination (Si-Ge) of the surface in which preferential Si oxidation and Si-O formation is a difficult process during atomic layer deposition (ALD) oxidation due to excess oxygen-containing molecules in ALD reactors at elevated temperatures which results formation of mixed SiO_x - GeO_x interlayer and dangling bonds on both Si and Ge[6,7,9]. Elimination of thermally non-stable GeO_x species may be possible with Si cap layers epitaxially grown on SiGe channels for planar devices; however, it is problematic for gate-all-around devices or FinFETs[10].

Passivation of the SiGe surface and minimization of associated interface defects between SiGe high-k dielectrics prior to gate oxide deposition has been studied intensively including plasma nitridation[11,12] and sulfur[13] treatment however, the interfaces deteriorates by diffusion of species at elevated temperature during ALD process. A primary source of interface defects are the sub-oxides of Ge which readily form during SiGe oxidation;[14] volatile GeO diffuses through the gate oxide degrading device performance[7,15]. Furthermore, unlike SiO, GeO can desorb from the oxide surface at low temperature ($\sim$ 400C) and induces significant Ge consumption from the interface by sublimation[16-20]. Apart from this, GeO_2 is water soluble[21] which is not desired in manufacturing processes. Conversely, interface defects can be suppressed by modification of SiGe oxide interfaces during or after ALD process by utilizing diffusion of reactive oxygen species or by reducing GeO_x with gettering process.

In this work, suppression of electronic defects at the high-k gate oxide/SiGe interface during and after gate oxide deposition is investigated with metal oxide semiconductor capacitors (MOSCAPs) devices. Correlations are made between the interface charge trap density (D_{it}) determined by impedance measurements and the chemical - physical structure of the interface obtained with high resolution scanning transmission electron microscopy (STEM) and electron energy loss spectroscopy (EELS) along with energy dispersive x-ray spectroscopy (EDS). Diffusion species from SiGe interfaces into gate oxides seen in STEM-EELS are verified with compositional depth profiling obtained with energy resolved photoemission spectroscopy (ER-PES) performed with non-destructive soft x-ray probe at synchrotron.

The dissertation is organized into five chapters. Basics of the device fabrication methods and advanced characterization techniques are introduced in first chapter. Chapter II presents post ALD defect reduction mechanism at HfO_2/SiGe interface with selective oxygen using direct gettering metal gates such as Al. Chapter III presents remote oxygen scavenging by using diffusion barriers. Novel hetero gate oxide structures formed with $Al_2O_3 - HfO_2$ introduced in chapter IV to explore selective oxygen scavenging by using highly oxygen reactive trimethyl aluminum (TMA) precursor. In chapter V, a counter intuitive interface defect reduction mechanism during ALD oxide growth is presented in which by controlling diffusion of oxygen species (GeO_x) with ozone exposure, selective surface oxidation was achieved. In last chapter, preliminary results from ferroelectric oxide – SiGe interface and future perspectives is discussed.

1.2 Oxide Semiconductor Interfaces and Defects

Delocalization of the wave function in periodic potential is one of the manifestations of quantum physics which results exotic transport properties in solids. The advancement in CMOS came along with solutions to passivation problems of Si-oxide interface charge traps induced by the localized surface states formed due to sudden termination of periodic Si atoms at the surface.[22] In atomic picture, semiconductor surface atoms are prone to charging due to uncompensated covalent electrons such as dangling bonds in Si. Metal surfaces can compensate the imbalanced surfaces by flooding the with electrons; however, in semiconductors, deficiency of the charges (depending on dopant level) can induce space charge region spreading potential to a distance from the surface.[23,24] Therefore, semiconductor surface potential can be modified significantly by the surface trap charges. In contact with oxide, semiconductor surface potential can be even more complicated because of space charges take place in oxide itself as a result of device fabrications or oxide nature. Hence, neither oxide nor semiconductor oxide interface is neutral and modifies the surface potential accordingly.

The oxide and its interfaces with semiconductor can have distinct charges classified in four categories as shown in figure 1.1. These trap charges can impact device operation significantly by changing the potentials in channels of MOSFET. Elimination of the charge traps for Si and its native oxide SiO_2 is well studied. However, novel channel materials necessitate additional research due to absence of thermally stable, defect-free native oxides.

Fixed oxide charge: It is positive charge located in oxide near the interface as illustrated in white region in figure 1.1. It is induced by the fabrication process, and it can affect the surface potential and channel mobility.

Mobile ionic charges: These are process induced ionic impurities such K^+ or N^+ which can move under bias thereby effect the surface potential.

Oxide trapped charge: These charges are trapped in oxide as a result of electron-hole pairs generation due to high energy particle bombardment during fabrication.

Interface trapped charge (D_{it}): These charges located between semiconductor and the gate oxide, and, unlike other type of charge traps, they are electrically active. They can be both positively and negatively charged depending on structure and the composition of the oxide semiconductor interface. Trapped charges in surface states can contribute to current conduction by transitioning from surface state to conduction band or valence band.
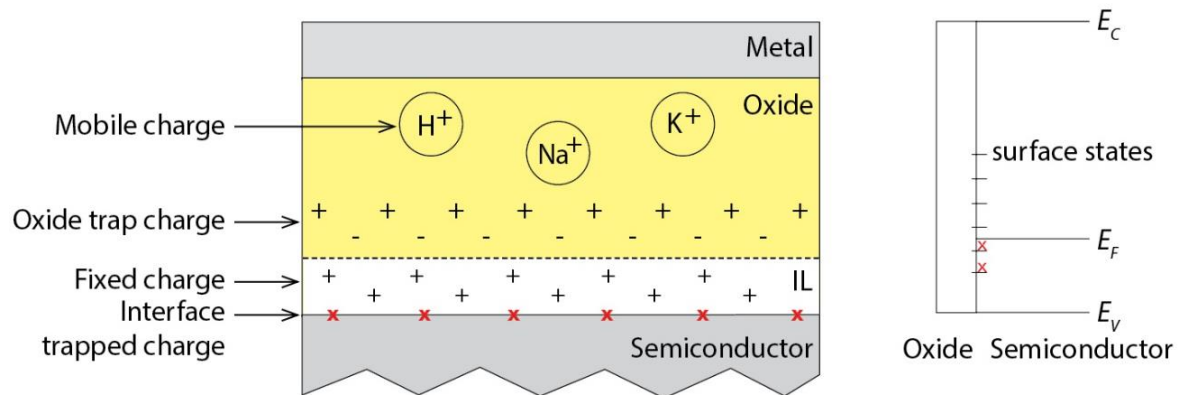
Figure 1.1 Oxide defects and surface states. Four type of defects and their locations are illustrated in the oxide. Interface defects are denoted with red cross. Correspondingly, band diagram of p-type MOS in flat band voltage is shown on the right. Red cross indicates trapped charges in surface states in band gap below the fermi level.

5

Interface trapped charges are induced by surface states located in band gap with fixed position relative to energy-band edges. Therefore, they can be occupied or emptied depending on the Fermi level position. By changing surface potential of the semiconductor (V_g in MOS), the occupation probability of the surface states changes as the energy of the surface states bends along with band respect to fermi level. Consequently, the trapped charge at the surface states induce capacitance (C_{it}) in parallel with semiconductor capacitance (C_{SC}). The total MOS capacitance (C_g) is govern by;

$$\frac{1}{C_g} = \frac{1}{C_{ox}} + \frac{1}{C_{SC} + C_{it}} \quad Eq\ 1.21$$

where C_{ox} is the oxide capacitance.

Interface charge trap can change the semiconductor surface potential, increase the leakage current with band to band tunneling by acting as generation – recombination centers. The interface charge traps (electronic defects) induced by surface states can deteriorate the semiconductor device operation. For instance, for VLSI circuits, ease of transistor switching is desirable which is known as steep subthreshold switching. High interface trap density can adversely affect subthreshold slope (S) because the interface charge trap associated capacitance is in parallel with depletion capacitance (C_d) as shown in equation 1.22.[25].

$$S = \left(\frac{dlog_{10}I_{ds}}{dV_{gs}}\right)^{-1} = 2.3\frac{kT}{q}\left(1 + \frac{C_d}{C_{ox}}\right) Eq\ 1.22$$

Oxide formation on semiconductor surface can passivate or induce more charge interface trap charges depending on the materials and the fabrication process[25]. In addition, the oxide itself or the oxide deposition process, can induce fixed or mobile oxide charge which can modify the surface potential.

1.3 Electrical Characterization of Metal Oxide Semiconductor (MOS) Capacitor

MOS capacitors are core of metal oxide semiconductor field effect transistors (MOSFET); hence, they have been studied extensively and has an established model of operation[26]. Electrical characterization of MOSCAP devices is relatively easy and provides several device parameters by inspection. Quantitative information about the semiconductor – oxide interface can be obtained from MOSCAPs with careful analysis of multifrequency capacitance and conductance measurements. Due to the simple device structure of MOSCAPs as shown in figure 1.2 and relatively easy fabrication procedure, it is common practice to study the quality of the gate oxide with MOSCAPs prior to complex MOSFET fabrication.

MOSCAPs operation is well documented in textbooks. In this dissertation two main characteristics of C-V and G-V are analyzed; frequency dependent depletion capacitance induced by interface charge traps and the maximum capacitance (C_{max}) which is typically a function of oxide thickness and dielectric constant (relative permeability). Apart from this, the leakage across the gate oxide obtained with I-V measurements are reported.
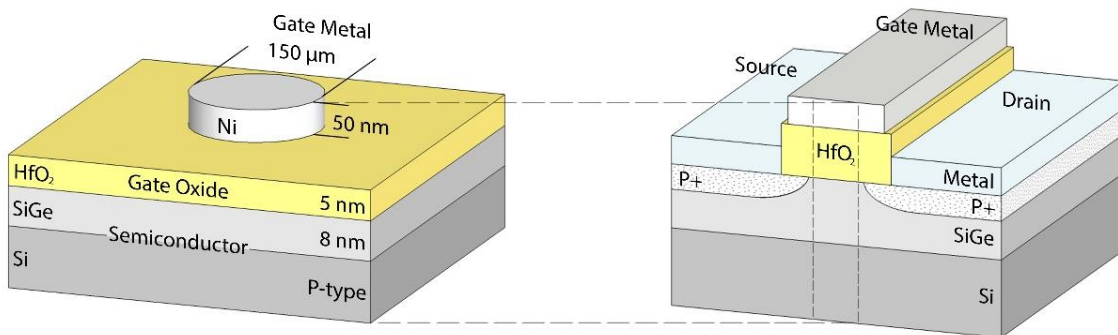
Figure 1.2 MOS and MOSFET device structures. MOS devices forms the base for the MOSFET transistors. Oxide and oxide – semiconductor interface quality can be studied with MOS. The general structure of the MOS device used in dissertation is illustrated.

7

Multifrequency capacitance (C-V) and conductance (G-V) measurements are performed typically ranging from 1 kHz to 1 MHz using LCR meter by measuring the ac current in the circuit while running AC (~30mV) voltage superimposed on DC bias voltage applied between the gate electrode and the substrate as shown in figure 1.3 Total capacitance (C_{MOS}) is the sum of the oxide and semiconductor capacitances in series.

For a p-type MOSCAPs, C-V and G-V are measured from inversion to accumulation by biasing the gate from positive to negative. The maximum capacitance (C_{max}) is achieved in accumulation as the negative gate bias accumulates the majority charge carriers, holes at the surface. The frequency dispersion in accumulation can be induced by border traps result of quantum tunneling of oxide charges located close to surface.[27] In C-V depletion, the holes are repelled by the positive gate bias hence the capacitance diminishes. However, charge traps at the interface due to surface states forms frequency dependent depletion capacitance.

The density of the interface charge traps (D_{it}) can be extracted by measuring multifrequency C-V and G-V in this region. Above threshold gate voltage (V_{th}), MOSCAPs go into inversion in which the minority carriers, electrons, accumulate at the channel surface at low frequencies. (<100 Hz).[28,29]

$$v_o \cong (RG + j\omega RC)v_i$$

$$C_{MOS} = \frac{d(-Q_S)}{dV_g}$$

$$\frac{1}{C_{MOS}} = \frac{1}{C_{ox}} + \frac{1}{C_{SC}}$$
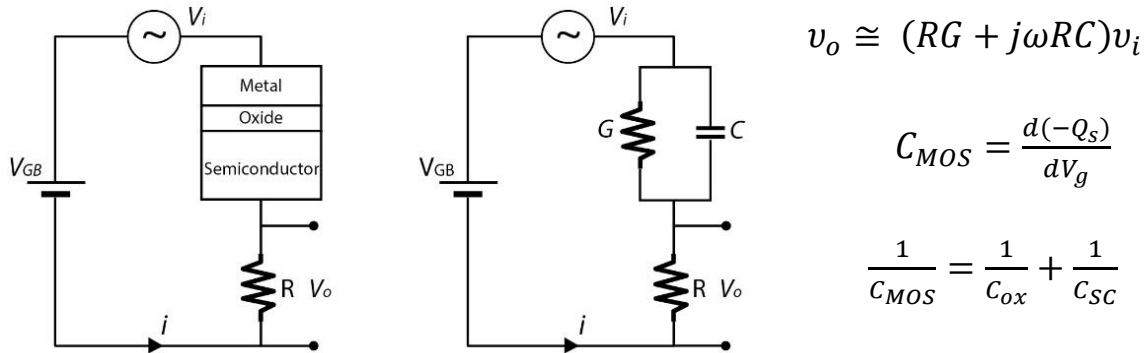
Figure 1.3 C-V and G-V measurement setup of MOS device. High frequency (>100 Hz) experiments can be performed by measuring current through resistor to obtain v_o.

1.4 Quantification of Interface Trap Charge Density (D_{it})

Interface trapped charges induce frequency dependent capacitance due to trapping and de-trapping of charges at the interface in response to change in surface potential by gate bias. This process is time dependent which determines the max measurement frequency of the interface states since charge trapping rate cannot follow up the change in bias at very high frequencies typically 1MHz. The interface defect capacitance can be determined by comparing the capacitance below and above the frequency of the trapping rate. This method is known as Terman method (C-V stretch out) which assumes that high frequency measurements has no interface defect component. However, several significant factors such as border traps, slow traps, depletion capacitance and conductance which is complex function of minority carriers are ignored[30].

Interface trapped charge capacitance (C_{it}) is in parallel to the semiconductor capacitance (C_{SC}) as shown in figure 1.4 b. Charging and discharging the interface traps is a lossy process therefore the resistance R_{it} is included in circuit as shown in figure 1.4 c.
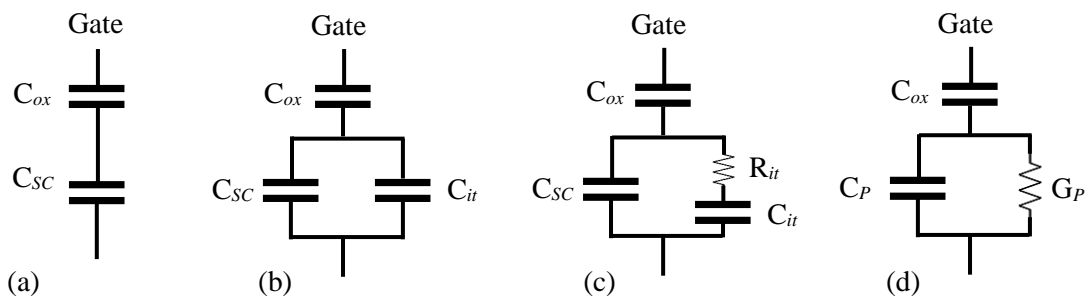
Figure 1.4 Equivalent circuits of an MOS capacitor and interface traps. Equivalent MOS circuit without (a) and with (b) interface charge traps. (c) MOS circuit with interface trap time constant $\tau_{it} = R_{it} C_{it}$. (d) Simplified circuit with C_{it}, R_{it} and C_{SC} lumped into C_P and G_P.

The circuit in c can be simplified as circuit in d by introducing parallel capacitance C_P and parallel conductance G_P given by;

$$C_P = C_{SC} + \frac{C_{it}}{1 + (\omega\tau_{it})^2} \quad Eq\ 1.41 \quad and \quad \frac{G_P}{\omega} = \frac{\omega\tau_{it}qD_{it}}{1 + (\omega\tau_{it})^2} \quad Eq\ 1.42$$

where, $C_{it} = q^2D_{it}$, $\omega = 2\pi F$ and (interface trap time constant) $\tau_{it} = R_{it}\,C_{it}$.

Interface defect density D_{it} can be calculated from equation 1.42 by measuring conductance which corresponds to single energy level in the band gap. By measuring G_P as a function of gate bias for range of frequencies (typically 10kH to 1MHz), the D_{it} distribution across the band gap (from weak inversion to flat band) can be obtained. This methods provides D_{it} as low as 10^9 cm^{-2}eV^{-1} proposed by Nicollian and Goetxberger[26].

The defect trapping and de-trapping occurs near the fermi level, and this introduces time dispersion. The normalized conductance is given by

$$\frac{G_P}{\omega} = \frac{qD_{it}}{2\omega\tau_{it}} \; \ln[1 + (\omega\tau_{it})^2] \quad Eq\ 1.43$$

A graph of G_P/ω versus ω exhibits a peak at $\omega\tau_{it} = 1.98$ from which $D_{it} = 2.5\,G_P/q\omega$ can be calculated. The Gp value is obtained from the measured MOS total admittance $G_{tot} + j\omega C_{tot}$ using $[G_p + j\omega C_p]^{-1} = [G_{tot} + j\omega C_{tot}]^{-1} - (j\omega C_{ox})^{-1}$. Accuracy of the D_{it} calculation is a function of the series resistance in measurements and the determination of precise C_{ox} value which can deviate if $qD_{it} > C_{ox}$. Apart from these, the tunneling leakage current, border traps, series resistance of the device itself and the resolution of the measurement setup can affect the accuracy[26,31]. Therefore, C_P analysis is critical to rule out underestimated effects in D_{it} calculation.

Full interface-state model eliminates these concerns by using a single energy Y circuit in which for a given surface potential, the capacitance induced only from the trap density at the Fermi level. At every gate bias or surface potential (ψ_s), the three components are completely specified by parameters G_{gr}, τ_n, and τ_p, (figure 1.5) which are chosen to fit both the $C_{tot}(\omega)$ and the $G_{tot}(\omega)$ data at that point. The interface-state model is obtained by converting Y circuit to a Δ circuit in which each element is complex frequency dependent admittance is integrated with respect to the defect energy. Details of the full interface-state model can be found elsewhere[26].

In this dissertation, conduction and full interface state models used to extract interface charge trap density from *C-V* and *G-V* measurements.
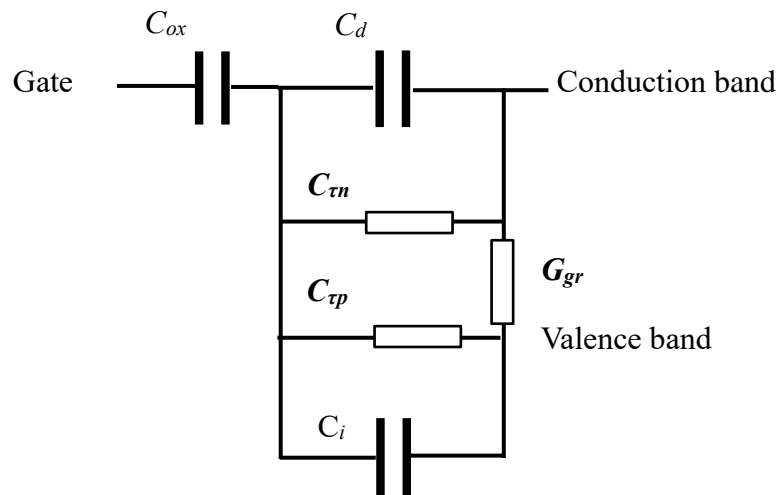
Figure 1.5 Equivalent circuit model of an MOSCAP with interface state elements.

1.5 Density Functional Theory

Electronic structures of the three-dimensional materials system can be modelled using computational quantum mechanical models. Density functional theory (DFT) is one of the commonly used technique to study the electronic structures of the many body systems in ground state[32]. By using functionals of electron density, the interatomic interactions and complex behavior of the many body condensed matter system can be determined in ground state.

In this dissertation, all DFT simulation were performed by Dr. Evgueni Chagarov. The DFT simulations of the high-k/SiGe interface were performed with Vienna *ab initio* simulation package (VASP) using projector augmented-wave (PAW) pseudopotentials (PPs) and the Perdew–Burke–Ernzerhof (PBE) exchange-correlation functional[33] Stoichiometric a-HfO$_2$ samples including 40 Hf and 80 O atoms were used for simulations. Hybrid classical and DFT-MD simulations including annealing, cooling and relaxation is used to generate several a-HfO$_2$ system. The quality of the amorphous nature were verified via radial-distribution function (RDF) main peak positions, average nearest neighbor numbers, nearest neighbor distributions, and DFT calculated[34] band gaps demonstrating good correlation to available simulated and experimental reference properties.[35] The sample matching to experimental result was selected and used for simulations. The amorphous samples were generated to match the SiGe (001) surface area. A more detailed explanation of a-HfO$_2$ sample generation was presented elsewhere.[34]

1.6 Atomic Layer Deposition (ALD)

ALD is a layer by layer material deposition technique on substrate by dosing chemical precursors consecutively along with their purge from reactor with noble gas or nitrogen in between. Large-scale film deposition in atomic scale thickness can be obtained regular base due to self-limiting chemical reactions nature of the process. ALD is employed in semiconductor manufacturing to produce stoichiometric oxides with precise thickness control in high aspect ratio features. In addition, multilayer oxide ALD can be obtained by changing the precursor chemistry during the process. ALD is widely used to deposit metals and oxides and recently plasma assisted ALD, electron enhanced ALD being developed to activate the ALD reactions[36]. Atomic layer etching (ALE) processes is also in development for similar reasons.

The Al_2O_3 ALD deposition process is illustrated in figure 1.6. The O-H terminated substrate is exposed to trimethylaluminum (TMA, Al $(CH_3)_3$), and precursor molecules adsorb on the surface until saturation. Aluminum and oxygen form a bond, and H bonds the CH_3 ligands to form CH_4 (g). Excess of precursor is purged from the reactor by nitrogen gas prior to the second precursor dosing. Water is the typical oxidizer and is introduced into reactor to form Al_2O_3 after reacting with dimethyl aluminum adsorbates on the surface releasing CH_4 gas. Excess H_2O and methane are removed by second purge process terminating the surface with hydroxyl groups (-OH) which provide nucleation sites for TMA dose in second ALD cycle. This one cycles forms single Al_2O_3 layer of about 1 angstrom on the surface and the whole process cycle can be repeated for desired thickness.

$$1\text{-} \quad \textbf{AlOH + Al (CH3)}_3 > \textbf{AlOAl(CH3)}_2 + \textbf{CH}_4$$

$$2\text{-} \quad \textbf{AlCH}_3 + \textbf{H}_2\textbf{O} > \textbf{AlOH + CH}_4$$
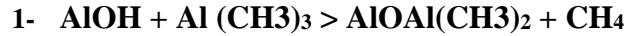
Stoichiometry, growth rate and uniformity of the oxide grown with ALD process is subject to process conditions such as temperature, pressure, initial surface condition, precursor chemistry, precursor dose time, purge time between precursor doses which necessitates careful process optimizations.
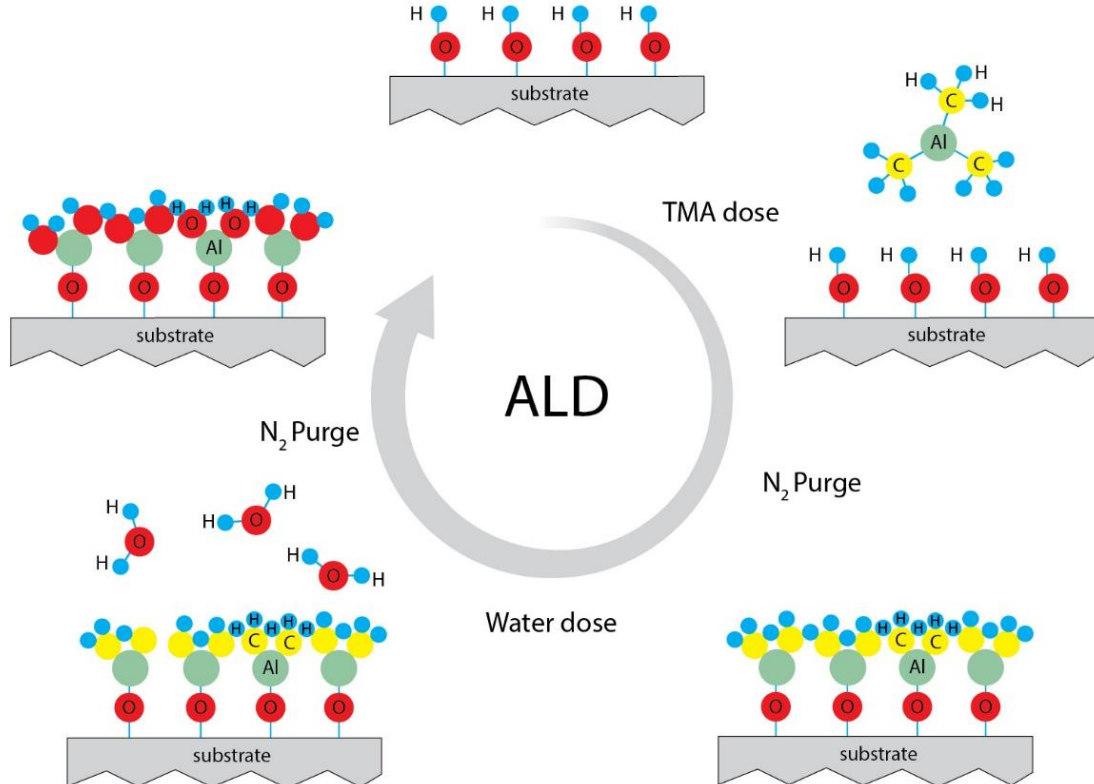
Figure 1.6 Illustration of Al₂O₃ atomic layer deposition process. Deposition occurs with TMA and H_2O precursors along with nitrogen purge. TMA reaction with the hydroxyl forms methane as reaction byproduct purged out with N_2. The methyl groups react with H_2O and form Al-O bonds. Methane purged out and leaves hydroxyl terminated surface for the next ALD cycle

1.7 Electron transparent TEM Specimen Preparation with Focus Ion Beam

Fast and precise milling with high energy ions (Ga) and Pt deposition in nanoscale makes focused ion beam (FIB) irreplaceable for TEM sample preparation. The details of the technique with process step can be found in literature[37]. While high energy ions readily remove material, the high energy ions can induce significant damage on lamella surface by extending into the material several nanometers.[38] Therefore it is common practice to reduce the beam energy at last step to remove damaged layer; however, this may not be adequate to obtain high resolution STEM image. Low energy Ar ions (<1keV) is used mostly to improve image quality by removing dead layer from lamella surface.
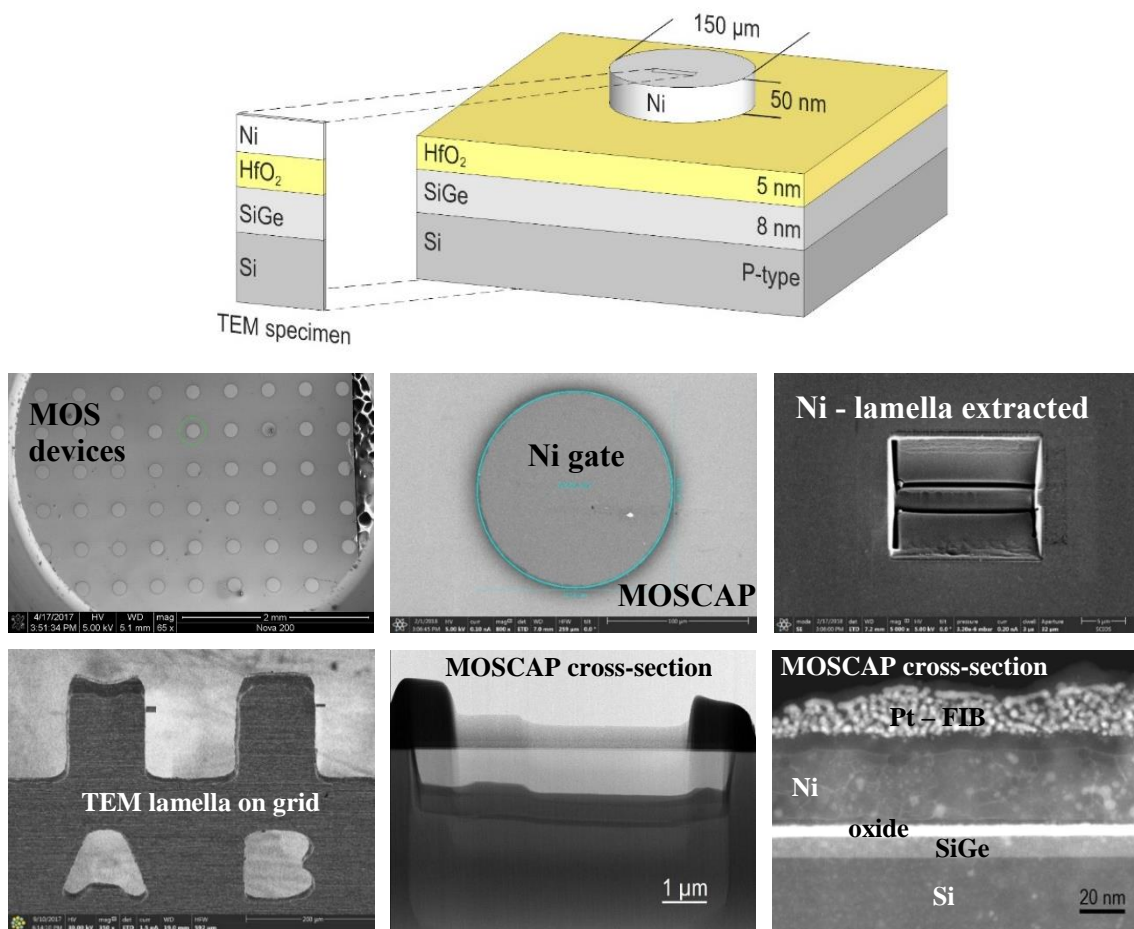
Figure 1.7 TEM specimen preparation from MOSCAP device.

15

1.8 Scanning Transmission Electron Microscope (STEM)

STEM is powerful technique to study materials and interfaces due to its unique sub angstrom spatial resolution. Transmission electron microscope is very old technique; however the development in monochromatic high energy electron emission gun, high quality electron lenses and detectors has significantly improved resolution[39].

In TEM, images formed by parallel high energy electrons (typically 200-300keV) passing through the thin specimen are captured by large area detectors. In scanning TEM, (STEM) a focused electron probe of sub angstrom diameter rasters across the sample, and STEM images are formed by detecting the transmitted electrons. By correcting for spatial and chromatic aberrations in electron beam, it is possible to obtain sub angstrom resolution STEM images. Compositional profiles of the specimen in atomic resolution can be obtained with spectrometer integrated into STEM microscope.

High angle annular dark field (HAADF) detector is commonly used for the STEM image acquisition due to convenient interpretation of the image correlated directly with atomic number of the elements (z-contrast). HAADF images (see figure 1.8) formed with forward scattered electrons impinging on detectors outside the electron beam column. Bright field (BF) images are complementary to HAADF. BF images are obtained with electrons incident on a detector located on the transmitted electron path. A typical STEM microscope with aberration corrector equipped with HAADF, BF, EELS, EDS detector is shown in figure 1.8.
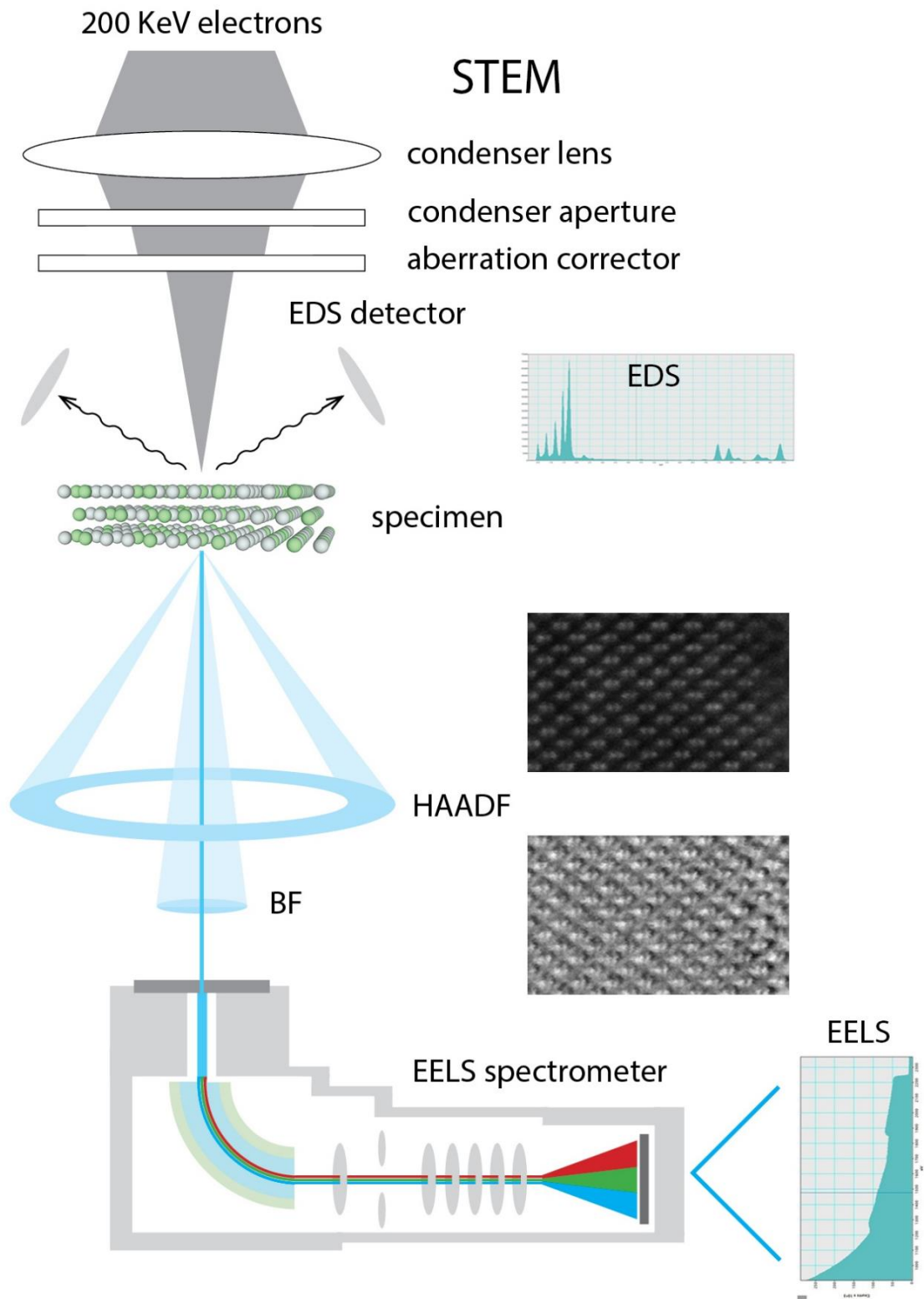
Figure 1.8 Scanning Transmission Microscope schematics. The STEM microscope with HAADF, BF imaging detectors and EDS, EELS spectrometers are illustrated.

1.9 Electron Energy Loss Spectroscopy (EELS)

EELS became a widely used spectroscopic technique upon critical advancements [40] in electron microscopy especially with spatial aberration correction[41,42] and implementation of energy monochromators[39]. High energy monochromatic electrons loose energy and changes their trajectories as a result of elastic and inelastic scattering with atoms in specimen due to Coulomb interaction[43]. An EELS spectrum is taken by detecting transmitted electrons passed through energy analyzer. By monitoring the energy difference of inelastically scattered vs non-scattered electrons respect, chemical information about the specimen can be extracted. The energy loss of the transmitted electrons is correlated with the excitation energy of core electrons from their ground state into empty states above the Fermi level. In addition, chemical bonding and the occupancy of the states can be determined by monitoring the near edge structure of the energy loss of core electrons (ELNES)[44].

EELS compositional mapping can be obtained by scanning the electron beam across the specimen. During EELS experiments, large angle elastically scattered electrons can be collected with high angle annular dark field detectors. As illustrated in figure 1.8, a z-contrast STEM image (HAADF) of the probed location can be obtained along with compositions from EELS[45]. In this way, by using microscope equipped with aberration corrector (Cs corrected) for sub-Angstrom spatial resolution and electron energy monochromators with energy resolution below 100 meV[39], the structure and chemical composition (along with bonding states) of the specimen can be obtained[46] with atomic scale resolution[47].

Typical EELS spectrum shown in figure 1.9 can be divided into three regions; the zero loss (ZLP) containing elastically scattered electrons, the low loss region, and the high loss region. The energy resolution of the system can be obtained from the full-width of half-maximum of the zero-loss peak (ZLP) which provides additional information about thickness of the specimen upon transmission. The EELS low loss region (spectra energy losses up to 50 eV) dominated by plasmon excitations and inter-band transitions which provides information about optical properties. The higher energy loss (core-loss) region provides information about core-level excitations; the losses provide information on the elemental composition of the specimen as well as local unoccupied density of states.
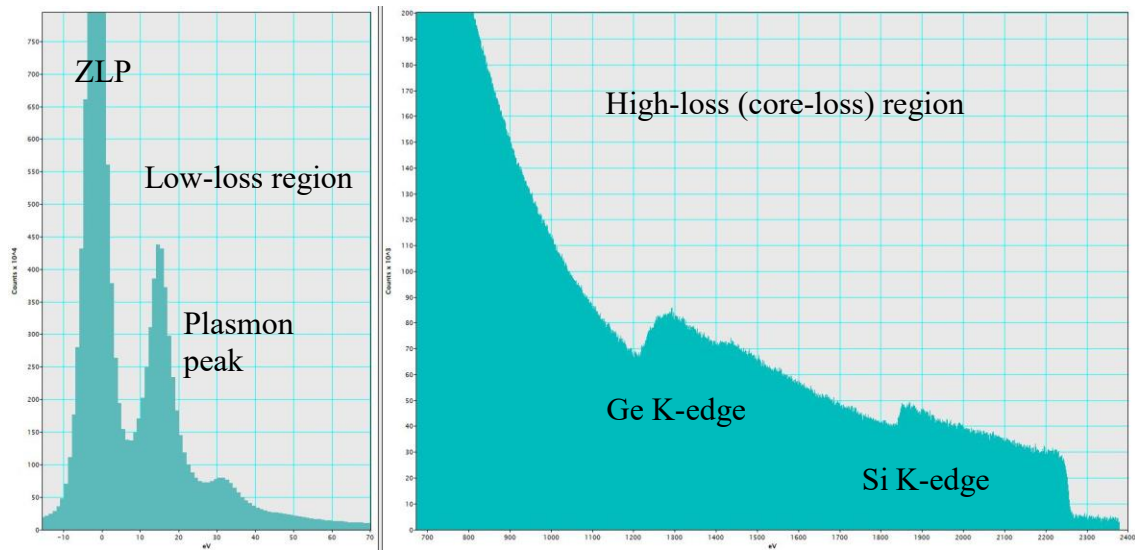
Figure 1.9 EELS spectrum. The zero loss, low loss and core loss regions of the spectrum is shown. Spectrum is taken from epitaxial SiGe (30%).

1.10 Energy Dispersive X-ray Spectroscopy (EDS)

Energy dispersive X-ray spectroscopy is an analytical technique for compositional analysis performed by detecting characteristic x-rays emitted from atoms ionized by high energy particles (electrons in STEM). The incident electron beam can excite core level electrons (ground state) into higher energy shells and form empty low energy inner shells. Empty states are filled instantly by relaxation of electrons from higher energy shells which emits x-rays with distinct energy corresponds to energy difference of the states. This process forms unique set of emission peaks in the spectrum (figure 1.8) providing information about the identity of the elements probed. The quantification in composition can be obtained with peak intensity analysis.

In combination with STEM, EDS spectroscopy provides sub nanometer resolution chemical compositional analysis complementary to STEM-EELS. Coherent electron beams are rastered across the region of interest resulting in characteristic x-rays emitted for each probe position. As shown in figure 1.8, large solid angle EDS detectors integrated into microscope above the specimen allows simultaneous EELS and EDS experiment with atomic resolution[48,49]. The accuracy of EDS depends on several parameters such as the thickness of the sample, absorption of emitted x-rays by both the specimen and holder (TEM grid), the escape probably of x-rays, multiple x-ray interactions (x-rays emitted isotopically in all directions in specimen), the complexity of the detector[50] and overlapping x-ray peaks of the elements probed[49].

1.11 Energy Resolved Photo Emission Spectroscopy (ER-PES)

Photo emission spectroscopy is a well-established surface sensitive spectroscopic technique based on the photoelectric effect. The compositions the top layers of material, i.e. vacuum/bulk interfaces can be obtained by measuring the intensity and the kinetic energies of the emitted electrons from surfaces irradiated with monochromatic x-rays. Each element emits electrons with specific kinetic energies as a result of inter orbital transitions thereby providing information about surface composition and chemical bonding. In this way, the oxidation states of the atoms can be mapped. The kinetic energy of the photoelectrons defined by; *KE = hυ – BE – Φspec* (Eq 1.11) in which the binding energy provides the identity and the oxidation state of the atom[51,52]

Photo electrons emitted from material after interacting with x-ray, escape the material with a kinetic energy which defines the elastic and inelastic mean free paths (IMFP) of the electrons (λ) and, therefore, the probing depth. By tuning the energy of the incident x-rays, the maximum probe depth in material can be varied[53]. Additional factors such as multiple scattering and elastic scattering can affect the probing depth. It should be noted that the photoelectrons are emitted from all the excited atoms across the material from surface into nominal maximum probing depth determined by kinetic energy of the photo electrons. Therefore, the elemental composition from PES represents the composition integrated from surface to the nominal probe depth. However, the photoelectrons at selected energy, the intensity contributions of the topmost monolayer into total intensity is about only 30% therefore significant contributions to the intensity arises from the composition of the elements beyond top layer (λ: 65%, λ: 85%, λ: 95%,)[53,54].

Chapter II

Elimination of high-k/SiGe Interface Defects by Selective Oxygen Scavenging

STEM-BF image of the MOSCAP device

Forming Gas Annealing
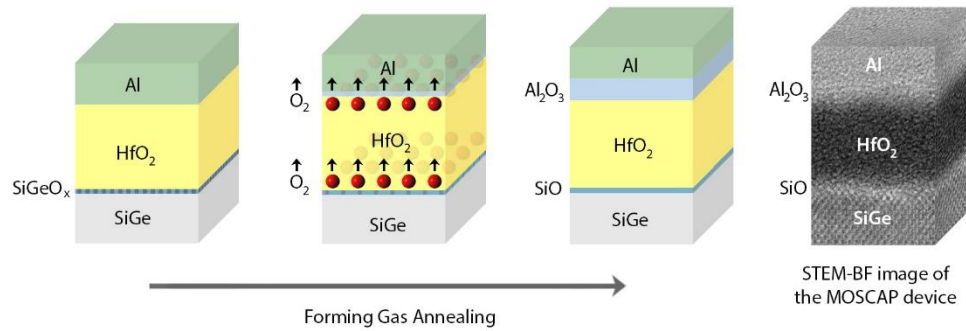
2.1 Introduction

Recently, density functional theory (DFT) calculations by Chagarov et al.[8] showed that even though SiO_2 or GeO_x formation at the $SiGe/HfO_2$ interface induces trap states in the band gap prior to forming gas anneal (passivation of Ge and Si dangling bonds by atomic hydrogen), a defect-free band gap can be established with monolayer Si-O termination of SiGe surfaces bonding to a HfO_2 high-k dielectric even prior to forming gas anneal. Preferential Si oxidation and selective Si-O formation on the SiGe surface is a challenging process during atomic layer deposition (ALD) oxidation due to excess oxygen-containing molecules in ALD reactors at elevated temperatures.[7,55] However, post-ALD processing may be employed to form very thin SiO_x-rich oxide/SiGe interfaces via an enthalpy-driven process of oxygen scavenging using a reactive gettering metal gate after ALD oxide deposition.

22

In this approach, GeO_x can be selectively reduced to Ge, forming a SiO_x-rich interface[21,56] by utilizing the difference in heat of formation between GeO_2 ($\Delta H_f^{\circ}{}_{solid}$ = -580.0 kJ/mol), GeO ($\Delta H_f^{\circ}{}_{solid}$ = -261.9 kJ/mol) and SiO ($\Delta H_f^{\circ}{}_{amorphous}$ = -423.42 kJ/mol)[57], SiO_2 ($\Delta H_f^{\circ}{}_{solid}$ = -905.49 kJ/mol)[58].

Oxygen scavenging by reactive metal gates is a well-known technique used for thinning low-k interfacial oxide layers in MOS gate stacks[59,60]. Previously, a reactive metal Ti gate was utilized to remove the IL between HfO_2 and Si, dissolving oxygen by Ti, which stayed metallic after the scavenging process[59] Furthermore, oxygen scavenging using Al gates, due to this metal's high oxide formation enthalpy (Al_2O_3: $\Delta H_f^{\circ}{}_{solid}$ = -417.45 kJ/mol), was reported to induce GeO_x decomposition at a high-k/SiGe interface[61]. Selective oxygen scavenging from the GeO_x component of the IL in $Al/Al_2O_3/Si_{0.55}Ge_{45}$ gate stacks was observed, resulting in low interface defect density.[6]

HfO_2 is the preferred gate dielectric in CMOS due to the combination of high thermal stability, high permittivity, and sufficiently large band gap[62]. Oxygen scavenging from mixed Si-Ge oxide ILs at the HfO_2/SiGe interface will be distinct from those with Al_2O_3 gate oxides because HfO_2 is a relatively poor oxygen diffusion barrier compared to Al_2O_3.[63] In this chapter, the impact of oxygen scavenging using Al gettering metal gate with HfO_2/SiGe MOS device was investigated. The oxygen scavenging process was utilized to thin the interlayer and form a Si-rich interface. A successful selective scavenging process which provides more than a 10× reduction in total interface trapped charge density across the band gap with a very thin residual IL was demonstrated in Al-gated devices.

2.2 Fabrication of MOSCAPs for Oxygen Gettering

As illustrated in figure 2.1, the MOSCAPs fabricated on epitaxially grown, strained $Si_{0.7}Ge_{0.3}$ on p-type Si (100) provided by Applied Materials. Samples were degreased for one minute by sonication in methanol and rinsed with acetone, isopropyl alcohol, and deionized (DI) H_2O. Before ALD oxide deposition, native oxides were removed by cyclic cleaning in HF (2%) and DI water 2.5 times for 1 minute each half cycle ending with HF. After N_2 drying, samples were dipped into ammonium sulfide solution (25% $(NH_4)_2S$) for 15 minutes for sulfur surface passivation[13]. After rinsing with DI water for 30 seconds and drying with N_2, samples were transferred into the ALD system via a load lock with approximately one minute of air exposure.

High-k oxides were grown using a Beneq TFS200 cross flow, hot wall ALD reactor at 275°C using $HfCl_4$ at 200°C as the hot source precursor and water as the oxidant source. The HfO_2 deposition was carried out using 250 ms pulses of $HfCl_4$ with 500 ms pulses of H_2O. Growth rates for the processes was found to be ~1Å/cycle extracted from oxide thicknesses obtained from cross-sectional STEM images. Ar carrier gas at 2-3 Torr was used for all processes and a 6 second purge was employed between pulses. Control samples with Ni gates and samples with reactive Al gates were deposited with a shadow mask (50 nm thick – 150 um diameter) using a Denton 502A thermal evaporator in $< 2 \times 10^{-6}$ torr vacuum. Native oxide was removed with one minute of Ar plasma treatment and Al back contacts were subsequently sputtered in Denton Discovery 18 sputter system.

Samples were annealed sequentially at 300°C, 330°C and 350°C for 10 minutes in forming gas (5% H_2, 95% N_2) in an Ulvac Mila-3000 minilamp annealing system; this was

24

a carefully optimized procedure for Ni gated nanolaminate MOSCAP devices. Capacitance-voltage (C-V) were recorded after each annealing step to determine the optimum annealing times at each temperature. Additional annealing at higher temperature, 400C, increased the defect density. It is noted that the annealing procedure was optimized only for one type of sample. Electron transparent cross-sectional TEM specimens (<50nm) from selected MOSCAP devices prepared with using a FEI-Scios Ga focus ion beam (FIB). The structure of the high-k/SiGe gate stacks were studied with high resolution scanning transmission electron microscopy (HR-STEM) using a FEI Metrios TEM and a JEOL-ARM300F in STEM mode operating at 200 kV. High-angle annular dark field (HAADF) and bright field (BF) mode was used for imaging.
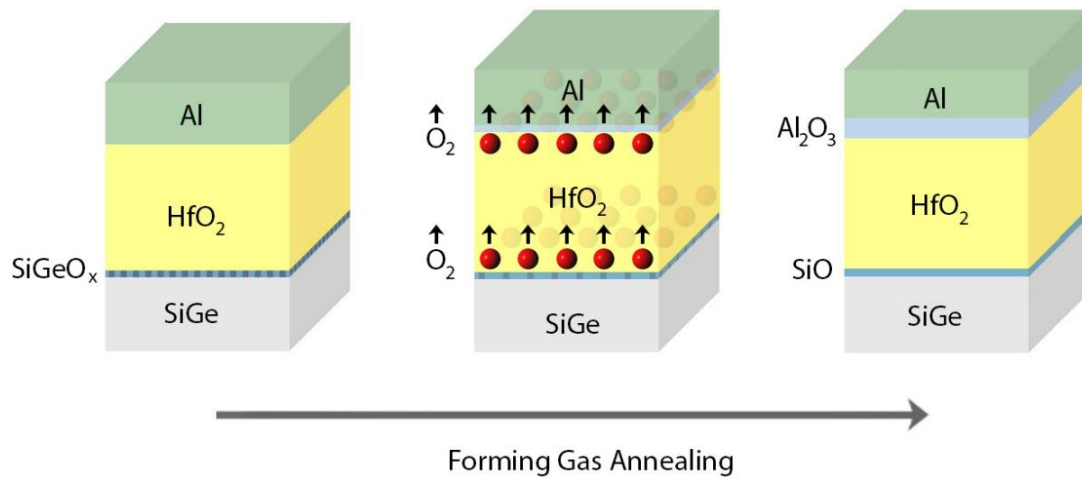
Figure 2.1 Selective oxygen scavenging process in Al/HfO$_2$/SiGe/Si. The interface defects illustrated with dots in blue region between HfO$_2$ and SiGe. Oxygen scavenged from IL denoted by red balls with arrows indicating oxygen diffusion in HfO$_2$. Formation of Al$_2$O$_3$ due to oxidation of Al metal gates illustrated with blue region between HfO$_2$ and Al. After FGA, the interface defects eliminated by GeO$_x$ reduction and SiO formation.

2.3 Electrical analysis of Ni/HfO$_2$/SiGe and Al/HfO$_2$/SiGe MOSCAPs

Electrical characterization of the MOSCAPs was performed using a Keysight B1500 at room temperature. Leakage currents (I_g-V_g) were measured from 2V to -2V DC gate bias, and multi-frequency impedance (C-V) along with conductance (G-V) measurements were obtained from 10 kHz to 1 MHz in the same bias range.

Ni and Al-gated HfO$_2$/SiGe/Si MOSCAPs with identical gate oxide deposition were compared with electrical measurements. As seen in figure 2.2, leakage currents for Ni-gated control devices ($<2\times10^{-4}$A/cm^2) were found to be approximately 100× higher in comparison with the Al-gated devices ($<2\times10^{-6}$A/cm^2) measured in accumulation at Vg = -1V.

Interface defects were characterized at room temperature with multi-frequency C-V and G-V spectroscopy measurements performed at 10 kHz – 1 MHz from inversion of 2V to accumulation of -2V, and the results shown in figure 2.3 (a-d) indicate two notable differences between the Ni control and Al gates. (1) First, the depletion capacitance induced by defects at the high-k/SiGe interface has a much smaller D_{it} hump for Al gettering gate devices in comparison to Ni controls which indicates a better interface between HfO$_2$ and SiGe with Al gates. The depletion conductance also shows a lower peak value for the Al-gated device.
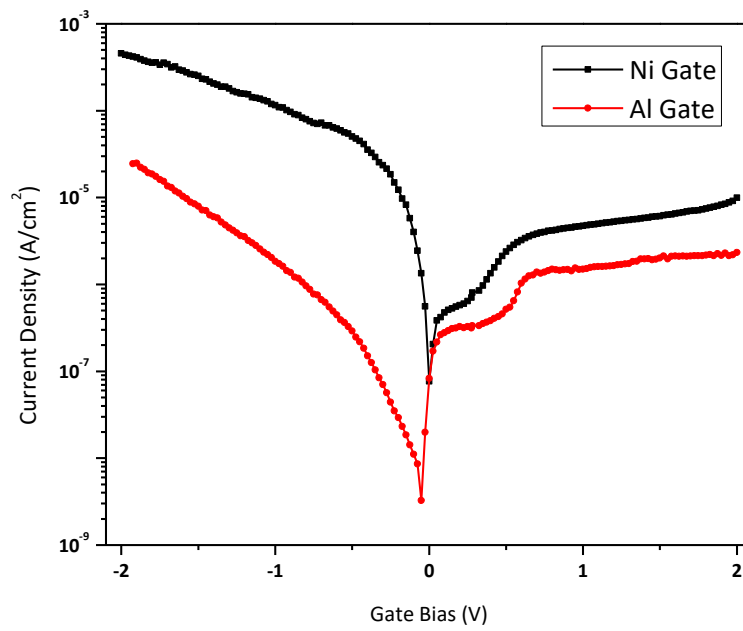
Figure 2.2 Leakage current across Ni/HfO₂/SiGe/Si and Al/HfO₂/SiGe/Si devices, The Al-gated devices show more than 10× lower leakage current in comparison to the Ni-gated device.
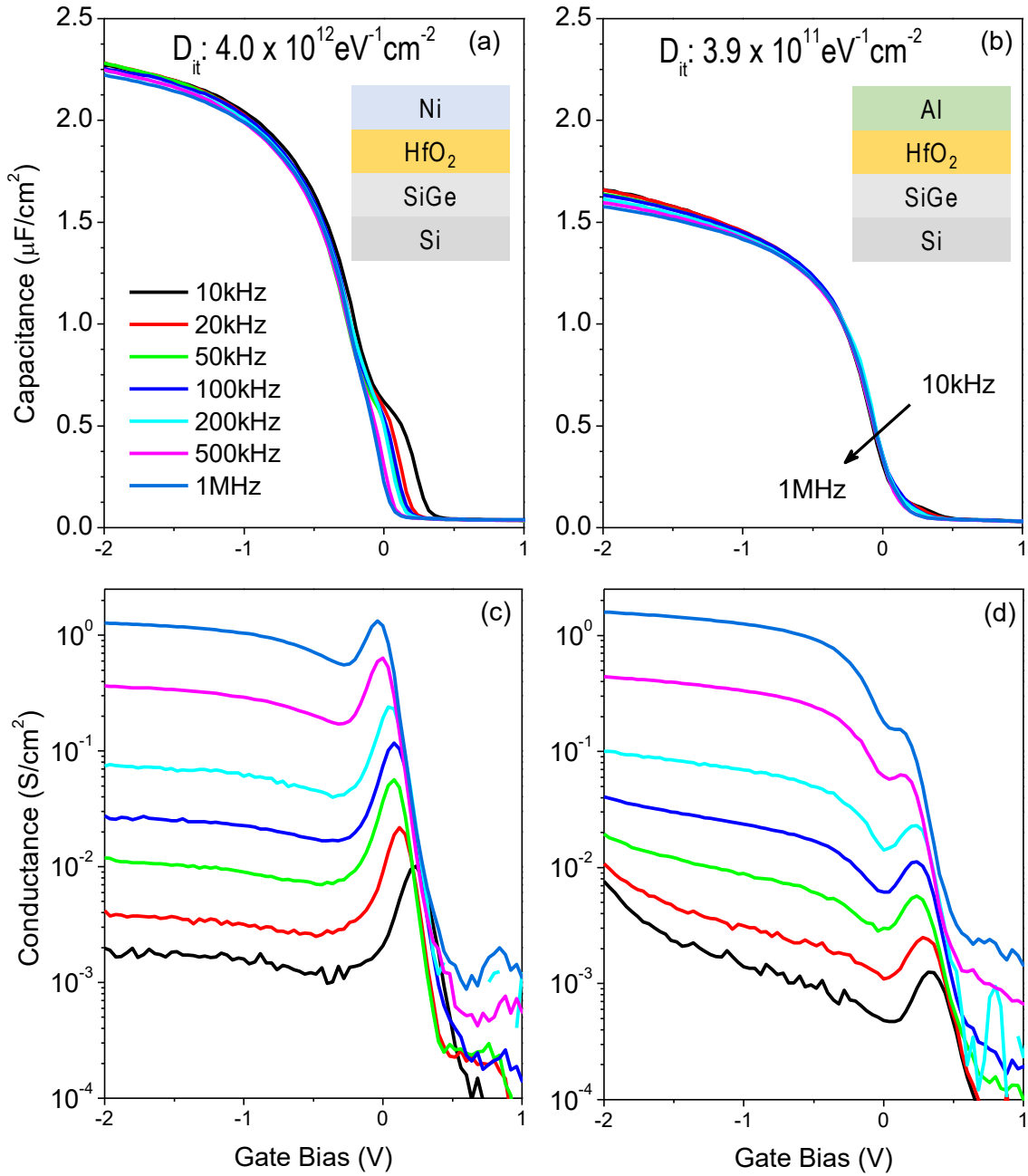
Figure 2.3 C-V and G-V graphs of Ni/HfO₂/SiGe and Ni/HfO₂/SiGe MOSCAPs.
Multifrequency C-V (a-b) and G-V (c-d) graphs of Ni and Al-gated MOSCAPs from 10 kHz to 1 MHz. Insets illustrate the device structures. The Al-gated devices exhibit smaller D_{it} humps in the depletion region and lower peak conductance. Inset peak D_{it} values were calculated with the full interface state model and show a 10× reduction in defect density with reactive Al gates in comparison to Ni controls.
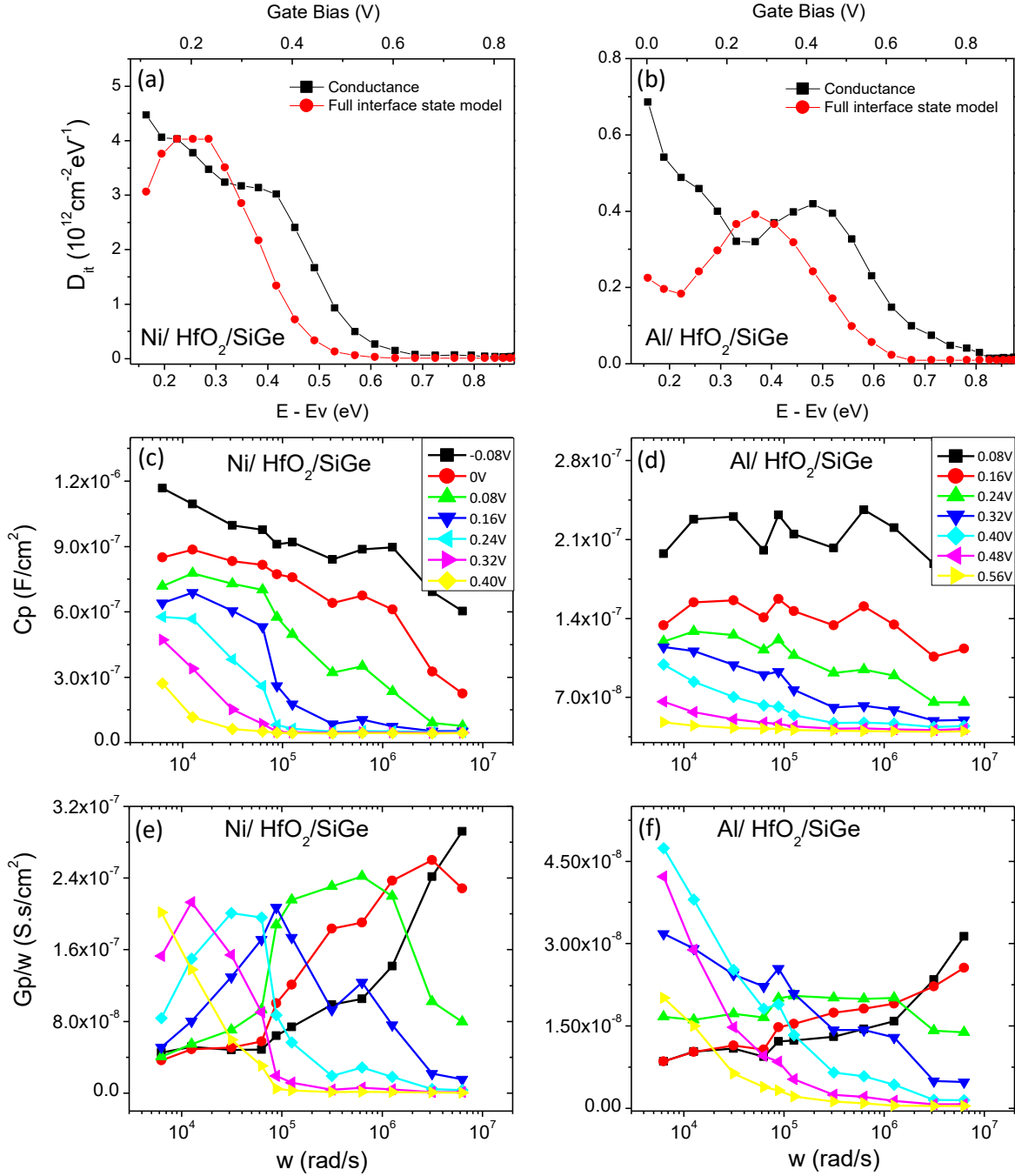
Figure 2.4 Interface defect density analysis of Ni/HfO₂/SiGe/Si and Al/HfO₂/SiGe/Si
(a-b) Comparison of defect distribution obtained with conductance and full interface state models. (c-d) $C_P - \omega$ graph, (e-f) $G_P/\omega - \omega$ graph. Both models show similar maximum defect density above the valence band with a small shift in energies. This difference can be attributed similar peak values of Gp/ω seen in several bias points shown in figure e-f. Al-gated devices do not show an obvious peak for Gp/ω; however, the conductance is an order of magnitude lower in comparison with Ni-gated device.

The defect density was calculated from the maximum of G_p/ω versus ω using the conductance method [64] as shown in figure 2.4. The peak of D_{it} value obtained with;

$$D_{it} = \frac{2.5}{q}(\frac{G_p}{\omega})_{max} \quad Eq \ 2.1$$

Due to similar G_p/ω peak values for several bias points, defect density was further analyzed with the full interface state model[65] by fitting capacitance and conductance curves for each bias point as shown in figure 2.4 and 2.5.
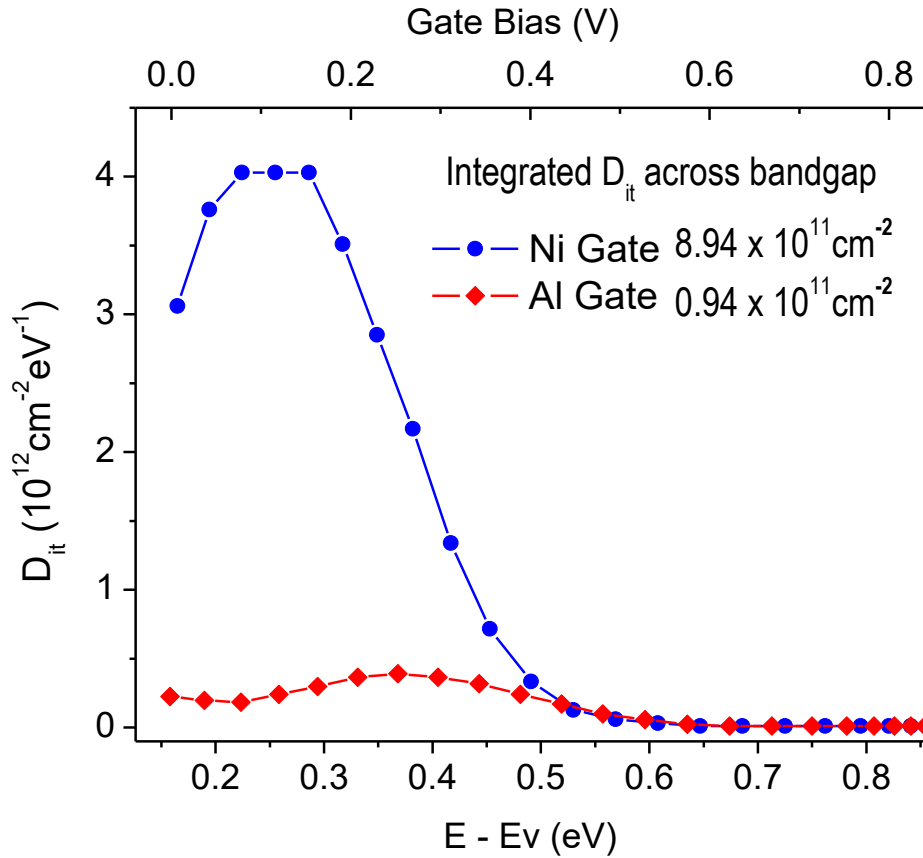
Figure 2.5 Interface defect density distributions for Al and Ni-gated MOSCAPs. D_{it} values extracted with the full interface state model. In comparison with Ni controls, Al gettering gate devices show lower defect densities across the full energy range of the band gap. The integrated defect densities indicate a ~10× reduction in total defect density across the bandgap with Al-gated device.

As shown in figure 2.4 a-b, the values extracted with both models are consistent and show maximum defect density close to the valence band; however, Al-gated devices have a lower defect density across entire band gap in comparison to Ni-gated devices. Peak defect densities of 4.0×10^{12} eV^{-1}cm^{-2} for Ni-gated and 3.9×10^{11} eV^{-1}cm^{-2} for Al-gated devices were observed at 0.25 eV and 0.36 eV above from valence band respectively. Furthermore, the total integrated defect density was also found to be an order of magnitude lower for Al gates. Both the conductance and full interface state models consistently indicate at least a 10$\times$ reduction in interface defect density between HfO$_2$/SiGe with Al gettering gates as compared to the Ni control gates.

The second difference between Ni control and Al gate samples is that the accumulation capacitance densities (C$_{max}$) differ: for Ni gates C$_{max}$ = 2.3 μF/cm^2 while for Al gates C$_{max}$ = 1.6 μF/cm^2. This difference can be attributed mainly to a thicker gate oxide being formed with Al gate metal because the Al is in direct contact with HfO$_2$ oxidizes to Al$_2$O$_3$ via oxygen scavenged from the interface and possibly from excess oxygen in the HfO$_2$[66]. In addition, Ge atoms decomposed from GeO$_x$ on SiGe may possibly regrow on SiGe surface and contribute to the lower capacitance density as it was observed by Kim et al for SiO$_2$ decomposition at HfO$_2$/Si interfaces[59].

2.4 Structural analysis of MOSCAPs with Gettering Metal Gate

The hypothesis of Al gates forming thicker oxide is confirmed with HR-STEM HAADF and BF images of the MOSCAPs shown in figure 2.6. Al gates show a 2.7 nm thicker gate oxide as compared to the Ni-gated control. The bright field image in figure 4b clearly indicates the formation of a second amorphous oxide layer in the Al gate region. The most significant difference between Ni and Al-gated devices in the STEM images is the interface region where Al gates show a very thin interface layer compared to Ni-gated devices. In some locations, a few monolayers of oxide or even direct bonding of HfO_2 to the channel is apparent for the Al gates.
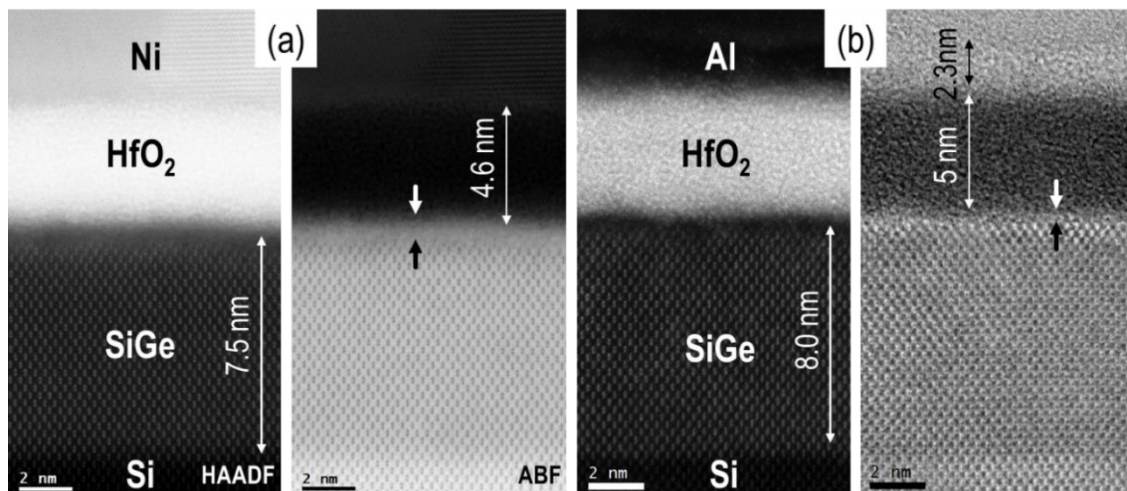
Figure 2.6 HR-STEM images of control Ni (a) and Al (b) gate HfO_2/SiGe MOSCAPs. In these images, oxide structures and regions defined according to contrast difference in which Ni-gated device displays two regions, gate oxide and IL in contrast to Al which has additional layer of 2.3nm on gate oxide. In comparison to Ni control, the Al-gated device shows sub 0.5nm interfacial oxide layer in various locations.

2.5 Compositional Analysis of Control and Al Gettering Gate MOSCAPs

Local compositional analysis of the interfaces investigated with energy dispersive X-ray spectroscopy (EDS) and electron energy loss spectroscopy (EELS) performed simultaneously using same FEI Metrios TEM and a JEOL-ARM300F microscopes in STEM mode operating at 200 kV. Figure 2.7 shows the composition of the Ni-gated device. Orange and blue dashed lines intercept half max of Hf and O peak correspondingly and indicates interface layer. The Si and Ge composition in IL denoted with green and black arrows indicates 0.9nm thick $SiGeO_x$ formation. The enhanced Ge composition at the SiGe surface is pointed with red arrow. The elemental composition of low defect interface in Al-gated MOSCAPs is shown in figure 2.8. Black and green dashed lines intercept the half peak values of the Si and Ge elemental intensity profile and define the interface layer region. As indicated by the black and green arrows, the interface is Si-rich unlike Ni gated device. This is consistent with low defect interface formation by GeO_x suppression. Figure 2.9 shows EDS analysis of both devices (acquired simultaneously with EELS) and show very similar results. The data are consistent with the formation of a 1-2 monolayer thick Si-rich interface oxide for the Al-gated HfO_2/SiGe MOSCAPs that exhibits very low D_{it}. The gate stack is found to have four oxide regions: Al_2O_3, $Al_xHf_xO_x$, HfO_2, and SiO_x (IL). With respect to the Hf peak, the oxygen peak is shifted toward the Al gate. The Al signal tail extends into gate oxide indicating Al oxidation at the HfO_2/Al gate interface. The orange dashed line intercepts the half peak of Hf and the tail of the Hf extends into Al. This is consistent with inter-diffusion forming a $Hf_xAl_xO_x$ region, although interface roughness will also contribute to apparent intermixing. Extension of the oxygen tail into the Al gate beyond the Hf peak is consistent with Al_xO_y formation.
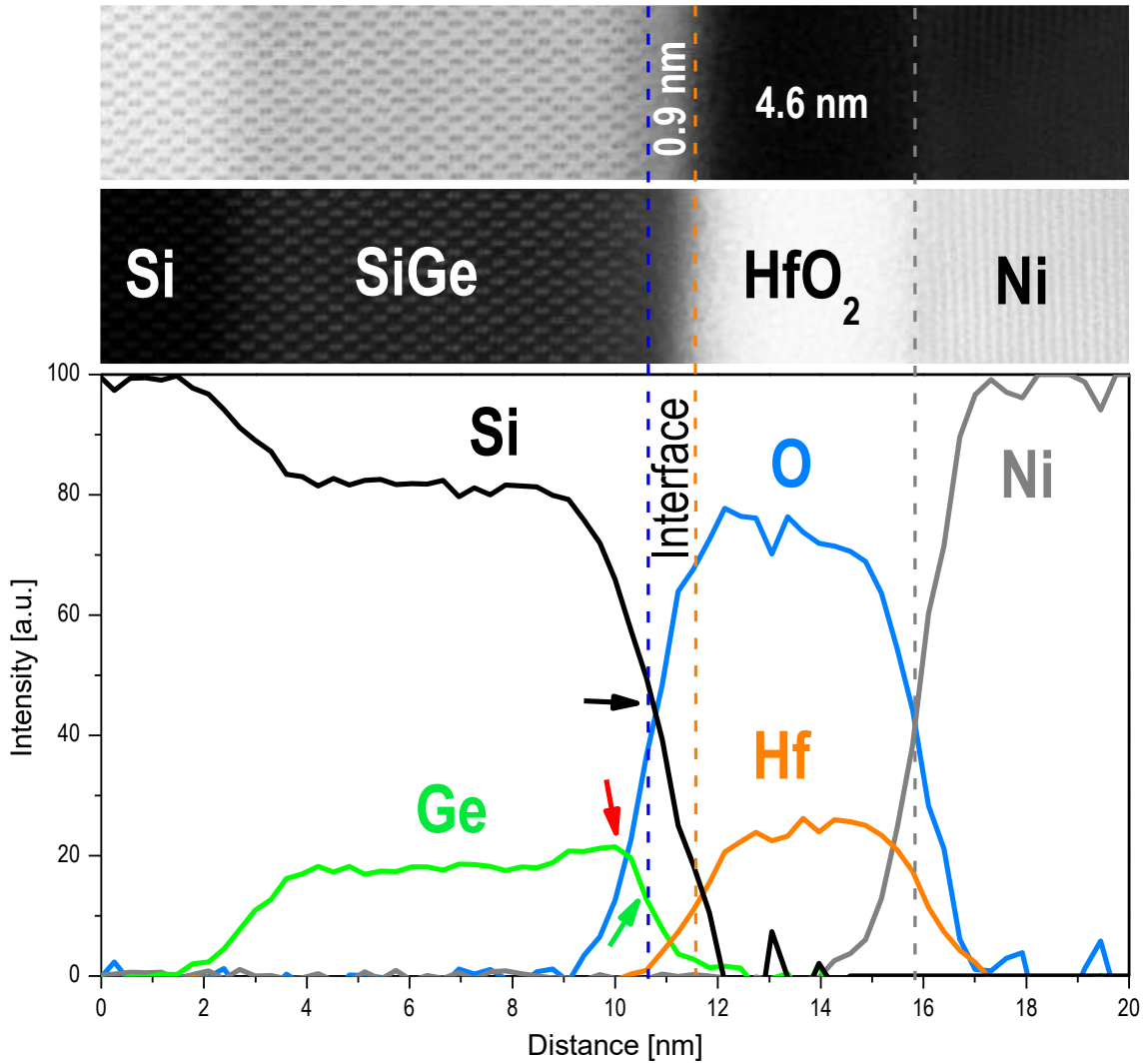
Figure 2.7 STEM images and corresponding EELS analysis of Ni/HfO₂/SiGe/Si device. In this STEM image, the regions of gate oxide are defined using compositions obtained with EELS spectra. Similar to the regions defined in STEM image of Ni/HfO₂/SiGe/Si in Figure 2.6, EELS revealed two regions in the Ni/HfO₂/SiGe/Si gate stacks. Blue and orange dashed lines intercept the half peak values of the O and Hf signals and delineate the SiGe-HfO₂ interface. Black and green arrows denote Si and Ge composition on SiGe surface in which a Ge enrichment at the surface composition is detected. Hf and O peaks have small offset and O shifted towards SiGe indicates IL formation. The gray dashed line intercepts the half max of the Ni and the O at the same points indicate sharp oxide Ni interface.
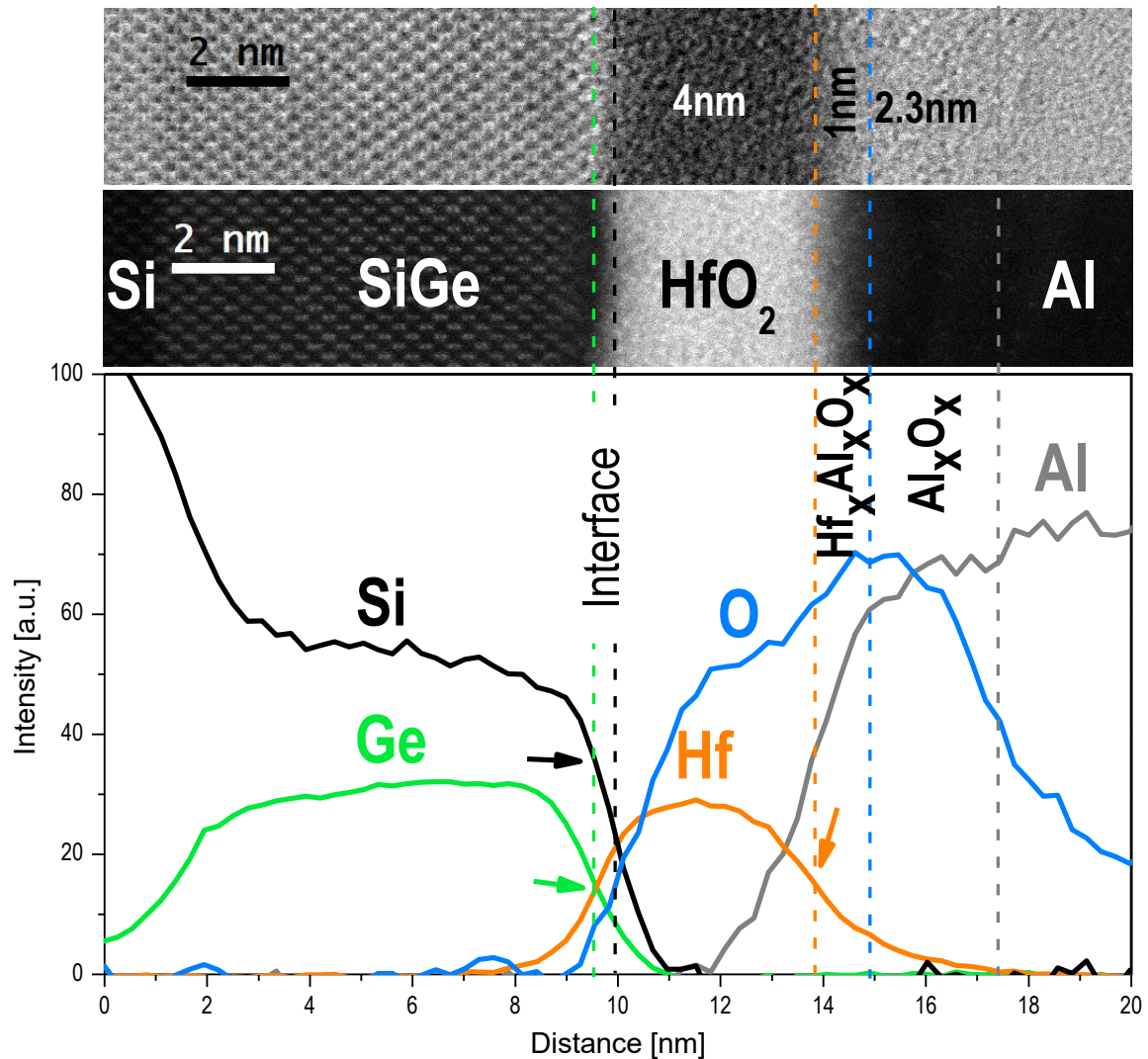
Figure 2.8 STEM images and corresponding EELS analysis of Al/HfO₂/SiGe/Si device. In this STEM image, the regions of gate oxide are defined using compositions obtained with EELS spectra. In contrast to three regions defined in STEM image of Al/HfO₂/SiGe/Si in Figure 4, EELS revealed four regions in the Al/HfO₂/SiGe/Si stacks. Green and black dashed lines intercept the half peak values of the Si and Ge signals and delineate the SiGe-HfO₂ interface. Black and green arrows denote Si and Ge composition on SiGe surface in which a Si rich interface composition is detected. The orange line intercepts the half max of the Hf signal. The Hf asymmetrically tails into the Al gate metal indicating that Hf and Al intermix. The blue dashed line indicates the max peak of oxygen which is shifted with respect to the Hf peak towards the Al gate. The Al peak tail extends into the gate oxide consistent with Al oxidation. The gray dashed line separates the regions of oxidized Al and elemental Al metal.

This thicker gate oxide formed by local Al oxidation is consistent with the 100× lower leakage and 0.7 uF/cm^2 reduction in C_{max} observed in I-V and C-V measurements. The data is consistent with the Al gate either decomposing GeO_x at the interface or removing GeO from the interface via oxygen scavenging[6] to form an SiO_x-rich interface and an order of magnitude reduction in interface defect density.
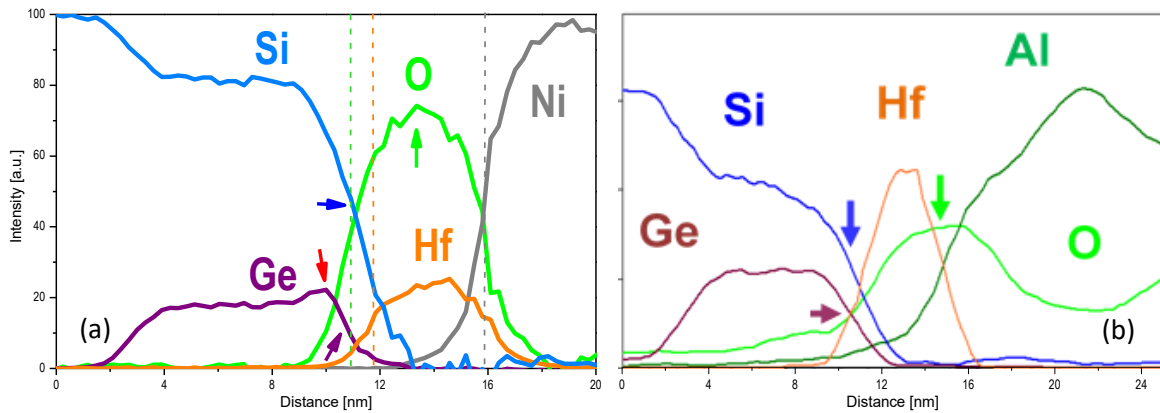
Figure 2.9 EDS analysis of Ni/HfO₂/SiGi/Si (a) and Al/HfO₂/SiGi/Si (b) devices. The green arrow in b shows the peak of the oxygen distribution are shifted with respect to the Hf peak and the oxygen tails extend into the Al consistent with Al oxidation causing a reduction in capacitance due to thicker AlO_x oxide formation. In contrast, Ni gated device in a, shows Hf and O peak offset smaller and O extending towards SiGe surface indicates thicker interface layer formation. This is consistent with EELS analysis. Blue and brown arrows show Si and Ge composition at the interface layer. Ni gated device shows significant Ge enrichment at the SiGe surface unlike Al gated device which shows Si rich IL formation.

2.6 Simulation of HfO$_2$/a-SiO/SiGe interface with DFT

Formation of low defect density interface with SiO$_x$ composition is studied with density functional theory (DFT). The simulation method is explained at the introduction in chapter 1.5 and more detailed documentation is presented elsewhere.[8]

The *a*-HfO$_2$ sample was stoichiometric and included 40 Hf and 80 O atoms. Several a-HfO$_2$ samples were generated using hybrid classical and DFT-MD simulations including annealing, cooling and relaxation. The amorphous sample quality was verified via radial-distribution function (RDF) main peak positions, average nearest neighbor numbers, nearest neighbor distributions, and DFT calculated[34] band gaps demonstrating good correlation to available simulated and experimental reference properties.[35] The sample with the best match to experimental data was selected and used for simulations. The amorphous samples were generated to match the SiGe (001) surface area.

The density of states (DOS) versus energy shown in figure 2.10 a indicates a defect-free band gap for the near-interface region of the SiGe channel, very similar to a SiGe bulk crystal. Figure 2.10 b shows the corresponding bonding coordination of an interfacial a-SiO layer. In the simulation cell, there are two 3- and 5-fold coordinated interfacial Si atoms along with 4-fold interfacial Si which do not create any mid-gap or band-edge states. These 3- and 5- fold coordinated Si atoms have multiple bonds to oxygen which is consistent with the interfacial Si atoms having primarily ionic bonding, so a range of coordination can be tolerated.
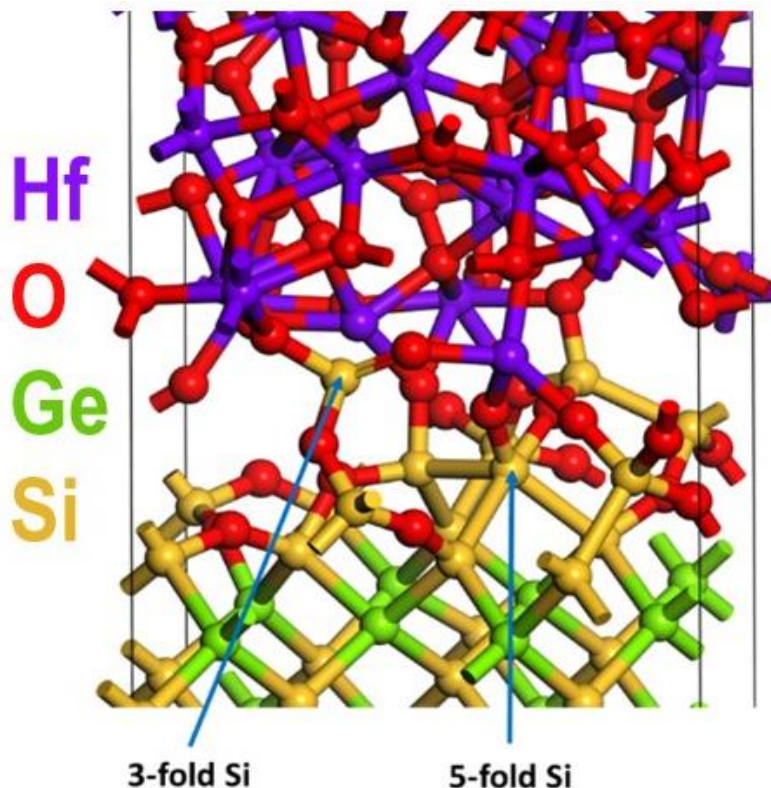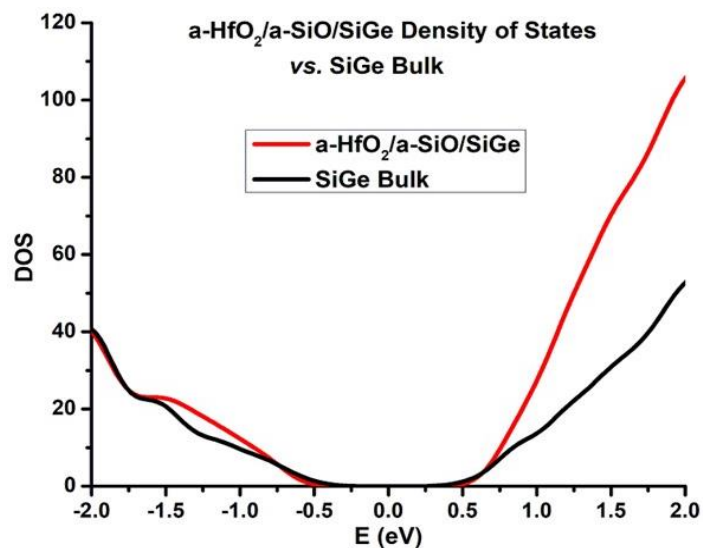
Figure 2.10 Density of states and interface bonding for bulk SiGe and HfO₂/SiO/SiGe. DFT results for annealed and relaxed a-HfO₂/a-SiO/SiGe shows no energy states in band gap very similar to bulk SiGe. Corresponding interface structures illustrates three-fold Si and 5-fold Si along with 4- fold Si bonding. Note the interfacial Si bonded to O which is in nonstandard coordination, consistent with ionic bonding.

2.7 Conclusion

Oxygen reactive Al gate were employed to reduce interface defects by scavenging oxygen from the SiGe/HfO$_2$ interface. In comparison with control Ni-gated device, thinner IL formation in Al gated MOSCAPs was demonstrated using STEM. Lower interface defect formation with Al gettering gate coincided with Si-rich interlayer formation as shown by STEM-EELS-EDS analysis. These results suggest that Al gates scavenge oxygen from the IL forming a thinner interlayer which contains less GeO$_x$. By having less GeO$_x$ at the interface, this process reduces interface defects. While Al-gated devices exhibited a remarkable D$_{it}$ reduction, significant decrease in C$_{max}$ is also seen due to formation of Al$_2$O$_3$ in contact with HfO$_2$. The Stable defect-free interface formation with a few monolayers of SiO on SiGe was demonstrated with DFT simulations[34]. The extremely thin interface with ultra-low defect densities between SiGe/HfO$_2$ proves that a thick IL is not necessary.

2.8 Acknowledgment

Chapter III

Suppression of Defects at high-k/SiGe Interface with Remote Oxygen Scavenging

Forming Gas Annealing

TEM image of the MOSCAP device
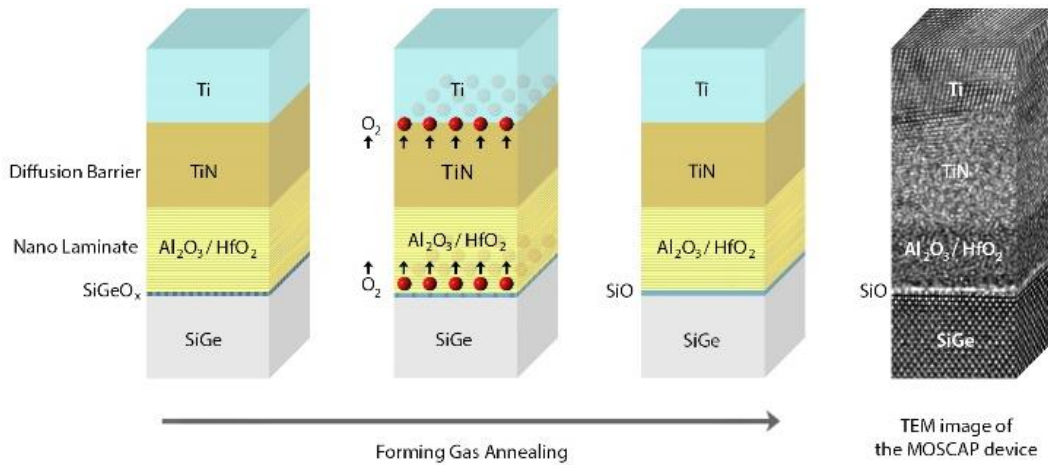
3.1 Introduction

Direct oxygen scavenging with Al metal gates causes an undesired reduction in C_{max} via formation of a lower-k aluminum oxide layer in series with the HfO_2 gate dielectric as presented in previous chapter. This unwanted C_{max} reduction can be prevented with remote oxygen scavenging by using diffusion barriers such as TiN. In this study, remote oxygen scavenging with Ti gates encapsulated between TiN and Pd was investigated to prevent this unwanted capacitance reduction[59] (denoted as a Pd/Ti/TiN gate structure). For this study, instead of HfO_2 gate oxide, Al_2O_3-HfO_2 nanolaminate oxide structures (grown with 4 super cycles consisting of 9 cycles of HfO_2 and one cycle of Al_2O_3) were chosen since Al_2O_3 is known to be a good diffusion barrier for Ge out diffusion[63,67]. Ge out diffusion into the gate oxide might induce reliability issues for device operation; therefore, nanolaminate HfO_2-Al_2O_3 structures were employed to prevent GeO_x diffusion to the gate metal.

40

3.2 Fabrication of MOSCAPs for Remote Oxygen Gettering

As illustrated in figure 3.1, the MOSCAPs fabricated on epitaxially grown, strained $Si_{0.7}Ge_{0.3}$ on p-type Si (100) provided by Applied Materials. Samples were degreased for one minute by sonication in methanol and rinsed with acetone, isopropyl alcohol, and deionized (DI) H_2O. Before ALD oxide deposition, native oxides were removed by cyclic cleaning in HF (2%) and DI water 2.5 times for 1 minute each half cycle ending with HF. After N_2 drying, samples were dipped into ammonium sulfide solution (25% $(NH_4)_2S$) for 15 minutes for sulfur surface passivation[13]. After rinsing with DI water for 30 seconds and drying with N_2, samples were transferred into the ALD system via a load lock with approximately one minute of air exposure.

High-k oxides were grown using a Beneq TFS200 cross flow, hot wall ALD reactor at 275°C using $HfCl_4$ at 200°C as the hot source precursor and $Al(CH_3)_3$ (trimethyl aluminum, TMA) at 25°C. Both processes used water as the oxidant source. The HfO_2 deposition was carried out using 250 ms pulses of $HfCl_4$ with 500 ms pulses of H_2O, and the Al_2O_3 deposition was carried out using 1 s pulses of TMA followed by 500 ms pulses of H_2O. Growth rates for both processes were found to be ~1Å/cycle extracted from oxide thicknesses obtained from cross-sectional scanning transmission electron microscopy (STEM) images. Ar carrier gas at 2-3 Torr was used for all processes and a 6 second purge was employed between pulses. Control samples with Ni gates was deposited with a shadow mask (50 nm thick – 150 um diameter) using a Denton 502A thermal evaporator in $< 2\times10^{-6}$ torr vacuum.

Gettering gate stacks with Ti encapsulated between TiN and Pd (7/30/30 nm thick Pd/Ti/TiN) were sputtered using the same shadow mask at 5 mTorr without a vacuum break at a power of 200W/200W/100W for 30/55/120sec (Pt/Ti/TiN) respectively with a Denton Discovery 18 sputter system. The TiN acts as a diffusion barrier, and the Pd prevents ambient oxidation of the gate stack as well as promotes the dissociation of hydrogen during forming gas anneal. Native oxide was removed with one minute of Ar plasma treatment and Al back contacts were subsequently sputtered in the same tool.
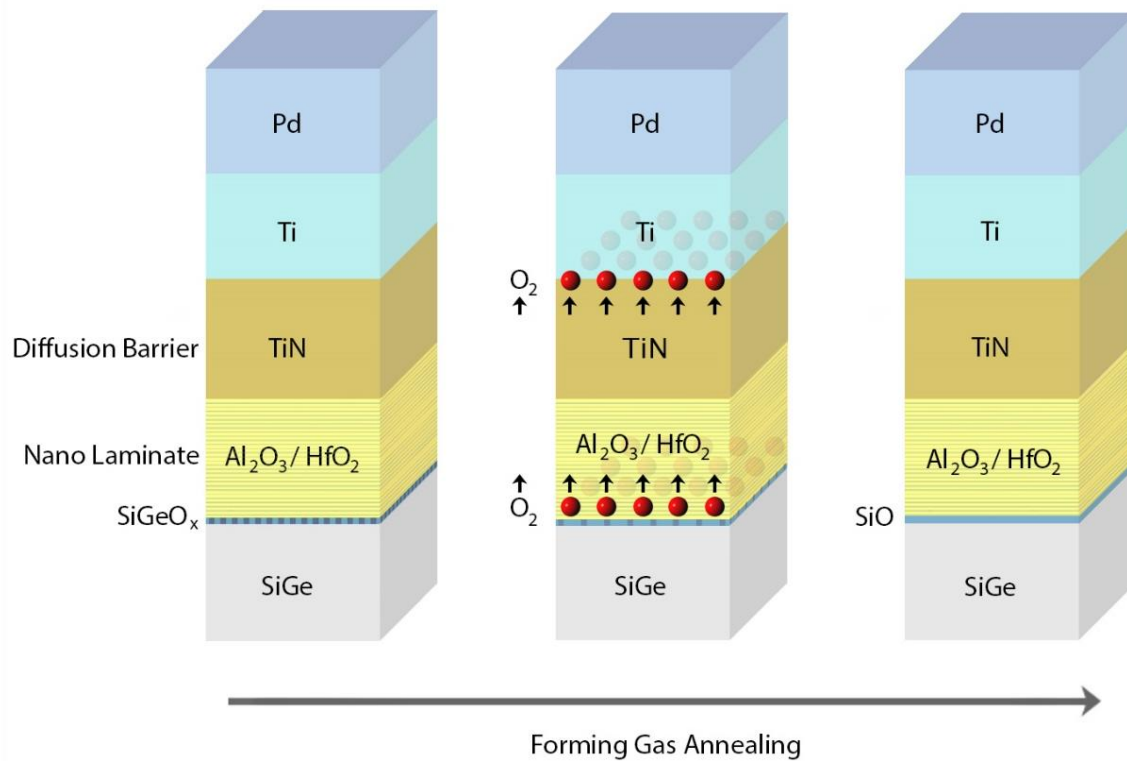
Figure 3.1 Remote oxygen scavenging in Pd/Ti/TiN/NL/SiGe/Si MOSCAP device. Oxygen gettering Ti metal gate encapsulated between Pd and TiN which is good diffusion barrier. TiN prevents oxidation of Ti metal. The red balls illustrate oxygen atoms scavenged from IL moving towards Ti layer during forming gas annealing.

Samples were annealed sequentially at 300°C, 330°C and 350°C for 10 minutes in forming gas (5% H_2, 95% N_2) in an Ulvac Mila-3000 minilamp annealing system; this was a carefully optimized procedure for Ni gated nanolaminate MOSCAP devices.

Capacitance-voltage (C-V) were recorded after each annealing step to determine the optimum annealing times at each temperature. Additional annealing at higher temperature, 400C, increased the defect density. It is noted that the annealing procedure was not optimized independently for each type of samples but, instead, this optimized FGA for the Ni gated nanolaminate MOSCAP was employed for all samples.

Pd/Ti/TiN gettering gate metal was also tested on only HfO_2 gate oxide and a similar gettering process was observed. However, the nanolaminate structure was preferred for further compositional analysis due to the improved diffusion barriers formed with the nanolaminate which prevents Ge out diffusion and provides lower leakage.

Electron transparent cross-sectional TEM specimens (<50nm) from selected MOSCAP devices prepared with using a FEI-Scios Ga focus ion beam (FIB). The structure of the high-k/SiGe gate stacks were studied with high resolution scanning transmission electron microscopy (HR-STEM) using a FEI Metrios TEM and a JEOL-ARM300F in STEM mode operating at 200 kV. High-angle annular dark field (HAADF) and bright field (BF) mode was used for imaging.

3.3 Electrical analysis of MOSCAPs with Remote Gettering Gate

Figure 3.2 shows leakage current density across the gate oxide for Ni and Pd/Ti/TiN gated NL/SiGe/Si MOSCAP devices and similar leakage current density of $1.3 \times 10^{-6} A/cm^2$ and $3.5 \times 10^{-6} A/cm^2$ at -1V is seen. Apart from this, NL devices with Ni gate shows lower leakage characteristics in comparison to HfO_2 gate oxide with Ni devices in figure 2.2. This is result of Al_2O_3 incorporation into HfO_2 which is known to be good diffusion barrier and the Al_2O_3 incorporation into HfO_2 may increase the band gap of the gate oxide[63].

Multi-frequency C-V and G-V measurements presented in figure 3.3 (a-d). Comparison of the C-V curves show two notable differences between the Ni-gated control capacitors and the MOSCAPS with Pd/Ti/TiN gates. First, the C_{max} is 3.5 $\mu F/cm^2$ for the oxygen scavenging gates versus 2.25 $\mu F/cm^2$ for the Ni-gated controls.
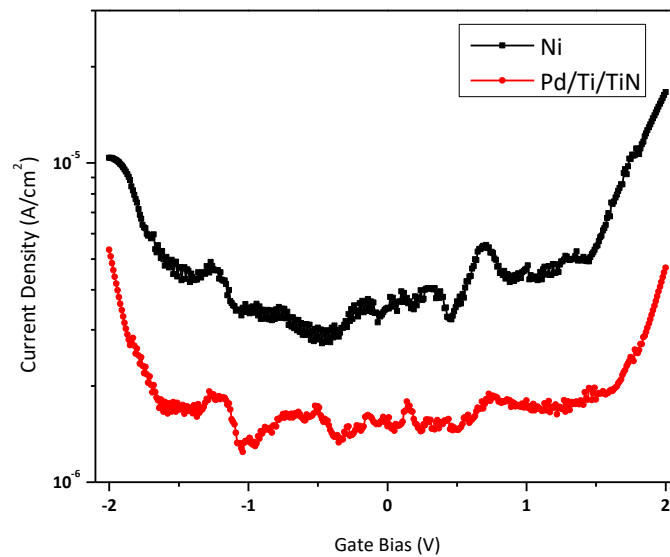
Figure 3.2 Leakage current across Ni/NL/SiGe/Si and Pd/Ti/TiN/NL/SiGe/Si devices. In comparison to Ni-gated device, Pd/Ti/TiN gated device shows slightly lower leakage current.
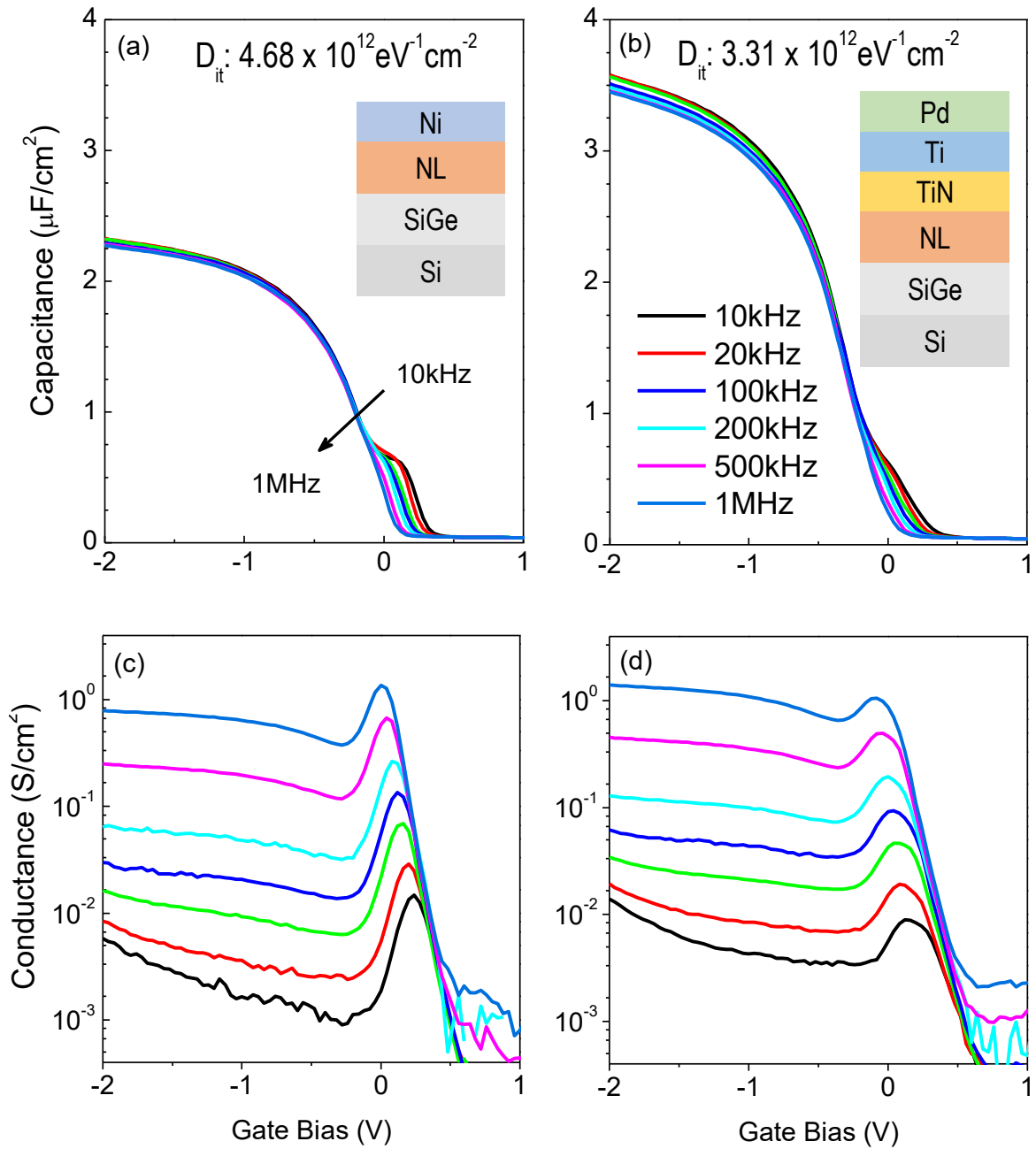
Figure 3.3 Multifrequency C-V and G-V graphs of Ni and Ti gated MOSCAPs. (a-b) C-V (c-d) G-V plots (10kHz-1MHz) from accumulation -2V to depletion 1V for gettering Pd/Ti/TiN gates and Ni control MOS capacitors. Inset schematics illustrate the device structures. Peak D_{it} values in the band gap are shown. In comparison with Ni gates, Ti-gated MOSCAP show a lower D_{it} hump and corresponding lower conductance peak. Inset peak D_{it} values were obtained from the full interface state model. Ti-gated devices show a higher accumulation capacitance of 3.5uF/cm^2 40% higher than Ni-gated devices.

The second significant difference in C-V curves comparing the Ni- and Pd/Ti/TiN-gated samples is the hump in depletion capacitance induced by defects at the high-k/SiGe interface as shown in figure 7. In comparison with the Ni-gated devices, Pd/Ti/TiN gated devices have a smaller D_{it} hump, indicating a better interface between HfO_2 and SiGe with Pd/Ti/TiN vs Ni gates. Peak D_{it} of 3.31×10^{12} eV^{-1}cm^{-2} for Pd/Ti/TiN gates and 4.68×10^{12} eV^{-1}cm^{-2} for Ni were calculated according to the full interface state model[68] and similar values were obtained with the conductance method as shown in figure 3.4 and 3.5. The defect distributions across the band gap calculated using the full interface state model shown in figure 3.4 indicate less charge trap formation with Pd/Ti/TiN gates in comparison to Ni gates. Both the conductance and full interface state models show ~30% reduction in D_{it} consistent with the formation of a higher quality interface between HfO_2 and SiGe.
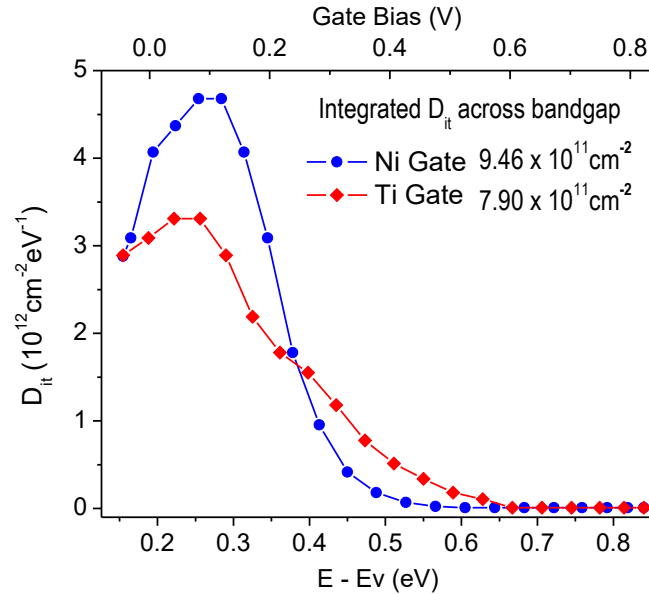
Figure 3.4 Interface defect density distributions for Ni vs Pd/Ti/TiN devices. The D_{it} values extracted from the full interface state model and in good agreement with the D_{it} values from the conductance method.
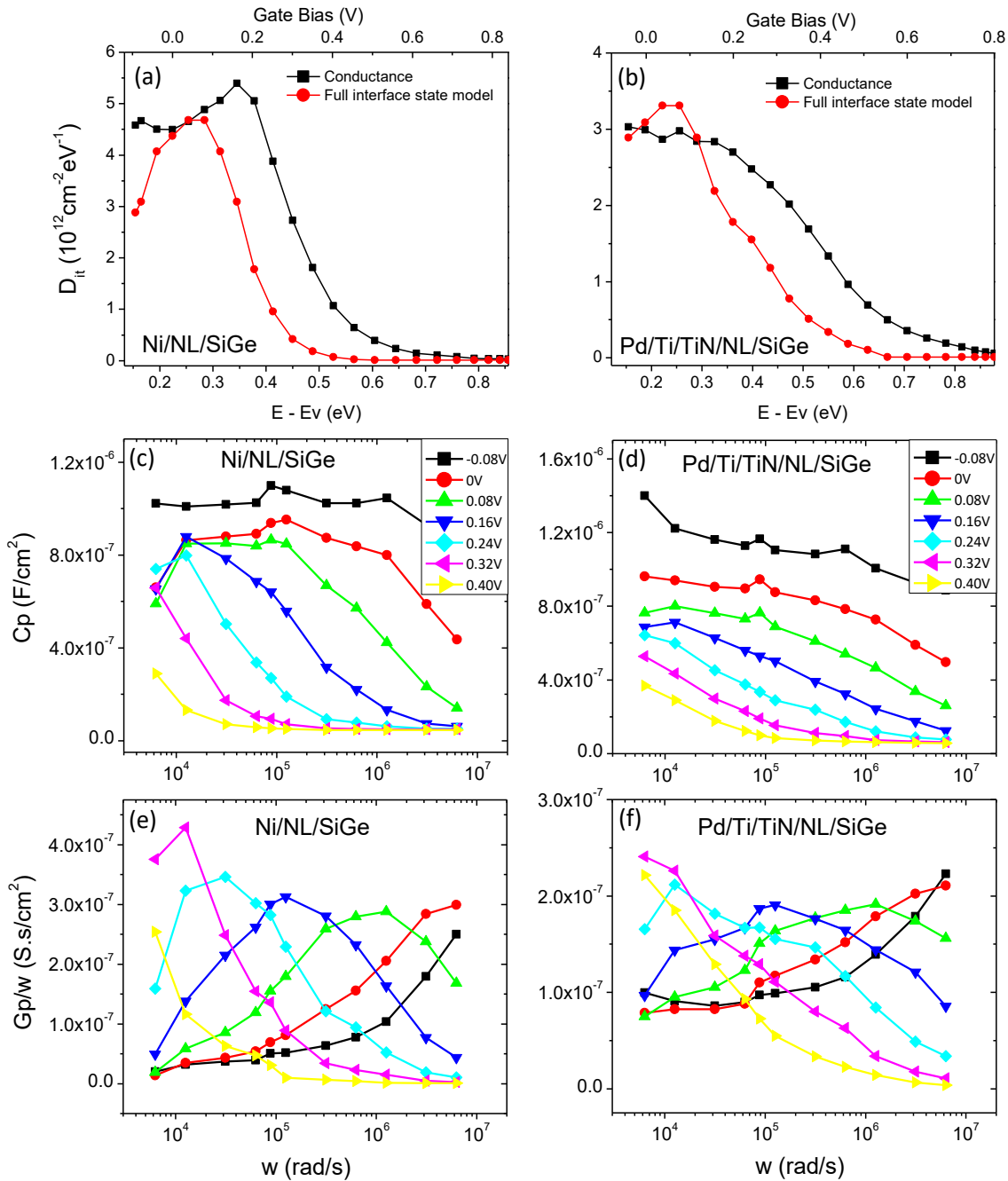
Figure 3.5 Interface defect density analysis of Ni vs Pd/Ti/TiN MOSCAPs (a-b) Comparison of defect distribution obtained with conductance and full interface state model. (c-d) $C_P - \omega$ graph, (e-f) $G_P/\omega - \omega$ graph. The conductance method was used to extract D_{it}. Both models show similar maximum defect density above the valence band with a small shift in energies. This difference can be attributed similar peak values of G_p/ω seen in several bias points shown in figure e-f. Both models indicate lower defect interface formation with Pd/Ti/TiN gated devices in comparison to Ni/NL/SiGe/Si devices.

47

3.4 Structural analysis of MOSCAPs with Gettering Metal Gate

This significant increase in capacitance can be attributed to IL thinning with oxygen scavenging by the reactive Ti gates, as shown in STEM images in figure 3.6. The Ni gated sample shows a ~1.1 nm thick IL whereas the sample with the Ti gate has 0.7 nm thick IL as shown in figure 3.7. However, the expected C_{max} value according to the STEM-derived oxide thicknesses is $2.8\mu F/cm^2$ instead of $3.5\mu F/cm^2$ for the Pd/Ti/TiN gated MOSCAP as shown in calculation in section 3.41 - 3.43.
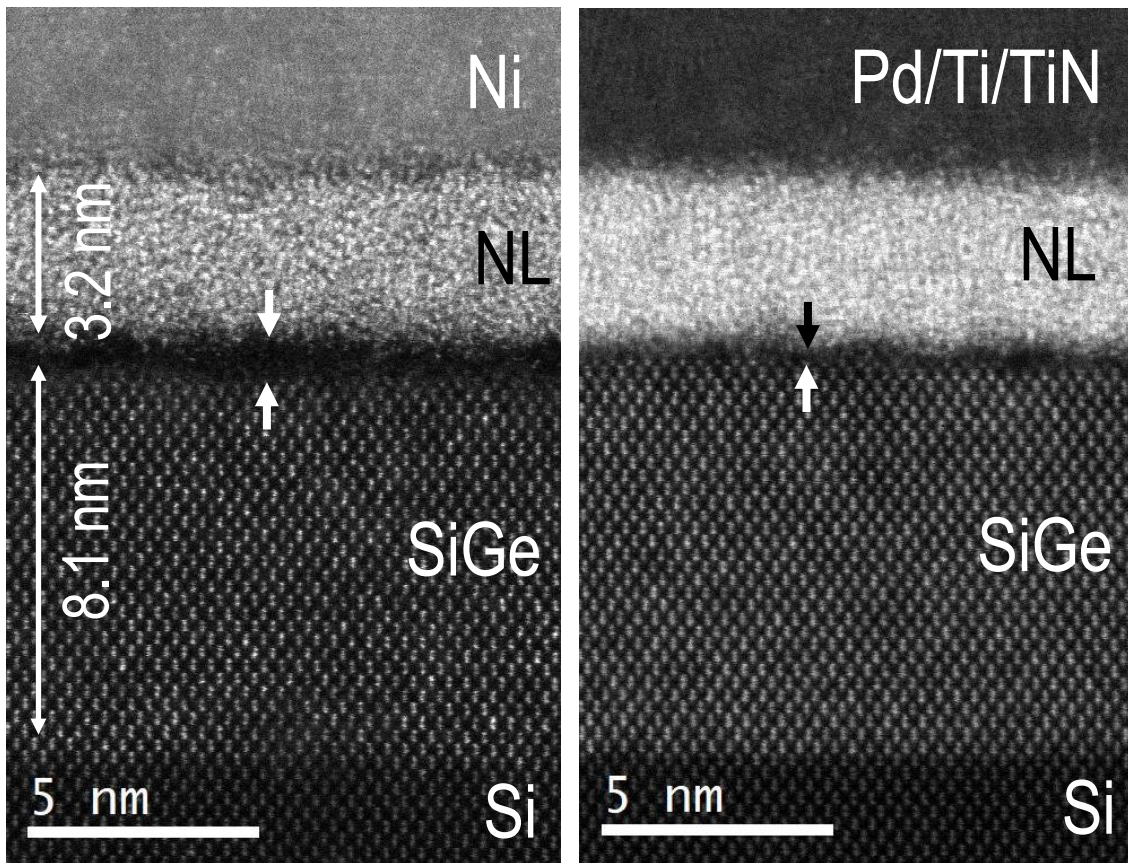
Figure 3.6 STEM-HAADF images of Ni/NL/SiGe/Si and Pd/Ti/TiN/NL/SiGe/Si. STEM-HAADF images of Ni and Pd/Ti/TiN gated HfO_2-Al_2O_3 nanolaminate MOSCAPs.

In this calculation, it is assumed that both devices have oxides with the same dielectric constant because they were grown simultaneously in the ALD reactor. Second, it is assumed that the dielectric constant of the IL formed at SiGe/HfO_2 is k = 4.5 as the IL consists of both SiO_2 (k = 3.9) and GeO_2 (k = 5.2)[69]. Therefore, the C_{max} difference between the experimental and expected value for the Pd/Ti/TiN sample suggests permittivity modulation of the HfO_2. In conjunction with this, the equivalent oxide thickness (EOT) for Ni-gated samples was found to be ~1.5 nm whereas Ti gettering gate has a notably lower EOT of ~1 nm as seen in following analysis.

Previously, the dielectric constant variation in HfO_2 by several means was reported. For example, nitrated HfO_2 was found to a have higher dielectric constant than pure HfO_2.[60] Considering TiN deposition on HfO_2 by sputtering in these samples, similar impact of permittivity modulation can be expected because sputtered TiN can form HfN via exchange of oxygen between HfO_2 and TiN. In addition, this exchange will form high-k TiO_2 (k=80) which will increase the net capacitance. Furthermore, it is likely that sputtered Ti can readily penetrate HfO_2 through TiN and form TiO_2 in the HfO_2.[59] Overall, the capacitance enhancement is dominated by IL thinning by oxygen scavenging. For given oxide thicknesses and C_{max}, the effective dielectric constant of the gate oxide was found to be k =10.93 for Ni and k = 16.2 for Pd/Ti/TiN gated MOSCAPs.
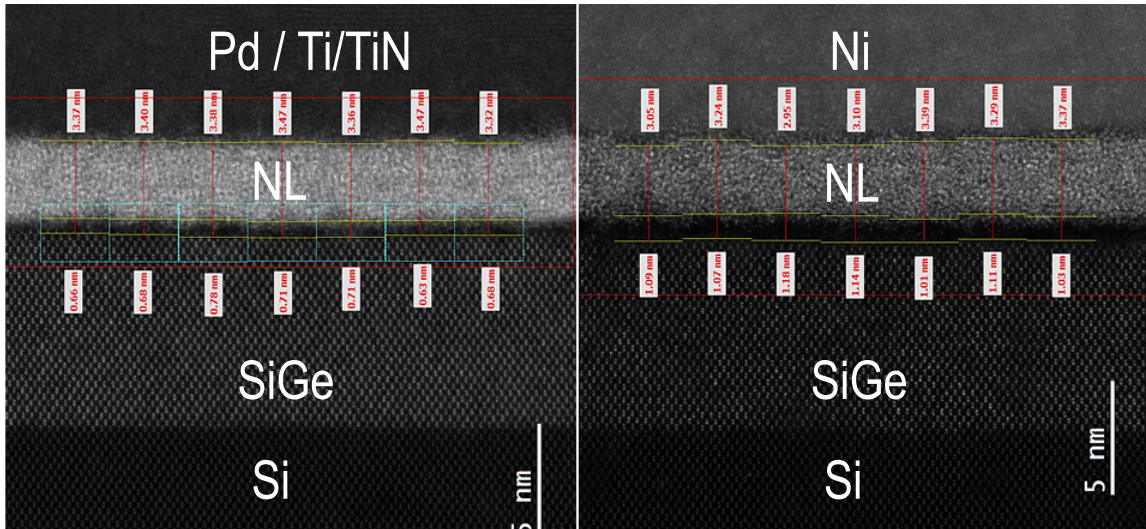
Gate	Avg. high-k	Avg. IL	Avg. HK + IL
TiN/Ti/Pd	34.0Å	6.9Å	40.9Å
Ni	32.0Å	10.9Å	42.9Å

Figure 3.7 Interface oxide thickness analysis with STEM-HAADF. Images shows comparable thickness for nanolaminate gate oxide in both devices. A ~4Å thinner interfacial oxide was observed in the Pd/Ti/TiN gated device (0.69nm) compared to the Ni gated device (0.11nm). The table for average thickness of ILs and HfO_2-Al_2O_3 gate oxide thickness is shown. Ti-gated device shows thinner IL in comparison with the Ni control.

3.4.1 Effective Dielectric Constant Analysis for Control Ni Gate

$$C_{accumulation} = C_{oxide} = \frac{K_o \varepsilon_o A}{t_{oxide}} \qquad \varepsilon_o = 8.85 \times 10^{-12} F/m$$

$$IL \Rightarrow \quad K_o = 3.9 \ (SiO_2), \quad K_o = 5.2 \ (GeO_2) \Rightarrow K_{IL} = 4.5$$

$$K_o = 25 \ (HfO_2), \quad K_o = 9 \ (Al_2O_3)$$

$$Area \ (A) = 16 \times 10^{-9} m^2$$

$$t_{oxide} = \sim 3.2 \times 10^{-9} m, \ t_{IL} = \sim 1.1 \times 10^{-9} m \quad (STEM)$$

$$C_{HfO_2} = \frac{25 * 8.85 \times 10^{-12} * 16 \times 10^{-9} m^2}{2.88 \times 10^{-9} m} = 1229 pF$$

$$C_{Al_2O_3} = \frac{9 * 8.85 \times 10^{-12} * 16 \times 10^{-9} m^2}{0.32 \times 10^{-9} m} = 3982 pF$$

$$C_{IL} = \frac{4.5 \times 8.85 \ x \ 10^{-12} \times 16 \times 10^{-9} m^2}{1.1 \times 10^{-9} m} = 579 pF$$

$$\frac{1}{C_{ox}} = \frac{1}{C_{IL}} + \frac{1}{C_{(Al_2O_3)}} + \frac{1}{C_{(HfO_2)}} \Rightarrow \frac{1}{1229 pF} + \frac{1}{3982 pF} + \frac{1}{579 \ pF}$$

$$C_{ox} = 358.17 pF \Rightarrow \frac{C_{ox}}{A} = \frac{358.17 \times 10^{-12} F}{16 \times 10^{-5} cm^2} = 2.23 \ \mu F/cm^2$$

Ni/NL/SiGe/Si device IL oxide thickness estimated from STEM and found to be 1.1nm. Since the interface oxide layer constitute of both SiO_2 and GeO_2, the interface oxide dielectric constant is assumed to be ~4.5 which is the average of the dielectric constants of SiO_2 and GeO_2.

3.4.2 Effective Dielectric Constant Analysis for Control Remote Gettering Gate

$$C_{accumulation} = C_{oxide} = \frac{K_o \varepsilon_o A}{t_{oxide}} \qquad \varepsilon_o = 8.85 \times 10^{-12} F/m$$

$$IL \implies K_o = 3.9 \ (SiO_2), \ K_o = 5.2 \ (GeO_2) \implies K_{IL} = 4.5$$

$$K_o = 25 \ (HfO_2), \ K_o = 9 \ (Al_2O_3)$$

$$Area \ (A) = 21.7 \times 10^{-9} m^2$$

$$t_{oxide} = \sim 3.4 \times 10^{-9} m, \ t_{IL} = \sim 0.7 \times 10^{-9} m \quad (STEM)$$

$$C_{HfO_2} = \frac{25 * 8.85 \times 10^{-12} * 21.7 \times 10^{-9} m^2}{3.06 \times 10^{-9} m} = 1569 pF$$

$$C_{Al_2O_3} = \frac{9 * 8.85 \times 10^{-12} * 21.7 \times 10^{-9} m^2}{0.34 \times 10^{-9} m} = 5083 pF$$

$$C_{IL} = \frac{4.5 \times 8.85 \ x \ 10^{-12} \times 21.7 \times 10^{-9} m^2}{0.7 \times 10^{-9} m} = 1234 pF$$

$$\frac{1}{C_{ox}} = \frac{1}{C_{IL}} + \frac{1}{C_{(Al_2O_3)}} + \frac{1}{C_{(HfO_2)}} \implies \frac{1}{1234 pF} + \frac{1}{5083 pF} + \frac{1}{1569 \ pF}$$

$$C_{ox} = 608 \ pF \implies \frac{C_{ox}}{A} = \frac{608 \times 10^{-12} F}{21.7 \times 10^{-5} cm^2} = 2.8 \ \mu F/cm^2$$

Pd/Ti/TiN/NL/SiGe/Si device IL oxide thickness estimated from STEM and found to be 0.7 nm. Similarly, IL constitute of both SiO_2 and GeO_2, therefore dielectric constant is assumed to be ~4.5. The Al_2O_3 and HfO_2 thicknesses are estimated from the number of ALD cycles of each oxide assuming equal growth rates per cycle and the total oxide thickness as determined by STEM.

3.4.3 Equivalent Oxide Thickness (EOT)

Equivalent oxide thickness is the thickness of SiO_2 gate oxide that is needed to induce same capacitance effect as high-k dielectric oxide being used in MOS.

$$C_{acc} = C_{ox} = \frac{k_o \varepsilon_o A}{t_{ox}}$$

$$k_{ox} = \frac{t_{ox} \, C_{acc}}{\varepsilon_o \, A}$$

$$EOT = \frac{k_{SiO_2} \, t_{ox}}{k_{ox}} = \frac{k_{SiO_2} \varepsilon_o \, A}{C_{acc}} = \frac{3.9 \times 8.85 \times 10^{-12} \, F/m}{C_{density} \, \mu F/cm^2}$$

$$EOT_{Ni \, gate} = \frac{3.9 \times 8.85 \times 10^{-12} \, F/m}{2.25 \, \mu F/cm^2} = 1.53nm$$

$$EOT_{TiN} = \frac{3.9 \, * \, 8.85 \times 10^{-12} \, F/m}{3.5 \, \mu F/cm^2} = 0.98nm$$

In comparison the Ni gate with 1.53nm EOT, Pd/Ti/TiN gate has an EOT below 1 nm which indicates a ~50% increase in overall effective dielectric constant of the gate oxide as shown below.

$$k_{Ni} = \frac{4.29 \, nm \times 2.25 \, \mu F/cm^2}{8.85 \times 10^{-12} F/m} = 10.9$$

$$k_{TiN} = \frac{4.09nm \times 3.5 \, \mu F/cm^2}{8.85 \times 10^{-12} F/m} = 16.17$$

3.5 Compositional Analysis MOSCAPs with Remote Gettering Gate

EELS analysis for the Ni/HfO$_2$-Al$_2$O$_3$-NL and Pd/Ti/TiN/HfO$_2$-Al$_2$O$_3$-NL samples shown in figure 3.8. In comparison to the Ni/HfO$_2$-Al$_2$O$_3$-NL sample, the Pd/Ti/TiN/HfO$_2$-Al$_2$O$_3$-NL sample has an abrupt Si profile in the IL region. This may be result of local variability of the interfaces. Another reason would be expected excess of oxygen in the HfO$_2$-Al$_2$O$_3$-NL for Ni/HfO$_2$-Al$_2$O$_3$-NL devices than for Pd/Ti/TiN/HfO$_2$-Al$_2$O$_3$-NL devices; it is hypothesized that the excess oxygen enhances Si diffusion into the HfO$_2$. The most important difference between these samples is the IL; a thinner IL is observed for Pd/Ti/TiN than for for Ni gates. Furthermore, EELS analysis indicates slightly lower Ge/Si ratio in the ILs for Pd/Ti/TiN (0.32) vs Ni-gated (0.38) devices as indicated with green arrows. This difference correlates with the lower defect density obtained in C-V analysis and indicates successful GeO$_x$ defect reduction with Ti gettering gates via remote oxygen scavenging through the TiN layer.

The formation of a SiO$_x$ rich interfaces with Ti gettering gates is consistent with the more favorable thermodynamics of Ge-O to Ti ligand exchange than Si-O to Ti-O ligand exchange. The excess interlayer Ge in Pd/Ti/TiN gated device might have been evaporated in form of GeO$_x$ or it may have regrown on SiGe epitaxially; however, the amount of Ge being regrown would be difficult to detect by TEM-EELS since the interlayers are below 1nm thickness. GeO$_x$ diffusion through gate oxides has been detected by XPS[13], but again the amount would be too small to detect by TEM-EELS. It is noted that in comparison to the Al gettering gate in figure 2.3, the Pd/Ti/TiN gettering gate in figure 3.3 is less effective for interface defect reduction.
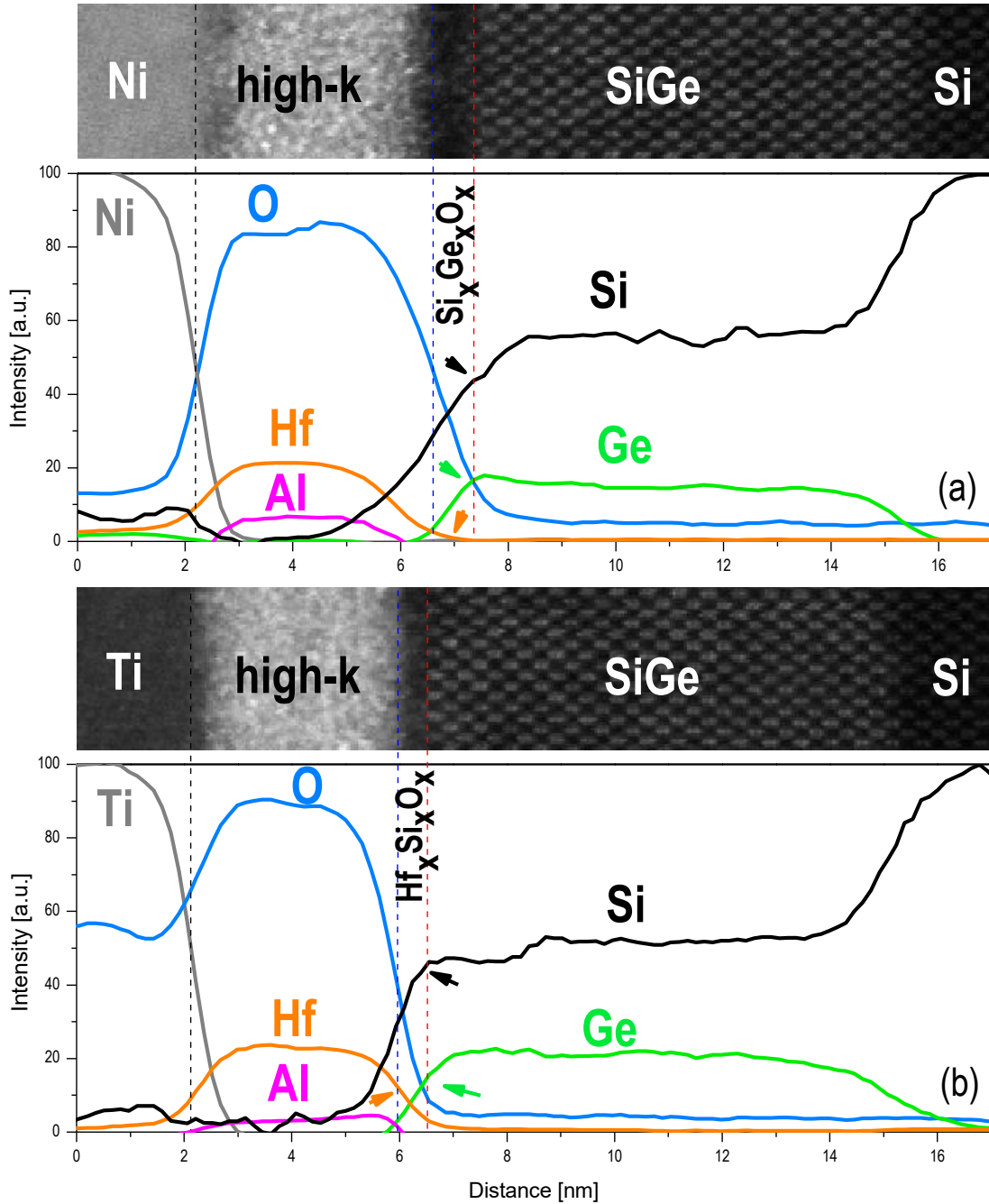
Figure 3.8 STEM-HAADF and EELS analysis of Ni (a) and Pd/Ti/TiN (b) gated devices. The blue line intercepts the half max of the oxygen signal. The red line marks the SiGe surface atoms determined from the last row of crystallographically ordered atoms in the corresponding STEM image. Black and green arrows point to the Si and Ge composition at the SiGe surface. The orange arrow indicates the Hf compositions in the ILs. Ti-gated devices have a thinner Si rich IL of ~6Å in comparison with ~9Å for the control Ni-gated devices.

It is hypothesized that this difference has multiple causes. First TiN is known to be good diffusion barrier for oxygen and this likely reduces the efficiency of the scavenging process. Second, the Ni gate is grown with thermal evaporation (a soft process); conversely, the Pd/Ti/TiN gate is grown by sputter deposition which has energetic atoms and ions that can damages the oxide and the semiconductor interface. This sputter deposition induces additional defects at the interface for Pd/Ti/TiN gate which results higher D_{it} before FGA which is partially recovered during FGA, but the damage recovery is not complete. Third, the FGA annealing was optimized for Ni gated nanolaminate structure; therefore, the further FGA optimization might be required for each device structure to improve the effectiveness of the scavenging process.

3.6 Conclusion

Oxygen reactive Al and Pd/Ti/TiN gates were employed to reduce interface defects by scavenging oxygen from the $SiGe/HfO_2$ interface. In comparison with control Ni-gated device, thinner IL formation in Pd/Ti/TiN gated MOSCAP was demonstrated using STEM. Lower interface defect formation with Pd/Ti/TiN gettering gate coincided with Si-rich interlayer formation as shown by STEM-EELS-EDS analysis. These results suggest that Pd/Ti/TiN gate scavenge oxygen from the IL forming a thinner interlayer which contains less GeO_x. By having less GeO_x at the interface, this process reduces interface defects. As shown in previous chapter, while Al-gated devices exhibited a C_{max} reduction due to formation of Al_2O_3 in contact with HfO_2, the Pd/Ti/TiN gated device exhibited a C_{max} enhancement as the oxidized metal layer (TiO_X) was separated from HfO_2 by a conductive diffusion barrier.

3.7 Acknowledgment

Chapter IV

Engineering high-k/SiGe interface with novel gate oxide structures

4.1 Introduction:

Previously, partial elimination of interface defects via suppression of GeO_x formation with several surface treatments such as nitride and sulfur passivation on $Si_{0.7}Ge_{0.3}(001)$ prior to Al_2O_3 gate oxide deposition was reported [13,15]. However, such surface treatments are not capable of preserving SiGe surface therefore similar low defect density interfaces could not be established with HfO_2 gate oxide. This is because oxygen containing species such as excess H_2O, OH, and/or O can diffuse through HfO_2 during atomic layer deposition (ALD), forming GeO_x defects on the SiGe surface; in addition, the nature of HfO_2 allows diffusion of Ge and GeO_x to the top surface of the oxide as a result of reaction with HfO_2 and GeO_2 decomposition[14,15,63,70]

Recently, HfO_2/SiGe interfaces formed with Al_2O_3-HfO_2 nanolaminate gate dielectric stacks were found have a low interface state density, and it was hypothesized that the mechanism was reduction of GeO_x out-diffusion during ALD[71]. On the other hand, as presented in second chapter, theoretical DFT models of the amorphous HfO_2/$Si_{0.5}Ge_{0.5}(001)$ interface have shown that low-defect interfaces may be formed even before hydrogen passivation with short anneals (<10 ps) when the interface is comprised solely of SiO (silicon monoxide)[8].

Consecutively, formation of ultra-low defects at sub 0.5nm HfO_2/SiGe interface via selective oxygen scavenging by using an oxygen-scavenging, metallic Al gate[72] presented. The selectivity is shown to be result of difference in formation enthalpy of GeO_x compare to SiO_x facilitating transfer of oxygen from GeO_x to Al.[6,72] As shown, this process induces thicker gate oxides and reduced capacitance density (C_{max}) resulting from Al oxidation on top of ALD grown gate oxide. In chapter three, remote oxygen gettering through thin Ni gate metal and TiN diffusion barrier shown to prevent decrease in capacitance. However, these gettering gates need to be replaced with desired low work function metal to adjust the threshold voltage at MOSFET. The replacement processes of gettering gates increase fabrication steps and the cost along with other manufacturing concerns.

In the present study, formation of low interface defect density HfO_2/SiGe gate stacks using inorganic and organometallic based ALD Al_2O_3 insertion in bilayers and nanolaminates of Al_2O_3 and HfO_2 was investigated with STEM-EELS analysis. It is found that insertion of the highly oxygen reactive trimethyl aluminum (TMA) ALD precursor for Al_2O_3 in HfO_2 containing gate stacks reduces defects consistent with remote selective oxygen scavenging from the interface. This new selective oxygen scavenging technique is most effective when Al_2O_3 layers are uniformly distributed across the HfO_2 in a nanolaminate (NL) structure, but it also is effective when the Al_2O_3 ALD deposition occurs on top of the HfO_2. In Al_2O_3 ALD, during each TMA half cycle, the TMA is dosed in excess; therefore, after the surface hydroxyl groups are eliminated, the TMA is available to reduce additional species either by diffusion through HfO_2 or remotely at the growth surface. This is consistent with GeO_x out diffusing to the top of HfO_2 gate oxides[15,63,73], and the TMA remotely reducing the GeO_x during each half cycles[63].

It is found that using the Al_2O_3 ALD prior to HfO_2 deposition is not as effective as using the Al_2O_3 ALD in the nanolaminate, consistent with the suggestion that gettering is most effective after deposition of sufficient oxide to act as an H_2O barrier to reduce additional formation of GeO_x during water-based ALD. This hypothesis of the gate oxide acting as a H_2O barrier and TMA being a GeO_x reducing agent was supported by experiments with ALD of purely Al_2O_3 gates, because Al_2O_3 is a better diffusion barrier than HfO_2[63]. Once the Al_2O_3 gate oxide reaches a critical thickness, an additional 25% increase in oxide thickness results in a $4\times$ reduction in D_{it} and nearly complete elimination of the $SiGeO_x$ interfacial layer. For HfO_2, the selective scavenging process benefits from the difference in formation enthalpy of SiO_x in comparison to GeO_x and reduces the interface trapped charge density by forming Si-rich SiO_x at the interface, consistent with the predictions of the DFT models[8]. This is also consistent with the known ability of TMA to reduce low enthalpy of formation oxides on substrates at the start of ALD, a process known as ALD cleanup[74,75].

4.2 Fabrication of novel hetero oxide MOSCAPs

MOSCAP devices were fabricated with HfO_2 and Al_2O_3 oxides onto $Si_{0.7}Ge_{0.3}(100)$ epitaxially grown on p-type Si (100). Similar to fabrication process explained earlier, after degreasing samples, native oxides were removed by cycling 2.5 times through 1 min 2% HF solution and 1 min DI H_2O, ending with 2% HF. The samples were dried in N_2, passivated in an ammonium sulfide solution (25% $(NH_4)_2S$) for 15 minutes, rinsed with water for 30 seconds, and dried with N_2. Subsequently, samples were transferred to the atomic layer deposition (ALD) chamber and oxide structures were grown by using a Beneq TFS200 cross flow reactor at 275C using tetrakis dimethyl amino hafnium (TDMAH), $HfCl_4$ and TMA metal precursors and water as an oxidant. Each HfO_2 cycle consisted of 1s of a TDMAH or $HfCl_4$ pulse and a 500ms of H_2O pulse, each Al_2O_3 cycle consisted of a 1s TMA pulse and a 500ms H_2O pulse. Ar was used as carrier gas for all processes, and 6s purges were employed between each pulse.

A set of samples were fabricated in bilayer, tri-layer and nanolaminate (NL) structures formed by Al_2O_3 and HfO_2 in gate stack for MOSCAPs as shown in figure S1 and the insets of figure 1. Nickel gates (50nm thick, 150um diameter) were deposited with a shadow mask onto the oxide surface using a Denton 502A thermal evaporator in vacuum < 2×10-6. Al back contacts were deposited by sputtering after native oxide removal with Ar plasma at 100W, 5mTorr in Denton Discovery 635 sputtering system. Samples were annealed using an optimized recipe for 30 minutes total (10 min at 300°C, 10 min at 330°C, and 10 min at 350°C) in forming gas (5% H2, 95%N2) in forming gas (5% H_2, 95%N_2) in a Ulvac MILA-3000 Minilamp annealer at 3 slpm at 1atm.

4.3 Electrical analysis of MOSCAPs

Electrical characterization of the MOSCAP devices with C-V and G-V measurement obtained from 2 kHz to 1MHz with 30mV AC signal superimposed on DC gate bias varied from 2V to -2V. Impedance analysis of various gate oxide structures after forming gas annealing (FGA) are shown in figure 4.1. The C-V analysis for 45 cycles (~4.5nm) of HfO_2 control sample with a C_{max} of 2.5 uF/cm^2 and corresponding G-V characterization are presented in figure 4.1a and 4.1f; a peak defect density of (D_{it}) 3.74×10^{12} eV^{-1}cm^{-2} (see figure 4.6) is calculated using the full interface state model[68].
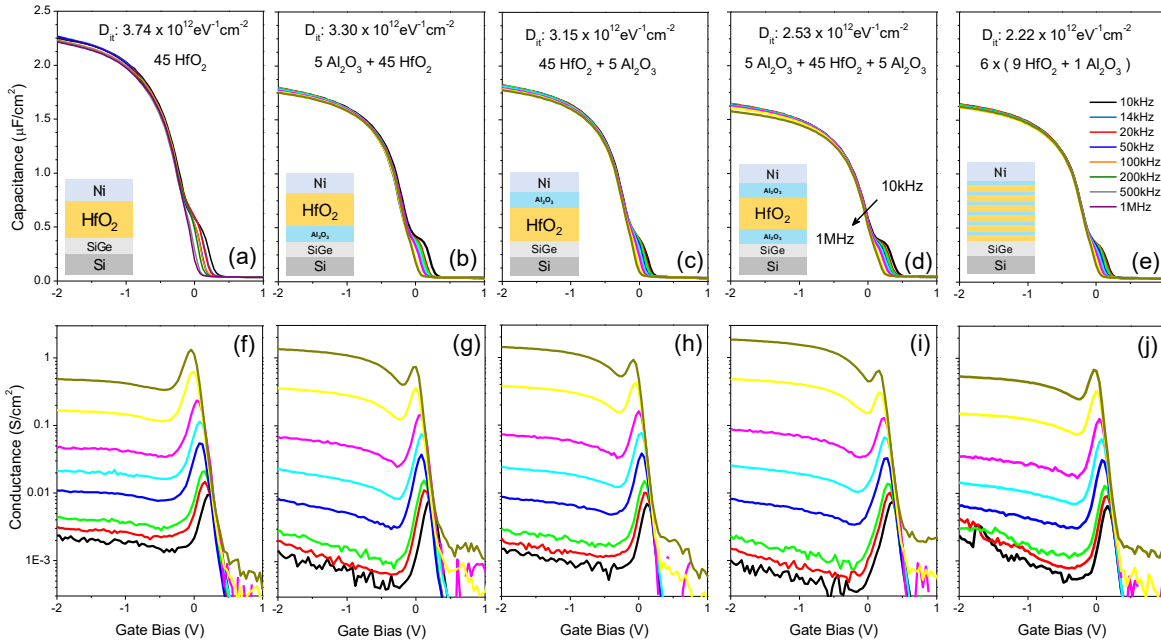
Figure 4.1 C-V and G-V graphs of multilayer MOSCAP devices. Inset drawings indicate device structure for given graph. The inset D_{it} values indicates peak interface defect density value in bandgap obtained with full interface state model. Control device with HfO_2 gate oxide shows highest interface defect density of 3.74×10^{12}eV^{-1}cm^{-2}. Al_2O_3 insertion into HfO_2 reduces D_{it} gradually by going from HfO_2-Al_2O_3 bilayer into Al_2O_3-HfO_2-Al_2O_3 tri-layer and finally nanolaminate gate oxides to D_{it}= 2.22×10^{12} eV^{-1}cm^{-2}. Al_2O_3 insertion reduces D_{it} regardless of its position shows significant impact of oxygen scavenging.
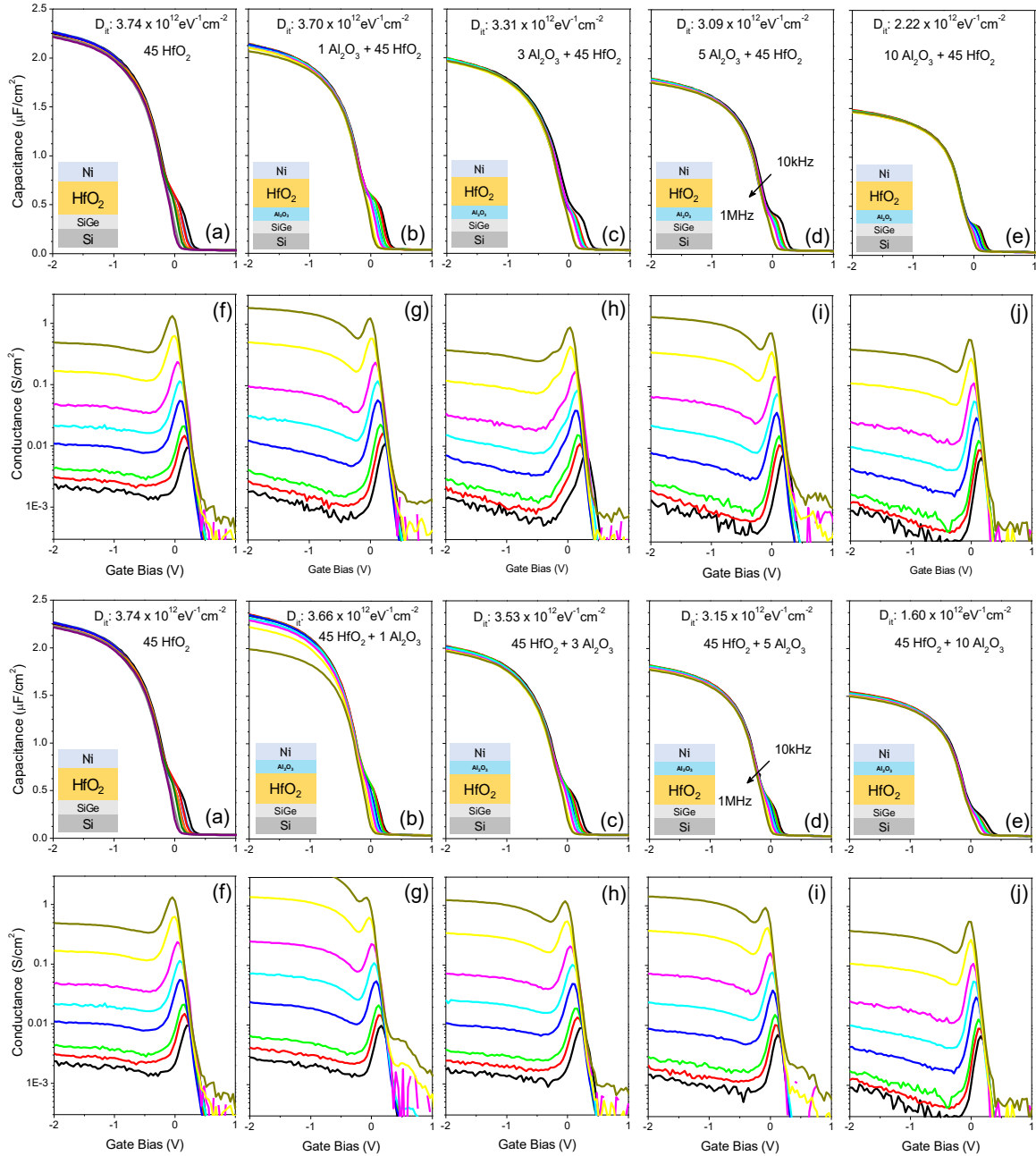
Figure 4.2 (first and second row) and 4.3 (third and fourth row) C-V and G-V graphs of bilayer MOSCAPs with 1,3,5, 10 layers Al₂O₃. Multifrequency (10 kHz to 1 MHz) after FGA C-V graphs of MOSCAP devices with only HfO_2 (a) and bilayers of SiGe/ Al_2O_3 / HfO_2 (b-e). Inset drawing indicates device structures and D_{it} values obtained with full interface state model and shows peak value in band gap. Depletion capacitance decreases from left to right by insertion of Al_2O_3 layers between HfO_2 and SiGe between HfO_2 and Ni varying from 1 to 10 cycles. The frequency dispersion in accumulation at - 2V is result of series resistance for this device.

Figure 4.1b and 1c show the C-V for 5 cycle Al_2O_3 insertion below and above 45 cycles of HfO_2. As expected, Al_2O_3 insertion decreases C_{max} in both cases due to an increase in total oxide thickness and the lower dielectric constant of Al_2O_3 in comparison to HfO_2. However, the magnitude of the dispersive, depletion capacitance D_{it} feature also decreases as shown in Figure 4.1b and 1c. Al_2O_3 insertion below or above HfO_2 has a nearly identical effect on interface defect density corresponding to peak D_{it} values of 3.30×10^{12} $eV^{-1}cm^{-2}$ and 3.15×10^{12} $eV^{-1}cm^{-2}$. Note full D_{it} distributions as a function of the thickness are shown below confirming the trends. Because interface trap response involves defects at the semiconductor oxide interface, a change in D_{it} resulting from the addition of 5 ALD cycles of Al_2O_3 on top of a 4.5 nm thick HfO_2 layer is unexpected. Moreover, as shown in Figure 4.1 d, Al_2O_3 insertion both above and below HfO_2 in an Al_2O_3 /HfO_2/Al_2O_3 tri-layer structure further decreases the interface trapped charge density by 10% to 2.53×10^{12} $eV^{-1}cm^{-2}$. Furthermore, as shown in Figure 4.1e, when Al_2O_3 layers dispersed across the HfO_2 in the nanolaminate structure (NL), the D_{it} decreases further down to 2.22×10^{12} $eV^{-1}cm^{-2}$, 12% lower than the tri-layer with a small increase in C_{max}. The C_{max} reduction due to an increase in total oxide thickness is expected, but D_{it} reduction with more Al_2O_3 incorporation remote from the interface is not. To better document the effects of bottom vs top Al_2O_3, samples were growth with 1, 3, 5, 10 cycles of Al_2O_3 inserted either below the HfO_2 or above the HfO_2 as shown in figure 4.2 and 4.3. Similar trend the decrease in D_{it} with insertion of Al_2O_3 monolayer is seen. D_{it} decreases the most with 10 cycles of Al_2O_3, on top of the HfO_2 induced a 57% decrease in the peak D_{it} as well as a 54% decrease in the integrated D_{it} while the Al_2O_3 inserted below the HfO_2 only induced a 40% decrease in the peak D_{it} as well as a 40% decrease in the integrated D_{it} as shown in figure 4.6.

For the 5 cycle Al_2O_3 insertion, although absolute defect density quantification is challenging, small decreases in the magnitude of the interface trap-related depletion capacitance feature while maintaining an essentially constant C_{max} suggests a lower defect density at the interface oxide/semiconductor interface for the nanolaminate structure compared to tri-layer sample or the bilayer samples. For each processing condition, 5-10 devices were studied. The 2-3 devices with the most consistent C-V were chosen for further analysis. Therefore, although absolute D_{it} calculations are accurate only within 30%; even 10% changes in D_{it} decay with Al_2O_3 insertion are reliable as confirmed via fabrication multiple sample sets. The D_{it} standard errors of the mean (in $/cm^2$-eV and %) for samples were calculated; SiGe/45 cycles of HfO_2/Ni: 0.266 (7.1%) ; SiGe/5 Al_2O_3/45 HfO_2/Ni: 0.074 (2.2%) ; SiGe/ 45 HfO_2/ 5 Al_2O_3/Ni: 0.10 (3.1%); SiGe/5 Al_2O_3/ 45 HfO_2/ 5 Al_2O_3/Ni: 0.124 (4.9%) ; SiGe/ $6 \times (9\ HfO_2 + 1\ Al_2O_3)$ / Ni: 0.05 (2.2%). Therefore, the typical standard error is 3.9%, and changes in D_{it} of 10% are significant in this comparison.
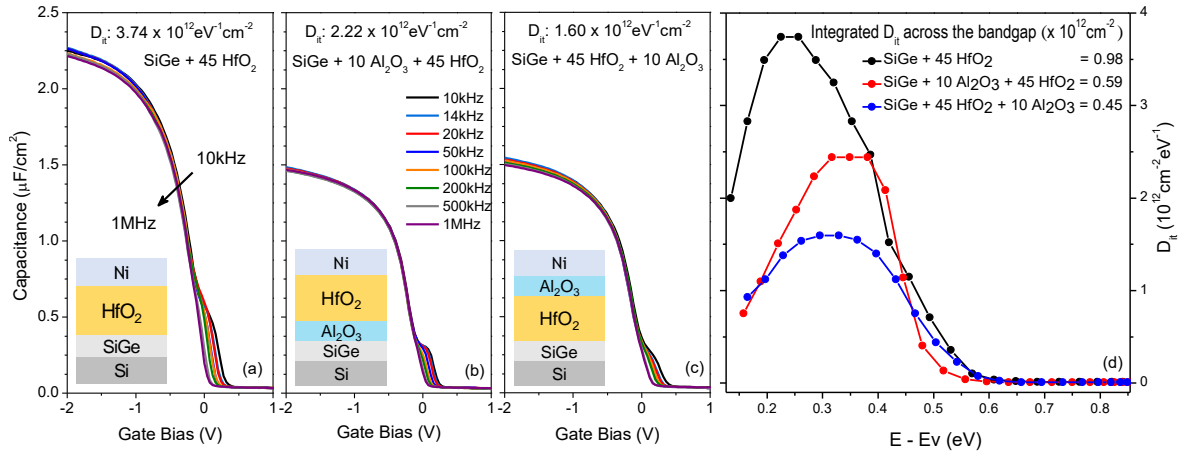
Figure 4.4 C-V graphs and Interface defect density distributions across the band gap for MOSCAPs. Inset drawings indicate device structure and D_{it} values indicate peak interface defect density in bandgap extracted with full interface state model (a) Control device shows highest D_{it} (peak) = 3.74 $x10^{12}eV^{-1}cm^{-2}$ and decreases by insertion of 10 cycles of Al_2O_3 monolayers before HfO_2 D_{it} (peak) = 2.22 $x10^{12}eV^{-1}cm^{-2}$ (b) and after HfO_2 ALD D_{it}(peak) = 1.6 $x10^{12}eV^{-1}cm^{-2}$ (c). Comparison of D_{it} distribution across the band gap shows decrease in peak and integrated D_{it} (inset) by insertion of Al_2O_3 (d).

To investigate the D_{it} reduction mechanism due to insertion of Al_2O_3 ALD layers, MOSCAPs with only Al_2O_3 gate oxides of varying thickness were prepared in below (4.5).
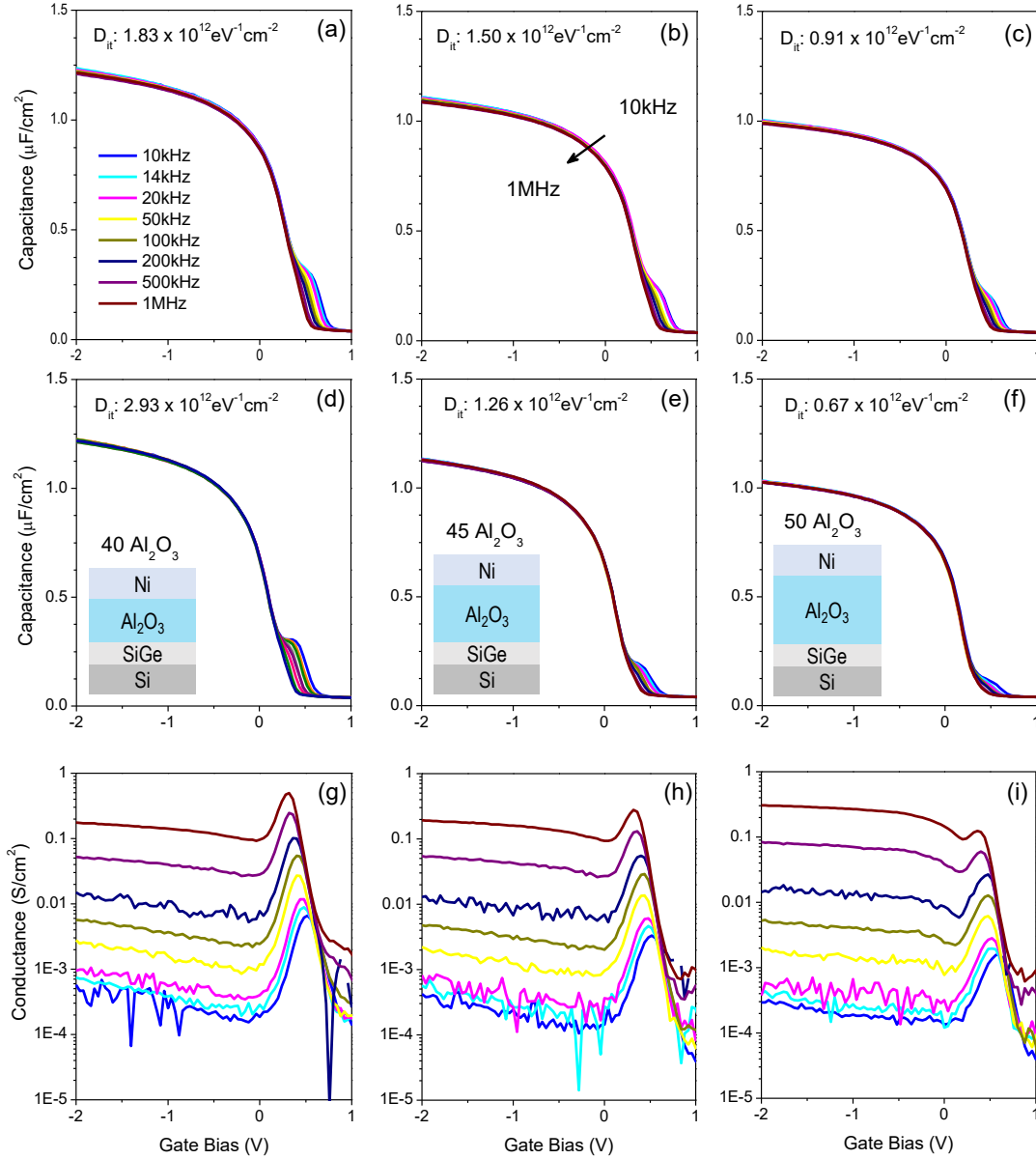
Figure 4.5 C-V and G-V graphs of Al_2O_3 MOSCAPs. Inset drawings illustrate device structure. The inset D_{it} values indicates peak interface defect density value in bandgap. Before FGA is shown in a-c and after FGA results shown in d-i. Control device with 40 cycles of Al_2O_3 gate oxide shows highest interface defect density and it decreases from left to right by increasing the thickness of Al_2O_3 layers on SiGe varying from 40 to 50 cycles. The small increase of Al_2O_3 thickness reduces D_{it} by > 4×; the lowest interface defect density of 0.67×10^{12} $eV^{-1}cm^{-2}$ is obtained with 50 cycles of Al_2O_3 after FGA.

As expected, C-V and G-V measurements from Al_2O_3 devices before and after FGA as a function of deposition cycles or oxide thickness show a decrease in C_{max} from 1.3uF/cm^2 to 1.0 uF/cm^2 by increasing the oxide thickness. The depletion capacitance D_{it} feature also decreases in amplitude. Once the ALD-grown oxide thickness increases above a critical value, there is a super-linear decrease in D_{it}. For an increase of 25% in the number ALD cycles (40 to 50 cycles), the D_{it} decreases by > 4× from 2.93×10^{12} to 0.67×10^{11} eV^{-1}cm^{-2} after FGA devices. Similar trend is also observed for Al_2O_3 before FGA as shown in figure 4.5 a-c. Because the D_{it} originates from defects at the interface with the semiconductor, D_{it} reduction by growing additional Al_2O_3 layers is consistent with chemical modification of the interface by exposure to the TMA-based ALD environment.

The suppression of the interface defects with Al_2O_3 insertion into gate oxide influences is not limited to a single energy but is distributed across the band gap as shown in the D_{it} energy distributions extracted from measured C-V and conductance-voltage (G-V) data using the full interface state model[68] as shown in figure 4.4. Trapped charge energy distributions of the corresponding capacitors shown in figure. 4.6 a and b are consistent with figure 4.2 and show a decrease of D_{it} with incorporation of Al_2O_3 ALD layers bot below and above HfO_2 layers. Inset D_{it} values in figure 4.6 c and d denote the integrated defect density across the band gap and are in good agreement with the behavior observed for the peak D_{it}.
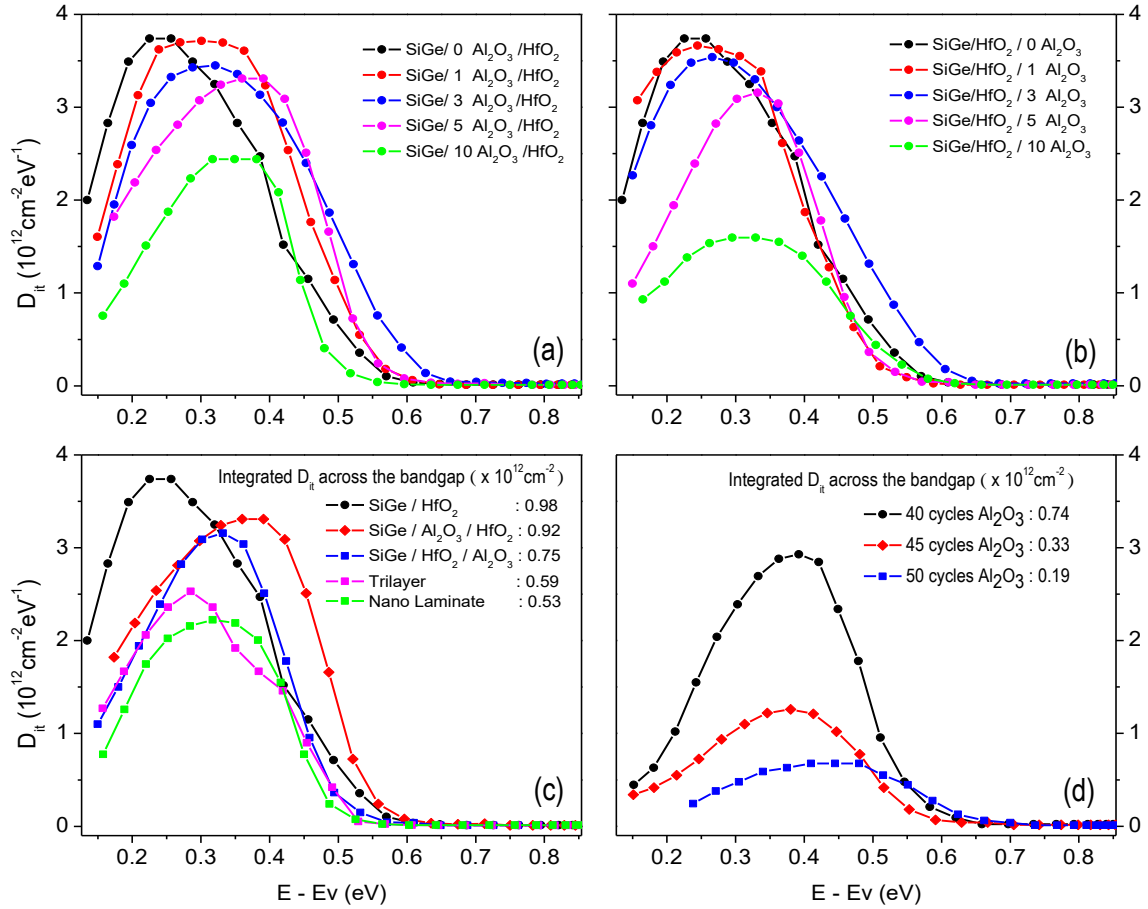
Figure 4.6 Interface defect density distributions of MOSCAP devices. The distribution of interface defects across the band gap calculated with the full interface state model. Interface defects at SiGe- oxide interface decrease by insertion of Al_2O_3 layers before HfO_2 (a) and after HfO_2 (b) gate oxide. (c) Comparison of interface defects variation at SiGe- oxide interface by insertion of Al_2O_3 layers into HfO_2 gate oxide. (d) Interface defect density decreases by increase in Al_2O_3 thickness. For 50 cycles of Al_2O_3, peak D_{it} reduces to 6×10^{11} $eV^{-1}cm^{-2}$ and integrated defects across the bandgap is as low as 0.19×10^{11} $eV^{-1}cm^{-2}$.

In Al_2O_3 ALD, during each TMA half cycle, the TMA is dosed in excess; therefore, after the surface hydroxyl groups are eliminated, the TMA is available to reduce additional species. However, during each H_2O half cycle, the H_2O is present in excess at the end of the pulse, and some H_2O or H_2O-derived species may diffuse through thin Al_2O_3 gate stack. Also, although Al_2O_3 is better diffusion barrier in comparison to HfO_2, it has been reported previously that GeO_x can diffuse through thin Al_2O_3 gate stacks[13]. The $Al_2O_3 - SiGe$ interface is known to include GeO_x species which are source of interface defects[6]. It is hypothesized that above a critical thickness, the Al_2O_3 becomes a good barrier to H_2O; therefore, excess TMA exposure during ALD can scavenge oxygen from GeO_x species and convert it into Ge which might be redeposited on SiGe without formation of new GeO_x from the water pulses.[6] This mechanism is consistent with decreasing D_{it} by insertion of Al_2O_3 into HfO_2-containing gate dielectric stacks or deposition of Al_2O_3 on top of HfO_2 gate dielectrics. However, as noted earlier, Al_2O_3 is more effective diffusion barrier in comparison to HfO_2 for oxygen containing species; consequently, the D_{it} suppression with HfO_2 dielectrics is not expected to be as great as with Al_2O_3 dielectrics of similar thickness[63]. This suggests that the number of Al_2O_3 layers incorporated into oxide is mainly responsible for the interface defect density reduction observed in these experiments. It is noted that for HfO_2 based gate stacks with incorporated Al_2O_3 layers the TMA may diffuse to the interface to directly reduce the GeO_x to Ge since HfO_2 is a poor diffusion barrier; however, the mechanism likely coexists with the remote scavenging mechanism.

4.4 Structural analysis of MOSCAPs

Figure 4.7 shows STEM high-angle annular dark-field (HAADF), bright field (BF) and TEM images of the HfO_2-only, HfO_2 - Al_2O_3 bilayers and nanolaminate gate stacks. White and black arrows in HAADF and BF images indicate the estimated oxide interfacial layer (IL) thickness. The SiGe-HfO_2 interface in figure 4.7a shows a 0.8 nm IL. Insertion of Al_2O_3 between SiGe and HfO_2 increases the apparent IL thickness (figure 4.7b) which is expected because the interface now consists of both Al_2O_3 and $SiGeO_x$. EELS or another spatially-resolved composition profiling method is needed to differentiate between these layers because of the similar atomic mass contrast of these oxides in HAADF-mode imaging. Al_2O_3 grown on HfO_2 and the Al_2O_3 - HfO_2 nano-laminate have thickness similar that shown in figure 4.7.
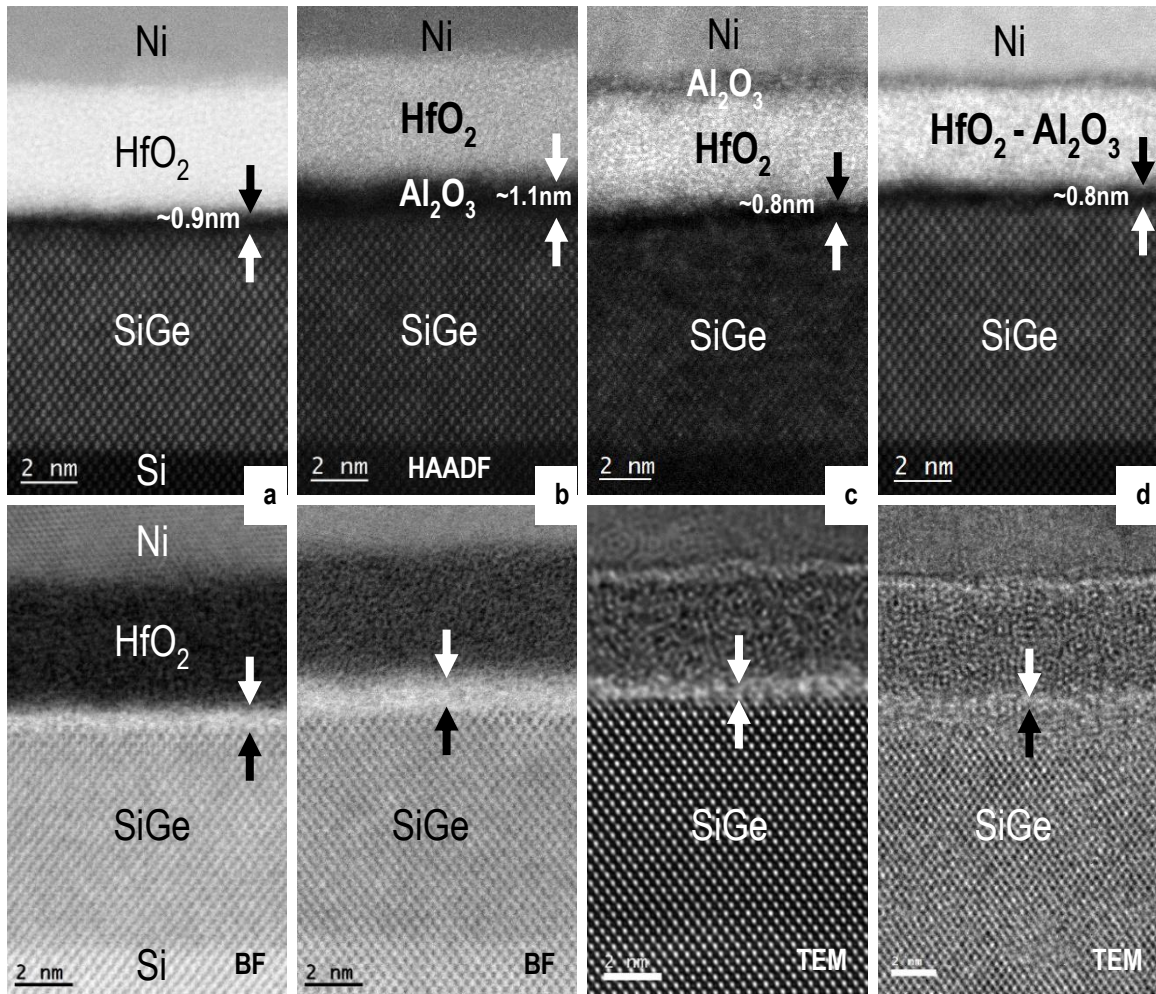
Figure 4.7 STEM-HAADF-BF images of MOSCAP devices. (a) control HfO_2, (b) $HfO_2/Al_2O_3/SiGe$ bilayer, (c) $Al_2O_3/HfO_2/SiGe$ bilayer, (d) and Al_2O_3 – HfO_2 Nanolaminate MOSCAPs. In these images, oxide structures and regions are defined according to z contrast. The interfacial layer between SiGe and oxide indicated with black and white arrows on corresponding STEM – HAADF, STEM - BF and TEM image. Note in (b) the interlayer consists of both $SiGeO_x$ and Al_2O_3, so it appears thicker than the control device in (a). In comparison to control device of $HfO_2/SiGe$, bilayer (c) and NL (d) shows thinner interface consistent with remote Al_2O_3 insertion reducing IL.

4.5 Compositional analysis of MOSCAPs

Elemental profiles across the gate stacks were investigated with STEM-EELS analysis as shown in figure 4.8. A multiple linear least square (MLLS) fitting procedure[76] is used to resolve spectroscopic feature overlay issues, especially for Al, Hf and Si. The red dash line intercepts the half max of oxygen peak and is employed to indicate the SiGe surface. Black and green arrow denote Si and Ge composition of the SiGe surface. figure 4.8a and 6b show 200keV EELS analysis of the same structures fabricated with hafnium tetrachloride at 300C and tetradimethylamido hafnium ALD precursors at 275C; no significant differences were observed as seen in figure 4.8a and b consistent with interface defects obtained with multifrequency C-V analysis. Both the $HfCl_4$ and TDMAH gate stacks have nearly identical elemental distribution across the device and have a Ge tail extending about 2 nm into the HfO_2 layer in contrast to the capacitors in figure 4.8c-f which show a diminished or zero Ge tail. This may be attributed to the Al_2O_3 layer impeding Ge out-diffusion[15,63]. It is surprising that Al_2O_3 reduces Ge out diffusion even when Al_2O_3 is deposited onto HfO_2 (figure 4.8c - 6f).

Further documentation that even remote Al_2O_3 ALD can control the GeO_x in the interlayer is observed in the composition of the interlayers. For all the gate stacks with Al_2O_3, the amount of Ge and the ratios of Si to Ge at the interface (between full max and 1/2 height of the oxygen peak) are greater than the control HfO_2/SiGe (figure 4.8a); exact comparison of the interfacial Si/Ge ratio between the samples with Al_2O_3 (figure 4.8b-f) is challenging since the ratio can vary with slight adjustment of the nominal interface position.
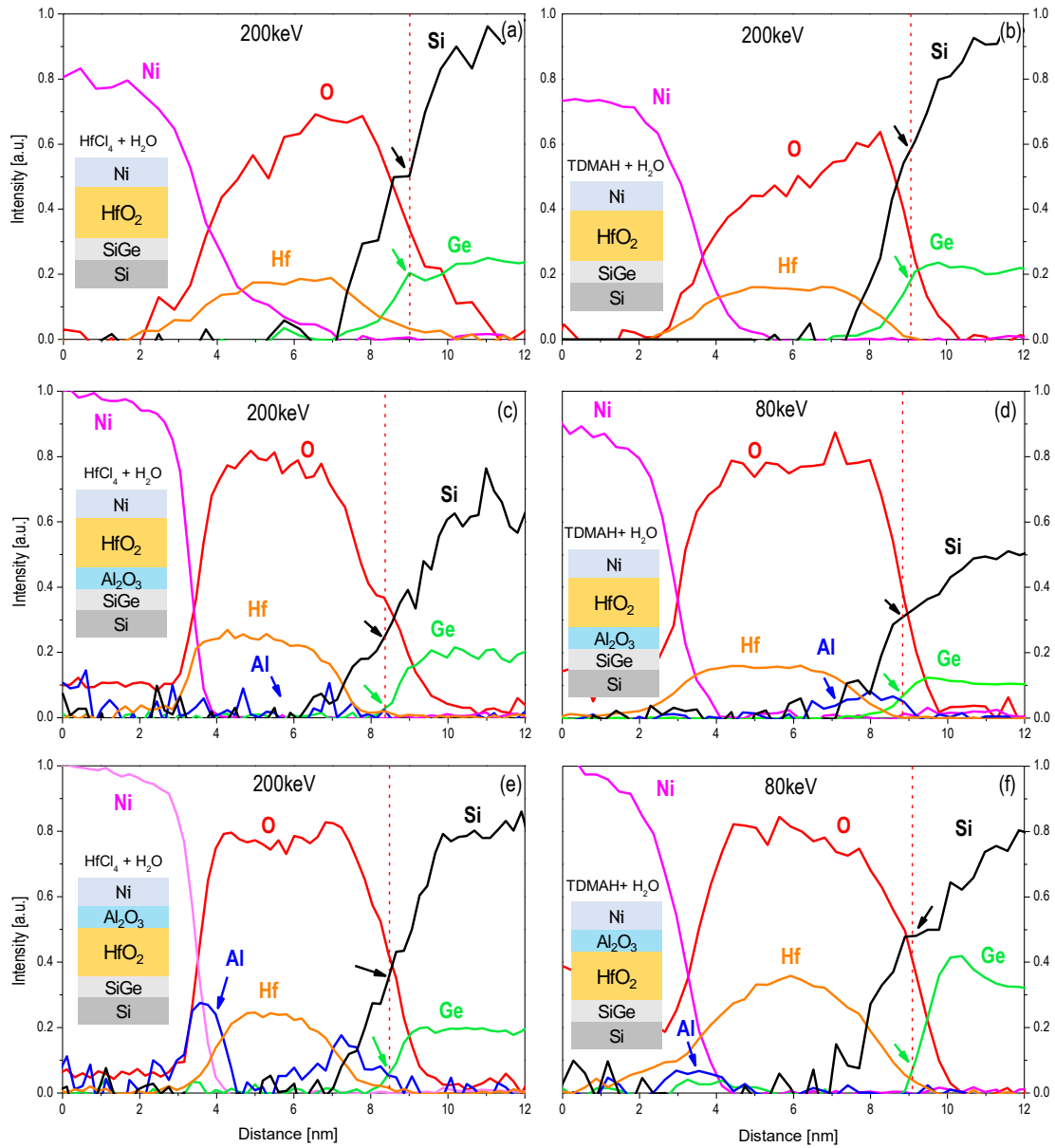
Figure 4.8 EELS analysis of MOSCAPs. EELS performed at 80keV and 200keV as indicated. The inset drawings illustrate corresponding gate stack structure along with the ALD chemistry above it. The compositions of the elements are averages area of ~6 x 0.2 nm parallel to sample surface. The red dashed line intercepts the half peak values of the O signals and indicate the SiGe - HfO_2 interface. Black and green arrows denote Si and Ge composition on the SiGe surfaces respectively. Blue arrow denotes Al composition in the oxide. Regardless of initial structure, AlO_x-HfO_2 interdiffusion is seen for bilayer samples, confirmed with raw data analysis in Fig 6 and 5. In comparison to a-b, devices in c-f show lower Ge/Si ratio at the intersection with red dashed lines indicates Si rich interface formation with Al_2O_3 incorporation into HfO_2. In contrast to Ni interdiffusion seen in a-b, Al_2O_3 insertion into HfO_2 impedes the Ni diffusion as seen in c-f.

STEM-EELS at both 80 keV and 200keV is employed to investigate the AlO_x distribution in the ALD HfO_2 layer, while controlling beam induced Al damage due to high energy electrons[77]. For the $HfO_2/Al_2O_3/SiGe$ structures (figure 4.8c and 6d), the 200 keV spectrum shows complete diffusion of the Al while the 80 keV spectrum shows only a small retention of Al at the interfaces likely due to the limited signal to noise of the 80 keV spectra; the data is consistent AlO_x diffusing during HfO_2 deposition. For the $Al_2O_3/HfO_2/SiGe$ structures (figure 4.8e and 6f), the 200 keV spectrum shows two Al peaks, one above and one below HfO_2 while the 80 keV spectrum shows a just small retention of AlO_x above the HfO_2 layer, consistent with the limited signal to noise of the 80 keV spectra. Overall both are consistent with diffusion of TMA or its reaction products into the HfO_2 when the Al_2O_3 ALD is performed after HfO_2 ALD. The nanolaminate gate stack composition studied with 80 keV EELS shows dispersed Al as shown in figure 4.9.

In comparison to control device in figure 4.8a-b, NL device in figure 4.9 shows thinner Si rich interface seen by narrower offset between O and Hf peak decays. Blue line spreads across the gate oxide indicates the uniform Al composition in the oxide. The compositions of the elements are averages area of ~6 x 0.2 nm parallel to sample surface. All the samples have an interlayer above the SiGe as shown by the gap between the Hf and O edges; however, the Si signal falls off most steeply for Si on the nanolaminate samples (figure 4.9) consistent with these samples having the most abrupt interface.

74
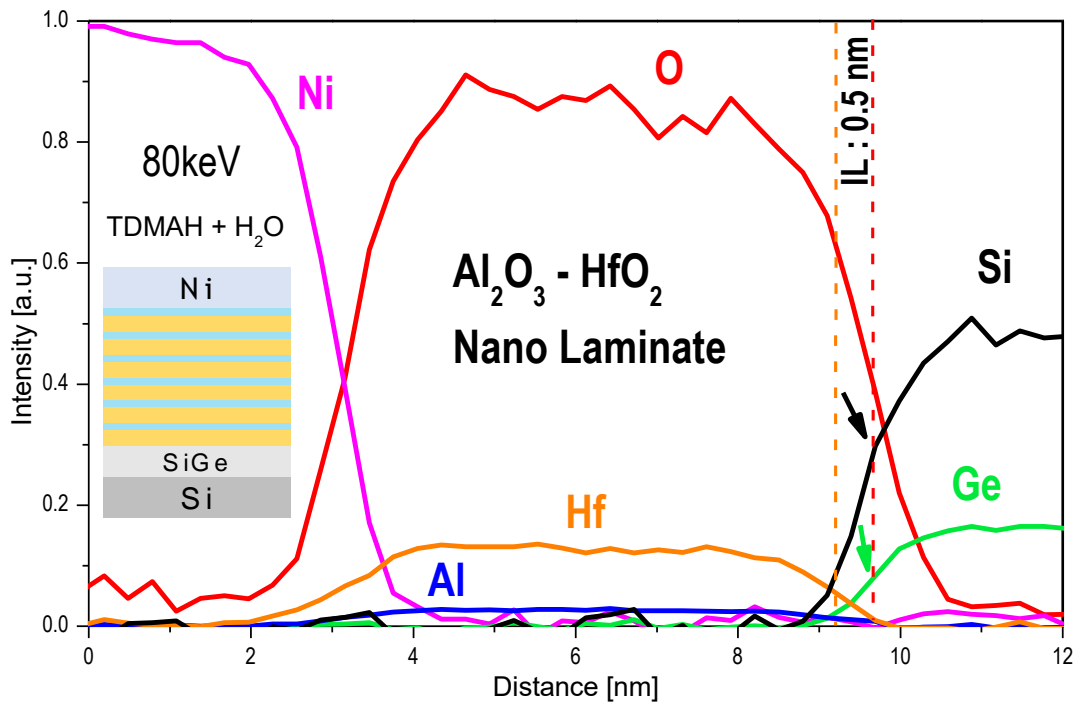
Figure 4.9 STEM- EELS analysis of nanolaminate 5 × (9HfO$_2$ + 1Al$_2$O$_3$) MOSCAP device. EELS performed at 80keV. Inset drawings which illustrates device structure along with the ALD chemistry above it. The red and orange dashed lines intercept the half peak values of the O and Hf signals respectively and indicate the SiGe - HfO$_2$ interface. Black and green arrows denote Si and Ge composition on the SiGe surfaces respectively and indicates 0.5nm thick SiO interface formation.

This unexpected interdiffusion of Al_2O_3 is also shown with EELS raw data in 3D semi-log graph in figure 4.10 (Ni/Al_2O_3/HfO_2 /SiGe) and figure 4.12 (Ni/HfO_2/Al_2O_3/SiGe). The oxide compositional profile can be seen from the electron energy loss peaks starting after element specific edges; for example, the Si K edge is at 1839 eV (orange arrow) and the Ge L edges at 1217 eV (pink arrow). The blue arrow indicates the SiGe/HfO_2 interface region. It is seen that the Ge peak decays earlier than the Si peak as a function of distance from the SiGe surface consistent with a SiO_x rich region at the interface. The black arrow indicates energy loss due to Al (K edge 1560 eV) across the oxide.

The peak intensity is significantly lower in comparison to other elements; however, it can be seen in several regions in the HfO_2 and reaches a maximum close to the HfO_2/Ni interface since it is deposited on HfO_2 as shown in focus of this area in figure 4.11 a-b. However, the Al peak can be also seen close to SiGe/HfO_2 interface, almost 4 nm away where it was deposited. The existence of Al signal in this region is consistent with AlO_x diffusion through HfO_2. A similar raw data analysis performed for Ni/HfO_2 /Al_2O_3 /SiGe bilayer device also show interdiffusion as shown in figure 4.13 a-b. However, comparison of EELS analysis for both bilayer structure indicates enhanced Al_2O_3-HfO_2 interdiffusion when Al_2O_3 is deposited prior to HfO_2 ALD.
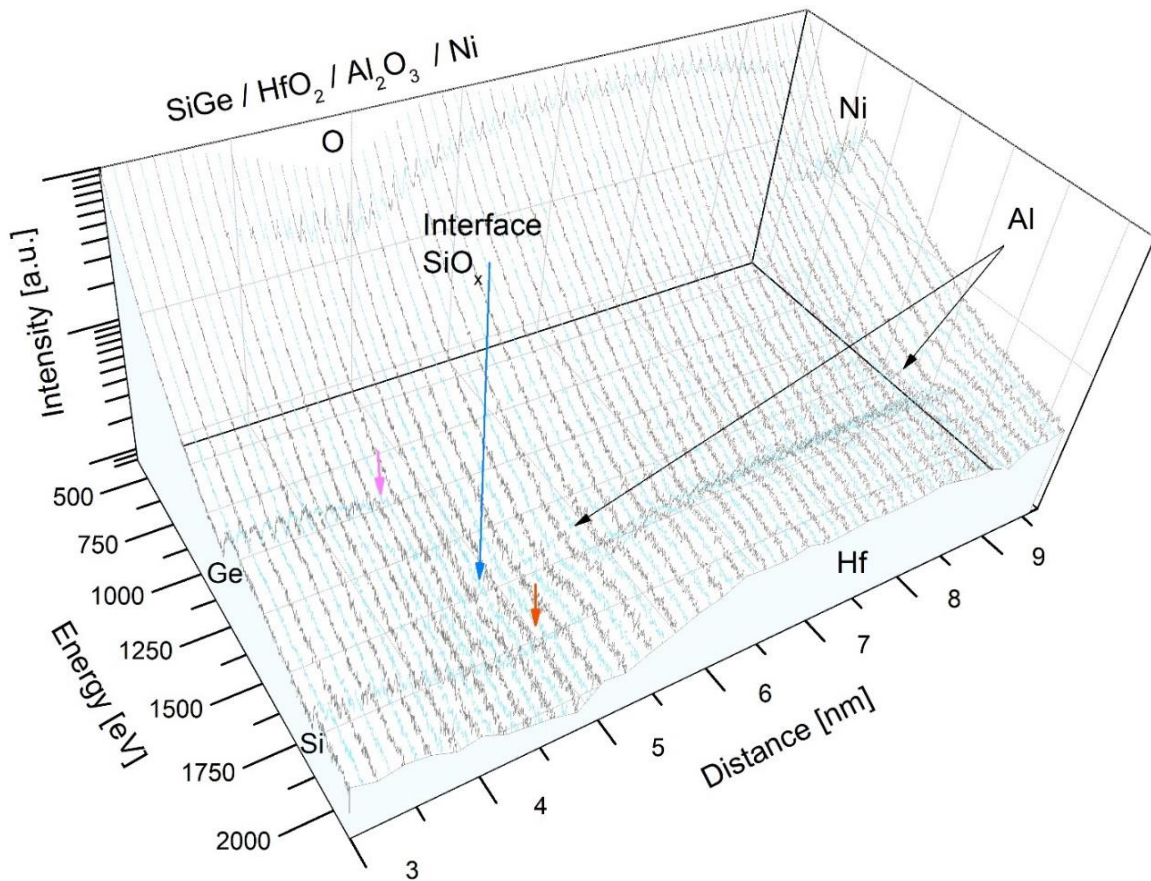
Figure 4.10 3D STEM- EELS analysis of Ni/Al₂O₃/HfO₂ /SiGe MOSCAP device. Raw EELS data taken at 200 keV from sample in Fig. 5e is shown in a 3D semi-log graph with the energy axis indicating the electron energy loss and corresponding intensity in arbitrary units. The axis labeled with distance indicates location of the electron beam on sample. The colored consecutive black and light blue lines indicate electron energy loss for the given location on samples and two colors chosen to enhance the image contrast. Each data line projects energy loss averaged from areas of 5×0.2nm parallel to the sample surface. The peaks appear on the graphs corresponds to Si K edge (1839 eV), Ge L edge 1217 eV, Hf M edge 1662 eV, O K edge 532 eV, Al K edge 1560 eV, Ni L edge 885 eV. The blue arrow indicates SiO_x interface formation between SiGe and HfO_2. Pink and red arrows indicate the Ge and Si compositions on SiGe surface. The Ge signal decays earlier than Si as it approaches the HfO_2 layer. Black arrows denote Al composition across the oxide. Al_2O_3 insertion onto HfO_2 in bilayer structure forms intermixing by Al diffusion.

77
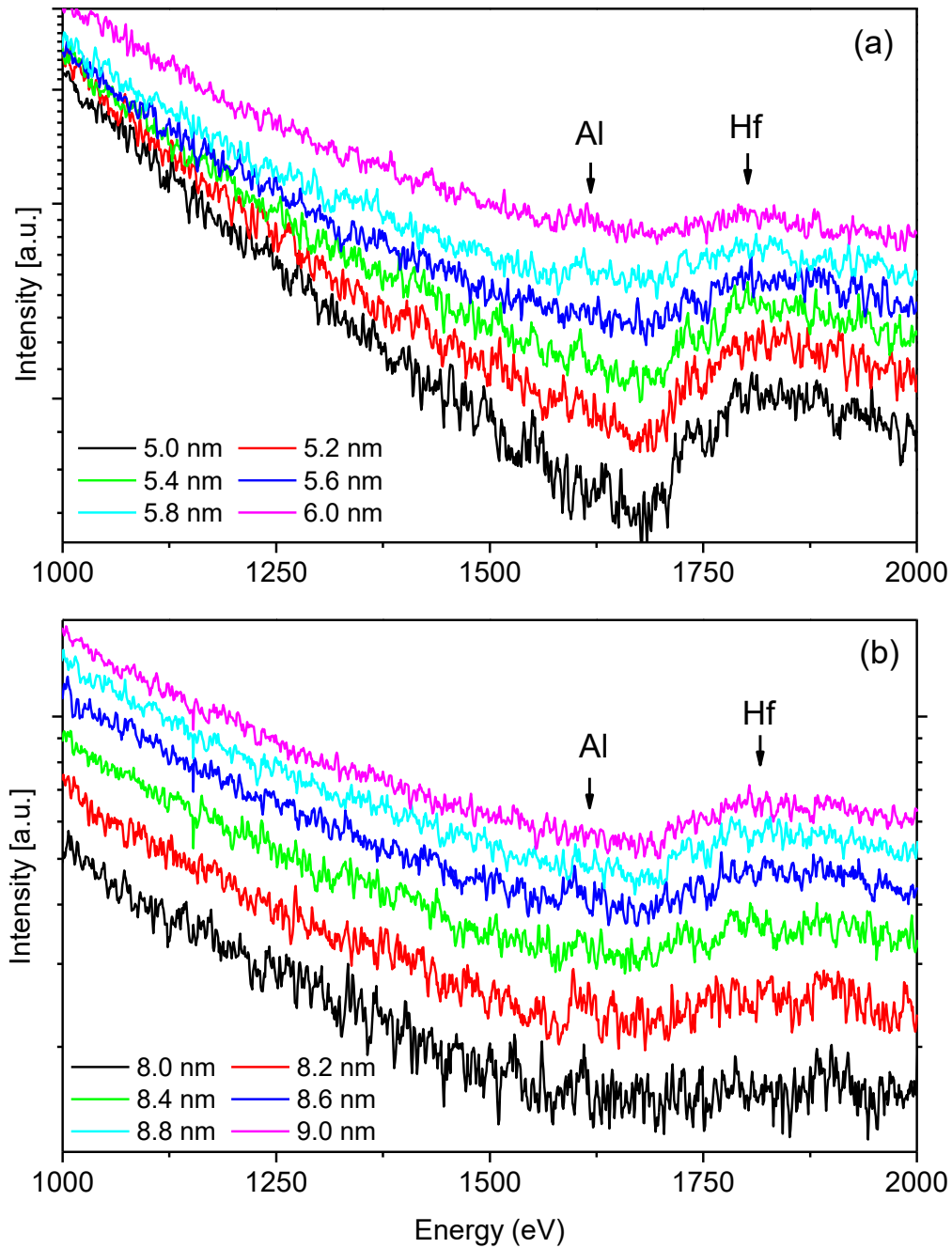
Figure 4.11 STEM- EELS raw data analysis of Ni/Al₂O₃/HfO₂ /SiGe MOSCAP. To increase the visibility of Al peak and inter diffusion, semi-log 2D graph of raw EELS data with 1-2K energy loss range 1-2KeV is presented in graph a (SiGe/HfO₂ interface region) and b (HfO₂/Ni interface region) Two graphs prepared with offsets introduced between each curve to improve visibility.
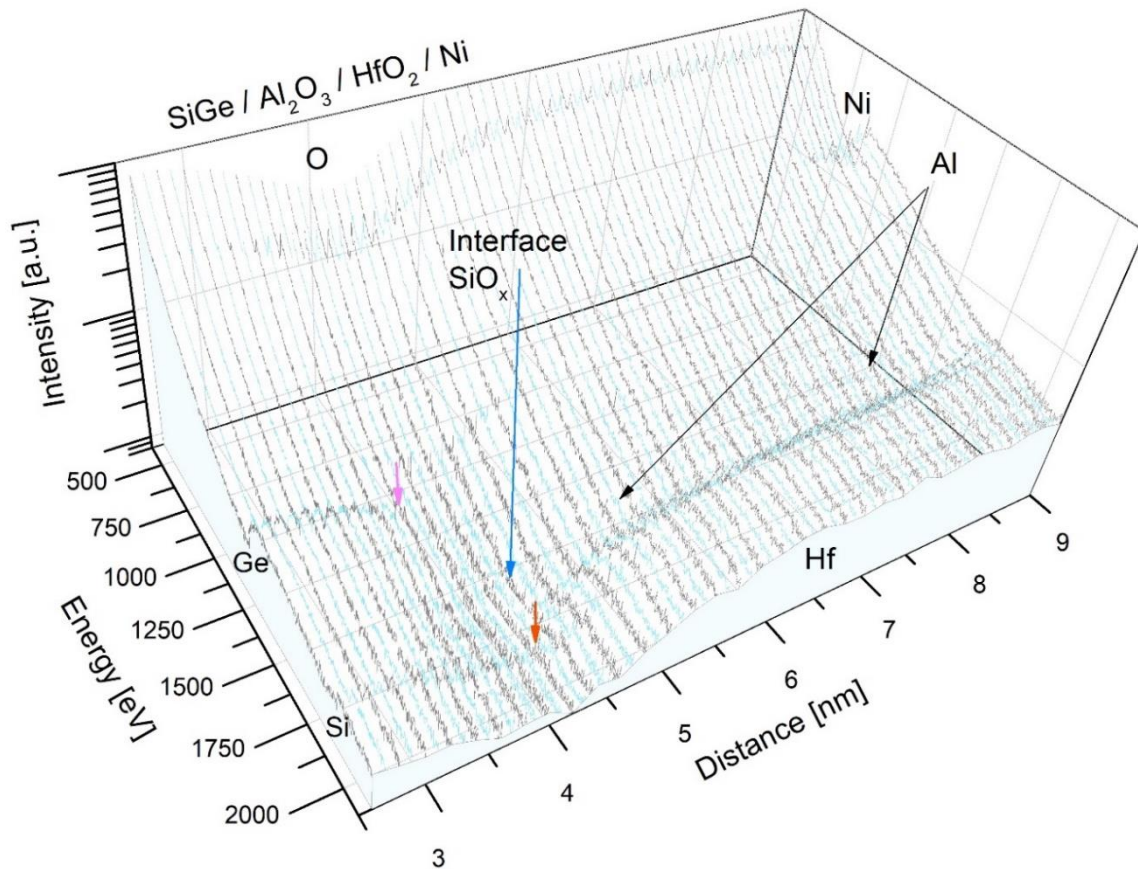
Figure 4.12 3D STEM-EELS analysis of Ni/HfO₂/Al₂O₃ /SiGe MOSCAP device. Raw EELS data taken at 200keV is shown in a 3D graph with the energy axis indicating electron energy loss and the corresponding intensity in arbitrary unit. The axis labeled with distance indicates location of the electron beam on sample. The colored consecutive black and light blue lines indicate electron energy loss for the given location on samples and two colors chosen to enhance the image contrast. Each data line projects energy loss averaged from areas of 5×0.2nm parallel to the sample surface. The peaks appear on the graphs corresponds to Si K edge (1839 eV), Ge L edge 1217 eV, Hf M edge 1662 eV, O K edge 532 eV, Al K edge 1560 eV, Ni L edge 885 eV. The blue arrow indicates SiO_x interface formation between SiGe and HfO_2. Pink and red arrows indicate the Ge and Si compositions on SiGe surface. The Ge signal decays earlier than Si as it approaches the HfO_2 layer. Black arrows denote Al composition across the oxide. Al_2O_3 insertion between SiGe and HfO_2 in bilayer structure forms intermixing by Al diffusion.

79
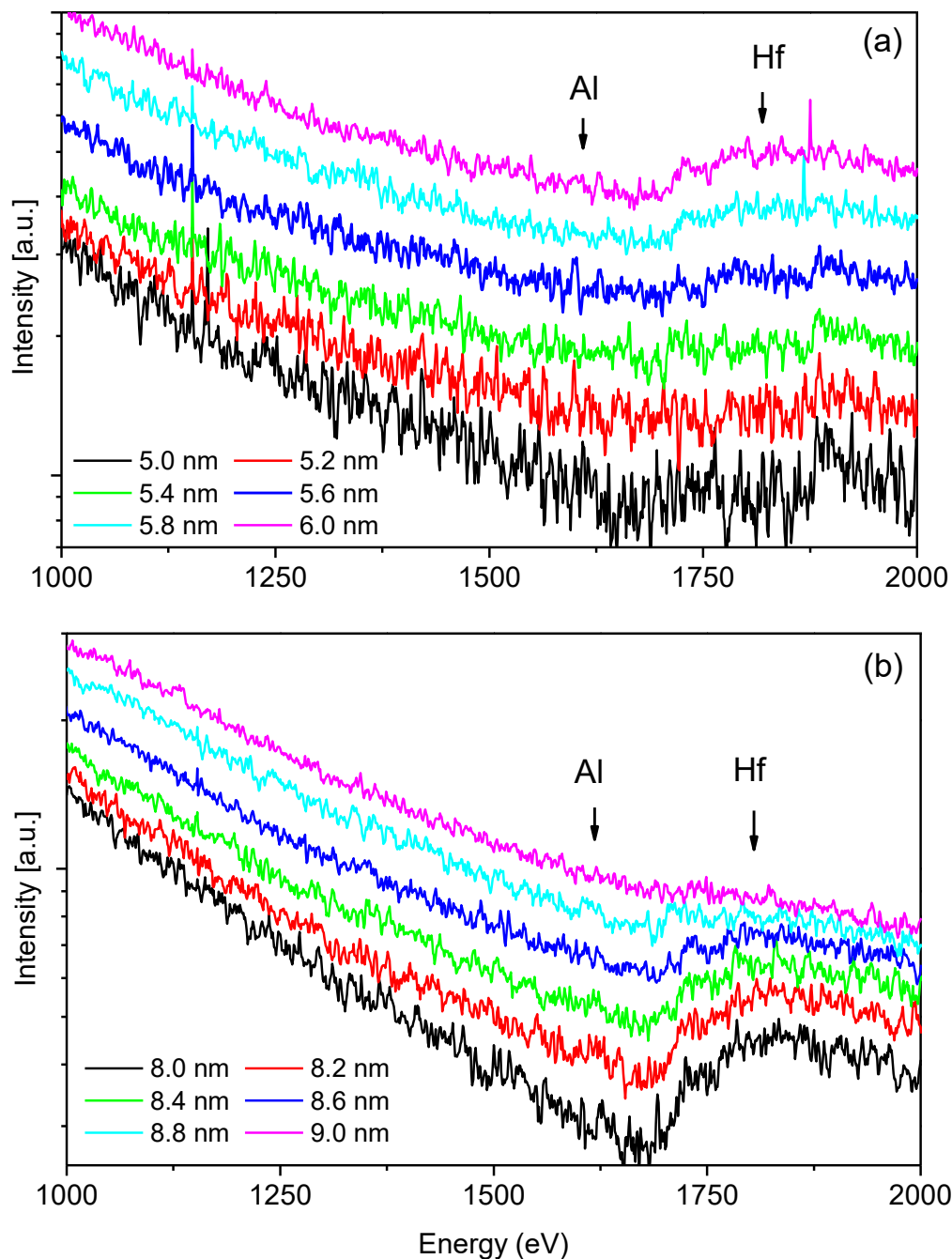
Figure 4.13 STEM- EELS raw data analysis of Ni/HfO₂/Al₂O₃ /SiGe MOSCAP. To increase the visibility of Al peak and inter diffusion, semi-log 2D graph of raw EELS data with 1-2K energy loss range 1-2KeV is presented in graph a (SiGe/HfO₂ interface region) and b (HfO₂/Ni interface region) Two graphs prepared with offsets introduced between each curve to improve visibility.
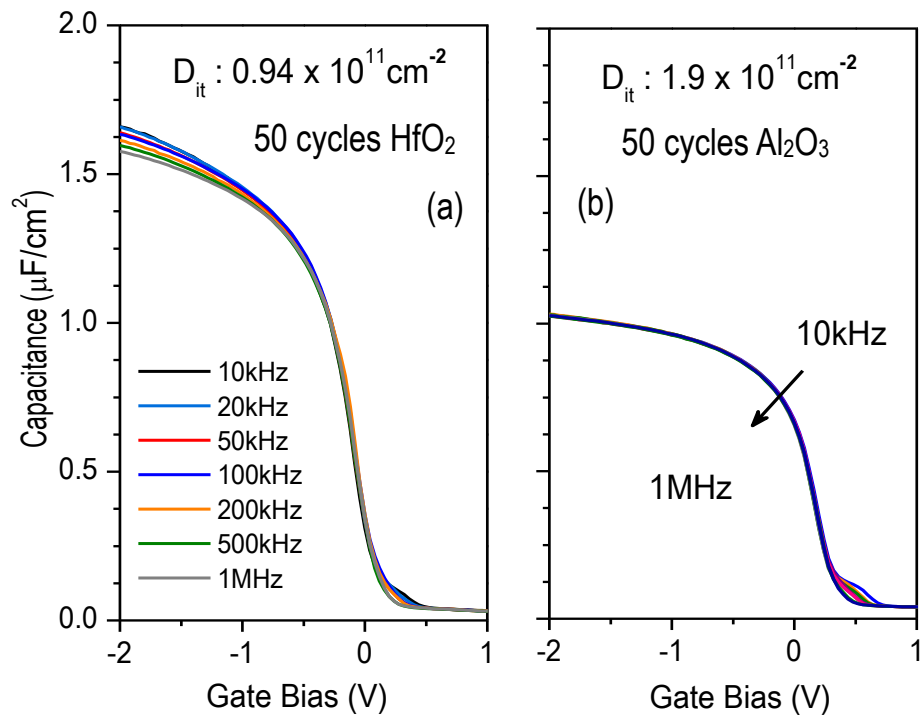
Figure 4.14 C-V graph of Ni/Al₂O₃/SiGe/Si and Al/HfO₂/SiGe/Si MOSCAPs. Both devices show very low depletion capacitance indicating similar low defect interface formation, insets values indicate integrated D_{it} values across the band gap extracted with full interface state model.

To elucidate the Al diffusion and the impacts on interface defects, Al gettering gate on HfO_2 is compared with Ni gated 50 cycles Al_2O_3 devices as shown in figure 4.14. Multi frequency C-V graphs shows almost identical depletion capacitance for both devices. Figure 4.15 shows simultaneously acquired HAADF and BF-STEM images of Ni/Al_2O_3/SiGe/Si (a-b) and Al/HfO_2/SiGe/Si (c-d) MOSCAP devices corresponds to C-V graphs in figure 4.15. In contrast to the Ni/HfO_2/SiGe/Si gate stack in figure 4.8, Al/HfO_2/SiGe/Si has a gettering gate which is known to remove oxygen from the interfaces and reduces IL thickness; this is supported by EELS analysis as shown in figure 4.16 indicating similar O and Hf peak decay profiles at the SiGe interface unlike with Ni gates which show offsets between O and Hf peak at the interface in figure 4.8a-f[72].

The gate stacks in figure 4.14 a and b have two very dissimilar oxides and show very low depletion capacitance feature resulting from charging/discharging of interface traps. Similar integrated D_{it} values are displayed in the inset. However, these two very different gate oxide structures deposited on SiGe show similar, almost abrupt interfaces with the underlying SiGe as shown in figure 4.15and 4.16. For Al/HfO_2/SiGe capacitors, it was previously shown that an Al metal gate can scavenge oxygen from the interfacial layer and reduce the interface defect density while also thinning the IL[72].
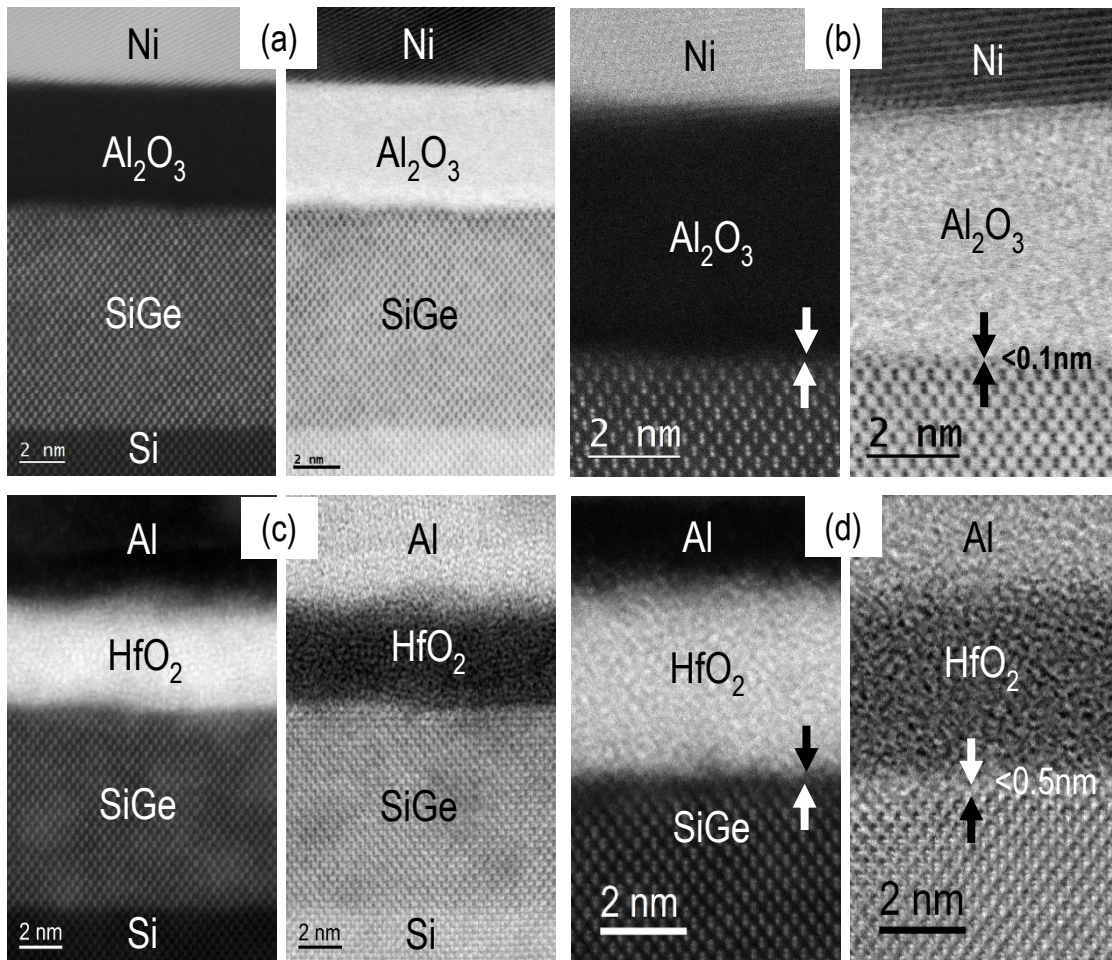
Figure 4.15 STEM images of Ni/Al₂O₃/SiGe/Si and Al/HfO₂/SiGe/Si devices. Note the Al is a gettering gate metal. High resolution STEM HAADF and BF images at 80 keV of devices with (a-b) Ni/Al$_2$O$_3$ and (c-d) Al/HfO$_2$ gate oxides; both have 50 ALD cycles. Nearly abrupt interfaces are observed in both bright field and dark field imaging for both devices. e-f) C-V graphs of Al/HfO$_2$ and Ni/Al$_2$O$_3$ devices with very low depletion capacitance are shown, insets denote integrated D$_{it}$ values across the band gap extracted with full interface state model.

For the case of the Ni/Al_2O_3/SiGe device, it is most likely that introduction Al_2O_3 ALD in the gate stack fabrication process provides an effect similar to that of an Al gate and scavenges oxygen from oxide/SiGe interface. The mechanisms are similar because TMA is a highly reactive precursor with oxygen which can interact with nearly all oxygen-containing molecules to form Al_2O_3. Insertion of each additional Al_2O_3 layer using TMA precursor can scavenge excess oxygen from the gate oxide or the high-k/SiGe interface.

It is hypothesized that TMA exposure scavenges weakly bound oxygen from the interface either by diffusing into the interface as TMA or TMA reaction products (for example monomethyl aluminum) or it decomposes the GeO_x remotely, producing suboxide species that diffuse readily through even thin Al_2O_3 (remote gettering)[13]. As TMA interacts and scavenges oxygen from the interface, it is likely that GeO_x dissociates and donates oxygen to TMA due to the lower Gibbs free energy of formation of GeO_x in comparison to SiO_x.[78] Therefore, TMA can selectively scavenge oxygen from the interface layer and reduce the interface trap density, while also thinning the IL, which has important benefits for gate stack dimensional scaling.

STEM-EELS compositional analysis for the Ni/Al_2O_3/SiGe/Si device shown in figure 4.16 supports this picture and indicates that a Si-rich interface forms, as shown by the intersection of the red dashed line marking the SiGe surface and half maximum count-rate of oxygen. The black and green arrows denote the Si and Ge composition at the oxide/SiGe interface, respectively. It is clearly seen that GeO_x composition is diminished significantly at the SiGe surface consistent with less diffusion of diffusion of GeO_x into the gate oxide and less diffusion of H_2O through the Al_2O_3 once the Al_2O_3 reaches a critical thickness.
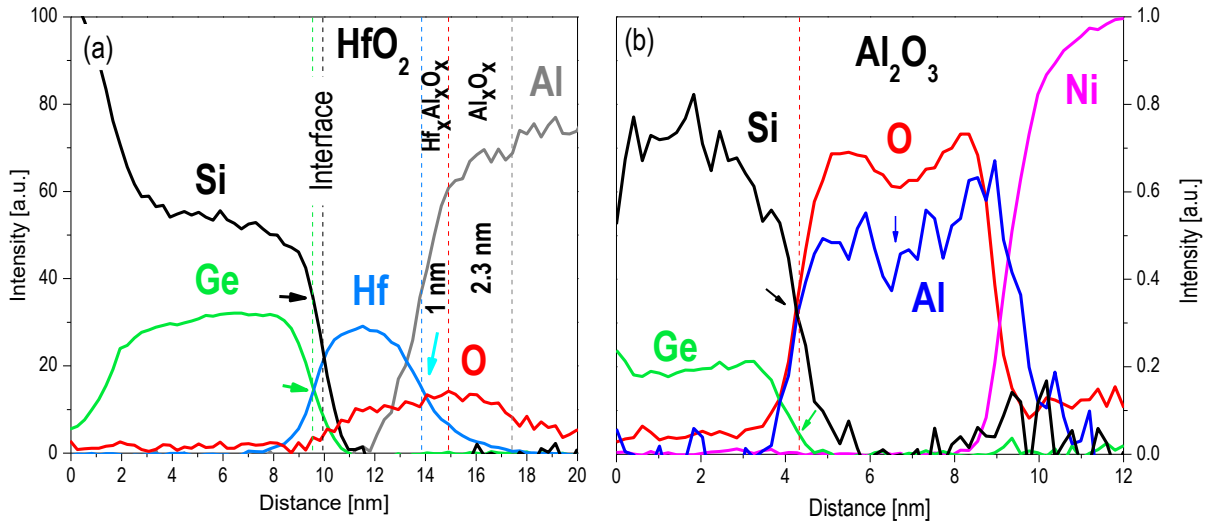
Figure 4.16 EELS analysis of Ni/Al₂O₃/SiGe/Si and Al/HfO₂/SiGe/Si MOSCAPs. EELS elemental composition of Ni/Al₂O₃/SiGe/Si is shown in g. The regions of Al₂O₃ gate oxide defined with Z contrast in a-b are in good agreement with the EELS spectra in g. The red dashed line intercepts the half peak values of the O, Si and Ge signals and delineate the SiGe-HfO₂ interface. Black and green arrows denote Si and Ge composition on SiGe surface; a Si rich interfaces observed. The blue and red arrows indicate the electron beam damaged (80keV) region of Al₂O₃. A similar effect also observed for samples studied at 2000 keV. Ni gate metal overlaying with Al indicating Ni and Al intermix. Note at the SiGe interface, the Al and O profiles are nearly identical consistent with a near zero SiGeOₓ interlayer.

4.6 Conclusion

Novel gate oxide structures were investigated which suppress electronic defects at high-k/SiGe interfaces by employing an oxygen scavenging ALD precursor, TMA. The approach utilizes the difference in the heat of formation of SiO_x and GeO_x, achieving lower interface trap densities at the high-k / SiGe interface with just a modest reduction of C_{max}. Although metallic Al remains more effective at oxygen scavenging, it induces a much larger C_{max} reduction, demonstrating the benefit of TMA remote oxygen scavenging. The data is consistent with insertion of Al_2O_3 into the HfO_2 gate oxide, removing a GeO_x component of the interlayer between the channel and the deposited gate dielectric, and suggests that effective oxygen scavenging can be achieved with TMA during ALD. This TMA based oxygen scavenging technique is most effective when the Al_2O_3 layers are uniformly distributed across the HfO_2 in a nanolaminate structure, but it also is effective when the Al_2O_3 ALD deposition occurs on top of the HfO_2. To achieve the effect, during each TMA half cycle of Al_2O_3 ALD, TMA is dosed in excess to provide sufficient TMA for reduction of additional chemical species after the surface hydroxyl groups are eliminated.

4.7 Acknowledgement

Chapter V

Suppression of electronic defects at the SiGe / high-k oxide interface via selective surface oxidation

5.1 Introduction

Previous studies on defect suppression at the gate oxide SiGe interface have included pre ALD passivation with nitrides[11,12] and sulfur[13] and post ALD selective oxygen scavenging with gettering metal gates[6,72]. However, the interfaces are still degraded by Ge out-diffusion[7] during ALD at elevated temperatures or the processes induce a large reduction in maximum capacitance by forming thicker gate oxides[72]. Conversely, modification of semiconductor oxide interfaces during the ALD process using reactive oxygen species has been shown to be effective for reduction of charge traps via formation of GeO_2 interfaces on high Ge content Si substrates (>90%) by post oxidation through Al_2O_3 using oxygen plasma[79,80] or ozone exposure[4]. In these studies, it was reported that increasing the Al_2O_3 thickness (1 to 1.5nm) on Ge substrates prior to post-oxidation reduces the GeO_x IL thickness (from 1.2 to 0.23 nm) and increases D_{it} (~5×). It was also shown that for samples subjected to post ALD oxidation, the thickness of the IL decreases for higher Ge/Si ratio in SiGe ($Si_{0.69}Ge_{0.31}$ to $Si_{0.5}Ge_{0.95}$) due to suppression of SiO_x in IL[4]. However, it was reported that low Ge content SiGe forms a $SiGeO_x$ interface which may indicate that post oxidation has a different mechanism in the low Ge SiGe which is readily epitaxially grown on Si.

In the present study, low defect interface formation with ozone exposure during gate oxide deposition is studied with impedance measurements correlated with STEM-EELS and energy resolved PES analysis to elucidate the mechanism. The impact of ozone exposure during ALD oxide deposition on the SiGe/high-k oxide interface is investigated with a large MOSCAP samples set, including gate oxides of Al_2O_3 only, HfO_2 only, and hetero Al_2O_3-HfO_2 structures. In contrast to previous reports on high Ge content SiGe[4,79], using ozone during HfO_2 gate oxide ALD is found to decrease interface defects by reducing interfacial GeO_x on $Si_{0.7}Ge_{0.3}$. Ultra-low D_{it} of 0.32×10^{12} $cm^{-2}eV^{-1}$ is observed with very thin IL (<0.2nm) on $Si_{0.7}Ge_{0.3}$ with ozone insertion into Al_2O_3 gate oxide ALD. STEM-EELS analysis shows significant interface defect reduction with SiO_x IL formation with ozone insertion into Al_2O_3 or HfO_2 gate oxide ALD on $Si_{0.7}Ge_{0.3}$.

Compositional depth profiles with PES reveal Si and Ge out-diffusion into HfO_2 during ALD growth and enhancement of Ge out-diffusion with ozone insertion which leaves a low defect SiO_x rich interface formed by selective surface oxidation. The ultra-low D_{it} observed with ozone dosing during Al_2O_3 gate oxide ALD on SiGe is consistent with two simultaneous processes: (1) Ozone depletes Ge from the interface by forming GeO and enhances Ge out-diffusion and (2) Al_2O_3 growth on SiGe directly scavenges the oxygen selectively from the oxide/SiGe interface and surface GeO_x. For HfO_2 gate oxide growth, only one of these processes is present so the ozone insertion still lowers the D_{it} by 4× but the resulting D_{it} is not as low as with Al_2O_3 gate oxide ALD.

5.2 Fabrication of the MOSCAPs

Interfacial defects at the gate oxide/SiGe interface were quantified with multi frequency impedance spectroscopy on MOSCAP devices fabricated on 8 nm thick p-type $Si_{0.7}Ge_{0.3}$(100) epitaxially grown on p-type Si (100). Degreased SiGe substrates are cleaned with cyclic HF (aq), and sulfur passivation with $(NH_4)_2S$(aq). HfO_2 ($HfCl_4$ - 250ms, H_2O – 250ms) and Al_2O_3 (trimethyl aluminum (TMA – 500ms) – H_2O – 500ms) gate oxides were grown at 300C in a Beneq TFS200 ALD reactor. After optimization of the ozone pulse length, ozone was introduced during oxide ALD in a single pulse (60 sec with 100% power at a flow rate of 4 g/h (at 100 g/Nm^3, 20°C)) such as in figure 1b, c, d or intermittently (5 sec each) (figure 5.2e "ozone nanolaminate - NL'').

Gate metal and back contacts were formed with Ni thermal evaporation and sputtering. Optimized forming gas annealing (5%H_2/95%N_2) was employed in 3 steps 300C-330C-350C for 10 min each, details of the very similar MOSCAP fabrication process can be found elsewhere[72]. Electrical characterization of the MOSCAP devices was performed with a Keysight B1500 at 300 K by I-V and multifrequency C-V, G-V measurements from inversion at 2V to accumulation at -2V. As previously documented, multiple devices on the same wafer were probed to verify the accuracy and repeatability of the interface defect density level to obtain consistent comparison between samples. This study showed that the typical standard error is 3.9%. Therefore, although absolute D_{it} calculations are accurate only within 30%; even 10% changes in D_{it} with processing conditions are reliable.

The structures and the compositions of the MOSCAP devices and interfaces were studied using electron transparent specimens (<50nm) prepared from device cross sections with a FEI Scios Focused Ion Beam using Ga ions and low energy Ar ions (<1keV) for the last step to remove the Ga beam damage. A JEOL JEM-ARM300F Transmission Electron Microscope equipped with double corrector was used in scanning transmission electron microscope (STEM) mode at 200keV both for imaging and compositional analysis. Oxide – semiconductor atomic structures were obtained from high-angle annular dark field (HAADF) and bright field (BF) z contrast images simultaneously. Similarly, the chemical composition of the devices was investigated simultaneously both with electron energy loss spectroscopy (EELS) and energy dispersive X-Ray spectroscopy (EDS) using a Gatan Quantum EELS spectrometer and dual large angle EDS detectors correspondingly. Dual EELS including zero loss and core loss spectra were collected to correct the energy shift and deconvolute plural scattering. Digital Micrograph was used for the compositional analysis and multiple linear least square (MLLS) fitting was performed after background subtraction[76].

Surface and depth compositional profiles across the gate oxide were investigated with energy-resolved photoelectron spectroscopy (ER-PES) using a nondestructive soft X-ray probe in a micro ARPES chamber equipped with a Scienta R400 analyzer at the MAESTRO beamline at the Lawrence Berkeley National Lab Advanced Light Source (ALS). Since the depth profiling with ion sputtering can alter the local oxide composition, especially in HfO_2[81,82], depth composition profiling was studied with ER-PES. ER-PES is chosen over angle resolved PES since it has a fixed experiment geometry and a small spot size, so the samples can be probed between the metal gates (figure 5.1)[53,83].

X-ray energy was varied between 150eV, 500eV and 1keV to benefit from differences in inelastic mean free path (λ) (IMFP) of the photoelectrons. It should be noted that the mean free path for elastically scattered photoelectrons can be longer than the IMFP (e.g. the elastic mean free path for photoelectrons at ~1keV in HfO_2 is ~6nm[1]).
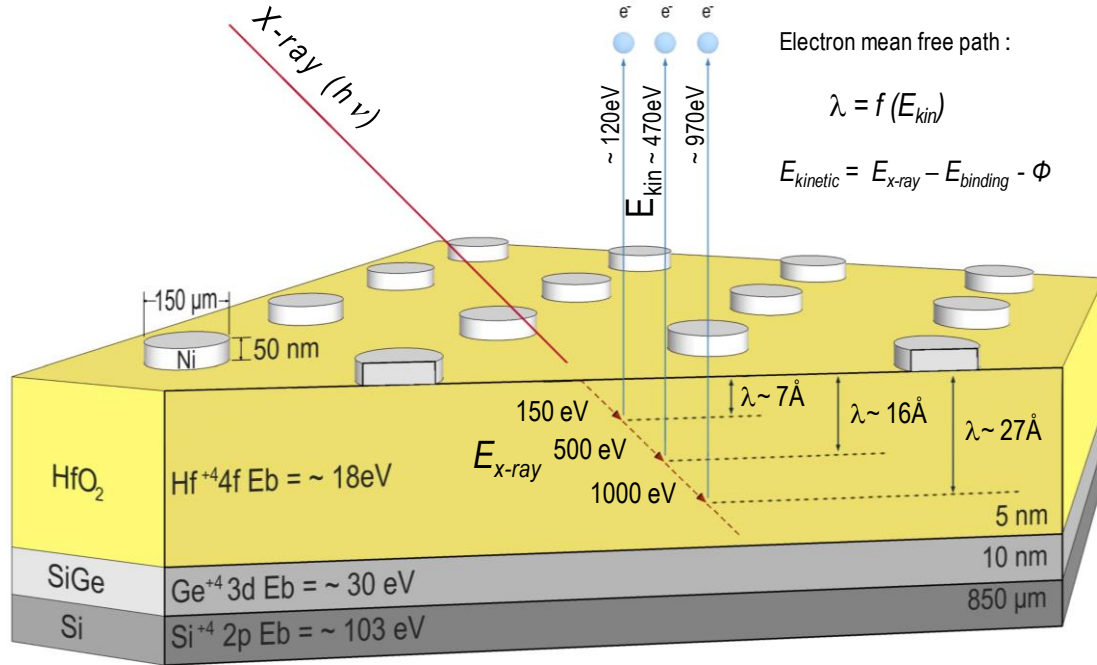
Figure 5.1 Schematics of MOSCAP structure and ER- PES experiment geometry. MOSCAP device with 5nm HfO_2 gate oxide and Ni metal gates are displayed. X-ray photons from the synchrotron source focused on sample with a beam spot of 40 x 40 μm on the HfO_2 surface between the Ni gate metals of the MOSCAP devices. Emission angle: incident photon angle to the sample normal is 54.75°. X-Ray penetration depth is much deeper than the HfO_2 and SiGe layer thickness; however, the inelastic mean free path (λ) (MFP) of the photoelectrons emitted by the elements is limited by the kinetic energy of the photo electrons. By using X-ray energy of 150eV, 500eV and 1000eV, the MFP of photoelectrons was varied, and deeper composition profiles obtained. Since the Si, Hf and Ge binding energies are similar, the IMFP of photoelectrons are similar which provides information from same depth. It should be noted that photoelectrons can be scattered elastically with longer mean free path such as photoelectrons at ~1keV in HfO_2 is ~6nm[1]; therefore, probing deeper into oxide is possible. Even for inelastically scattered electrons, only 65% of the spectrum intensity emanates within one λ of the top surface again enhancing probing deeper into the oxide.

Inelastically scattered electrons contribute only 65% to the intensity which originate within one λ of the top surface. This allows probing topmost layers due to the unique surface sensitivity obtained with low energy X-ray radiation as well as the oxide-SiGe interface probing with high energy X-rays. The incident photons and the central axis of the electron analyzer were at the same angle of 54.75° with respect to the sample normal. The soft X-ray photons were focused onto samples with a beam cross section of 40x40 μm^2 located on the HfO_2 surface between the gate metals of the MOSCAP devices as shown in figure 5.1. Each sample was probed at six points with 10 scans averaged at each point.

Compositions of the oxide at selected energy-depth were obtained by monitoring Ge 3d, Hf 4f and Si 2p XPS lines at narrow energy scan. Since the focus of the experiments is Si and Ge composition in the HfO_2 and at the interface, constant kinetic energy PES method[83] is employed by choosing the close ionization edges of Hf 4f 7/2 (14.2), Ge 3d 5/2 (29.2eV) and Si 2p 3/2 (99.4eV) to obtain similar kinetic energy photoelectrons hence similar probing depth. To avoid complication of quantization due to change in photon flux as a function of X-ray energy, the Si and Ge signal intensities are normalized with respect to the Hf 4f 5/2 signal. Details of the technique and experiment can be found in the supplement.

Data analysis, peak deconvolution and multi-peak fitting were performed with the IGOR Pro software (WaveMetrics, Inc., v.802). After Shirley background subtraction, XPS peaks were fitted using Lorentzian-Gaussian type line-shapes using the known binding energy positions. The Ge 3d5/2 peak at a binding energy of 29 eV and Hf4f 7/2 peak at 17.2eV were used as references to correct the spectral shift due to charging effects[84,85].

5.3 Electrical analysis of MOSCAPs

Multifrequency C-V measurements of the MOSCAP devices are presented in figure 5.2. Control devices with 45 ALD cycles of HfO_2 in figure 2a exhibit higher accumulation capacitance, (C_{max} = 2.25 $\mu F/cm^2$) along with high depletion capacitance indicating a high density of interface traps (D_{it} = 4×10^{12} $cm^{-2}eV^{-1}$) in comparison to all HfO_2 devices with ozone exposure during (not prior) ALD. Ozone exposure of the SiGe surface for 60 sec prior to HfO_2 deposition doubles the interface trap density to 8×10^{12} $cm^{-2}eV^{-1}$ with negligible change in C_{max} as seen in figure 5.2b. However, ozone insertion after 10 ALD cycles of HfO_2 decreases C_{max} to 2.0 $\mu F/cm^2$ and decreases D_{it} to 2.25×10^{12} $cm^{-2}eV^{-1}$ as shown in figure 5.2c. The 12% reduction in C_{max} is consistent with ozone forming a thicker interfacial layer, but the 45% decrease in D_{it} by changing the location of ozone exposure to 1 nm from the SiGe surface is significant. This effect was more prominent when the ozone is introduced after 5 cycles of HfO_2 on SiGe which induces a 55% reduction in D_{it} along with 20% decrease in C_{max} (figure 5.2d). Furthermore, when ozone is evenly dispersed into HfO_2, there is a 63% decrease in D_{it} to $1.5x10^{12}$ $cm^{-2}eV^{-1}$ compared to the control sample as shown in figure 2e. This dispersion of ozone pulses across the HfO_2 reduces D_{it} by 17% in comparison to a single 60 sec ozone pulse as shown in figure 5.2d. Instead of ozone, when water of identical pulse length is dosed for 60 sec \after 5 cycles of HfO_2 as shown in figure 5.2f, the interface deteriorates and D_{it} increased 15% compared to the control sample consistent with even common reactant species diffusing through gate oxide to the interface during ALD. The impact of ozone exposure during HfO_2 ALD is consistent with dosing ozone several nanometers from the SiGe still influencing interface trap density and, therefore, HfO_2 ALD being more complex than a true layer-by-layer process.
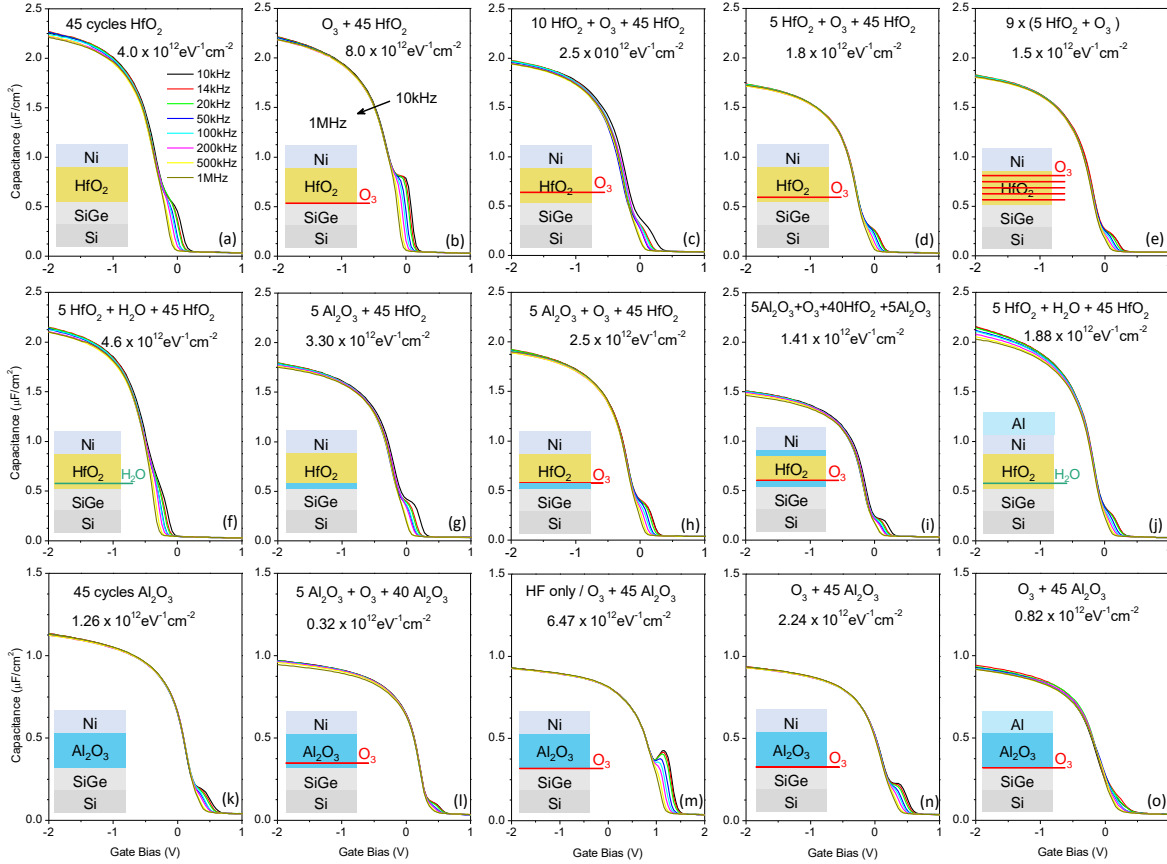
Figure 5.2 Multi frequency C-V graphs of MOSCAPs. Insets illustrate device structure for a given graph. All devices were sulfur treated prior to ALD except the device in m. (a) SiGe/45 cycles of HfO_2/Ni; (b) single 60 sec ozone dose prior to HfO_2 ALD (SiGe/60 s O_3 dose /45 cycles of HfO_2/Ni); (c) single 60 sec ozone dose after 10 HfO_2 ALD cycles (SiGe/10 HfO_2 /60 s O_3 /35 HfO_2/Ni); (d) single 60 sec ozone dose after 5 HfO_2 ALD cycles (SiGe/5 HfO_2 /60 s O_3/35 HfO_2/Ni); (e) NL with 5 sec of ozone after each 5 HfO_2 ALD cycles SiGe/9×(5 HfO_2+5s O_3) /Ni ; (f) bilayer device (SiGe/5 Al_2O_3/45 HfO_2 /Ni); (g) 5 sec H_2O dose between Al_2O_3 and HfO_2 ALD (SiGe/5s H_2O/5 Al_2O_3/45 HfO_2/Ni); (h) 60 sec ozone dose between Al_2O_3 and HfO_2 ALD cycles (SiGe/5 Al_2O_3/60s O_3/45 HfO_2/Ni); (i) 60 sec ozone pulse between Al_2O_3 and HfO_2 ALD cycles in tri-layer structure (SiGe/5 Al_2O_3 /60s O_3 /45 HfO_2 /5 Al_2O_3 /Ni); (j) 5 sec H_2O pulse after 5 cycles of HfO_2 deposition (SiGe/5s H_2O/5 H_2O/40 HfO_2 /Ni); (k) Control Al_2O_3 device (SiGe/45 Al_2O_3/Ni); (l) single 60 sec ozone pulse after 5 Al_2O_3 ALD cycles (SiGe/5 Al_2O_3 /60 s O_3 /35 Al_2O_3 /Ni); (m) single 60 sec ozone pulse prior to Al_2O_3 ALD, (SiGe/60 sec O_3 dose 45 cycles of Al_2O_3 /Ni), this device has only HF treatment; (n) single 60 sec ozone dose prior to HfO_2 ALD (SiGe/60 sec O_3 dose /45 cycles of HfO_2/Ni); (o) single 60 sec ozone dose prior to HfO_2 ALD with Al gettering gate (SiGe/60 sec O_3 dose /45 cycles of HfO_2/Al). The inset D_{it} indicates peak interface defect density in bandgap extracted with full interface state model. Ozone dose prior to HfO_2 ALD (b) increases D_{it} and ozone dose after few cycles of HfO_2 ALD (c-e) decreases D_{it}.

94

To elucidate the D_{it} reduction mechanism at the SiGe/HfO$_2$ interface by ozone exposure into HfO$_2$, several HfO$_2$ only and HfO$_2$-Al$_2$O$_3$ hetero gate oxides with ozone exposures are compared. A control Ni/45 cycles of HfO$_2$ + 5 cycles of Al$_2$O$_3$/SiGe device with 1.75 μF/cm^2 and D_{it} of 3.3x10^{12} cm^{-2}eV^{-1} is shown in figure 5.2g. In comparison to the 45 ALD cycle HfO$_2$ only control device in figure 5.2a, the control hetero oxide bilayer device exhibits a 18% decrease in D_{it} to 3.3×10^{12} cm^{-2}eV^{-1} consistent with oxygen scavenging by the TMA precursor, and a 23% decrease in C_{max} due to increase in total oxide thickness along with the lower dielectric constant of Al$_2$O$_3$ in comparison to HfO$_2$. In comparison to the bilayer control sample in figure 5.2g, the ozone exposed bilayer device in figure 5.2h exhibits only a 25% decrease in D_{it} with negligible change in C_{max}.

It is hypothesized that ALD of the bottom Al$_2$O$_3$ layer induces GeO$_x$ decomposition to Ge by oxygen scavenging; in addition, the bottom Al$_2$O$_3$ may reduce both O$_3$ and GeO$_x$ diffusion, but this is likely to be a minor effect since as shown below ozone is very effective in reducing D_{it} for Al$_2$O$_3$ gate oxides. In sum, the ozone only has a modest effect bilayer since the interfacial GeO$_x$ is already at low concentration, this more modest effect of ozone on bilayer samples is consistent with both ozone and TMA dosing reducing interfacial GeO$_x$ but using different chemical processes.

To study the decrease in trap density at the Al$_2$O$_3$/SiGe interface by ozone insertion, a set of samples with only Al$_2$O$_3$ gate oxide with and without ozone insertion was fabricated (figure 5.2k – o). The control 45 cycles of Al$_2$O$_3$ devices had a C_{max} of 1.12 μF/cm^2 and 1.26×10^{12} cm^{-2}eV^{-1} as shown in figure 5.2k.

In comparison to control HfO_2 in figure 5.2a and control hetero $Al_2O_3 - HfO_2$ devices in figure 5.2f, Al_2O_3 only devices exhibit a 70% and 60% lower interface trap density respectively consistent with oxygen scavenging by TMA exposure during Al_2O_3 growth. For ozone insertion into Al_2O_3 after 5 ALD cycles of Al_2O_3 on SiGe as shown in figure 5.2l, the depletion capacitance almost disappears consistent with a 75% decrease in D_{it} to 0.32×10^{12} $cm^{-2}eV^{-1}$ along with a small decrease in accumulation capacitance in comparison to the control device in figure 5.2k. Conversely, when SiGe is exposed to ozone prior to Al_2O_3 growth, the D_{it} increases significantly without (figure 5.2m) and with sulfur treatment (figure 5.2n) prior to Al_2O_3 growth. The sulfur passivated surface showed lower D_{it} consistent with sulfur reducing GeO_x[13]. The 75% decrease in D_{it} for ozone dosing of Al_2O_3/SiGe devices is consistent with both ozone and TMA dosing reducing interfacial GeO_x but using different yet complementary chemical processes. The TMA reduces GeO_x by gettering the oxygen to form Al_2O_3, and it is hypothesized the ozone promotes GeO_x sublimation to form a Si rich interface.

It is hypothesized that two distinct processes take place when ozone is inserted during Al_2O_3 ALD: 1) D_{it} reduction with ozone and 2) oxygen scavenging with remote oxide (TMA) gettering. To confirm the importance of remote gettering and its synergy with ozone dosing for even HfO_2 based gate oxides, both a top Al_2O_3 layer was grown on HfO_2 (figure 5.2i) as well as a traditional Al gettering gate (figure 5.2j). Compared to an ozone dosed HfO_2-Al_2O_3/SiGe bilayer device (figure 5.2h), the ozone dosed Al_2O_3-HfO_2-Al_2O_3/SiGe tri-layer device (figure 5.2i) exhibits a 44% decrease in D_{it}. This is consistent with remote oxygen scavenging by Al_2O_3 ALD grown on top of HfO_2 which is shown to be an effective method for IL modification for D_{it} reduction even 4nm away from SiGe surface.

In the second remote scavenging example, an Al metal remote gettering gate is employed which is separated from the gate oxide with a thin Ni layer as shown in figure 5.2j. This sample was also exposed to additional intentional water exposure after 5 cycles of HfO_2 to deteriorate and increase interface defects. In comparison to the control sample in figure 5.2f, the device with remote Al gettering gate exhibits a 60% decrease in D_{it} with negligible decrease in C_{max}. The data is consistent with the remote gettering by Al metal or a top surface Al_2O_3 ALD layer reducing the D_{it} by a mechanism which is independent of the D_{it} reduction by ozone or increase by H_2O insertion during gate oxide ALD.
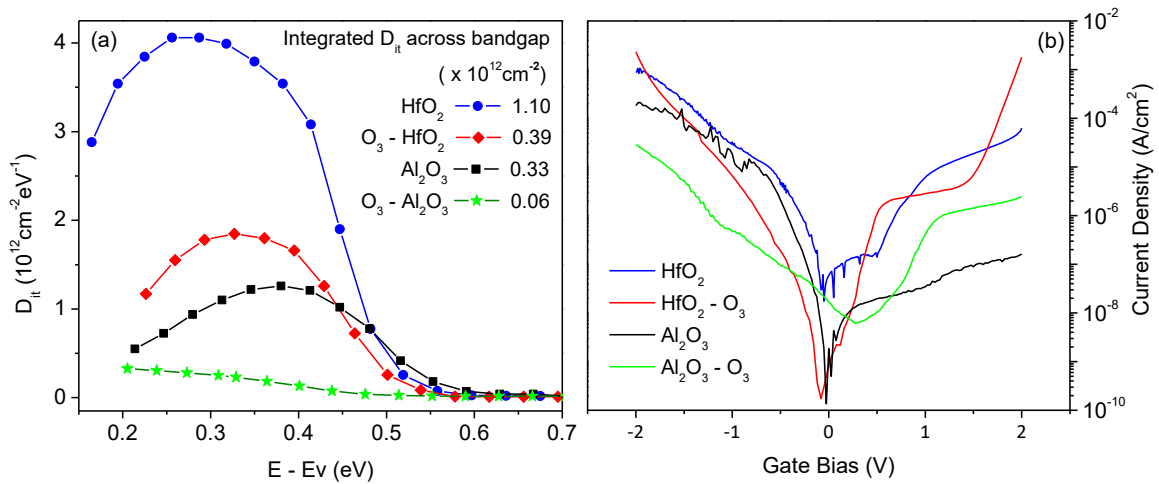
Figure 5.3 Defect Density Distribution and Leakage Current of MOSCAPS. (a) Interface defect density distribution of MOSCAPs across the band gap. b) Leakage current density across the gate oxide for the devices**.** The full interface state model was used to extract the defect density across the bandgap. In comparison to the 45 cycles HfO_2 control device with 4×10^{12} $eV^{-1}cm^{-2}$ (peak D_{it}), ozone pulsed bilayer devices with 5 ALD cycles of HfO_2 /60 sec O_3/40 ALD cycles of HfO_2 showed 1.8×10^{12} $eV^{-1}cm^{-2}$. Defect density was significantly lower for Al_2O_3 control devices in comparison to control HfO_2 and decreased further with ozone insertion for 5 Al_2O_3/60 sec O_3/40 ALD cycles of Al_2O_3 which exhibited 0.3×10^{12} $eV^{-1}cm^{-2}$. Inset values indicates total defect density across the band gap and showed more prominent decrease in trap density by ozone insertion. Devices with ozone also indicates lower leakage current in comparison to control devices indicated in I-V graph on the right.

Interface defect distributions across the band gap for selected devices calculated with the full interface state model are shown in figure 5.3a. Ozone insertion into HfO_2 only and Al_2O_3 only samples reduced interface traps charges almost uniformly across the bandgap; the integrated D_{it} across the bandgap exhibit 65% and 82% decreases, respectively. In addition, ozone insertion into devices reduces the leakage current consistent with thicker IL formation with ozone pulsing as shown in figure 5.3b. It is hypothesized that the ozone dosed Al_2O_3 sample (figure 5.2l) had exceptionally low D_{it} because two complementary mechanisms of D_{it} reduction are active: 1) D_{it} reduction with ozone exposure and 2) D_{it} decrease with remote oxygen scavenging via top surface Al_2O_3 ALD. In contrast, for the HfO_2 only device exposed to ozone in figure 5.2, there is only a single D_{it} reduction mechanism.

5.4 Structural analysis of MOSCAPs

The interlayer and oxide thicknesses of the selected devices are determined from STEM-HAADF and STEM-BF recorded simultaneously from the MOSCAP device structure with the electron axis parallel to the Si <110> direction as shown in figure 5.4. The control Al_2O_3 device in figure 5.4a&f had a darker (HAADF)/brighter (BF) IL region of 0.4 nm along with a 4.9 nm gate oxide thickness indicated with black and white arrows as obtained with z contrast; below these assignments are confirmed with compositional analysis. Insertion of ozone into Al_2O_3 forms an IL of similar thickness ~0.2 nm and increases gate oxide thickness to 5.5 nm as shown in figure 5.4b&g. In contrast, insertion of ozone into HfO_2 increases the IL thickness from 0.9 nm to 1.1 nm and increases the gate oxide thickness from 4.2 nm to 4.4 nm as shown in figure 5.2 c&h vs 2d&i. Both results are consistent with the decrease in C_{ox} with ozone insertion into Al_2O_3 (figure 5.2k vs 2l) and into HfO_2 (figure 5.2a vs 2d); however, the mechanism of D_{it} reduction necessitates the compositional analysis to elucidate the differences in ozone induced reduction/growth with Al_2O_3 vs HfO_2.
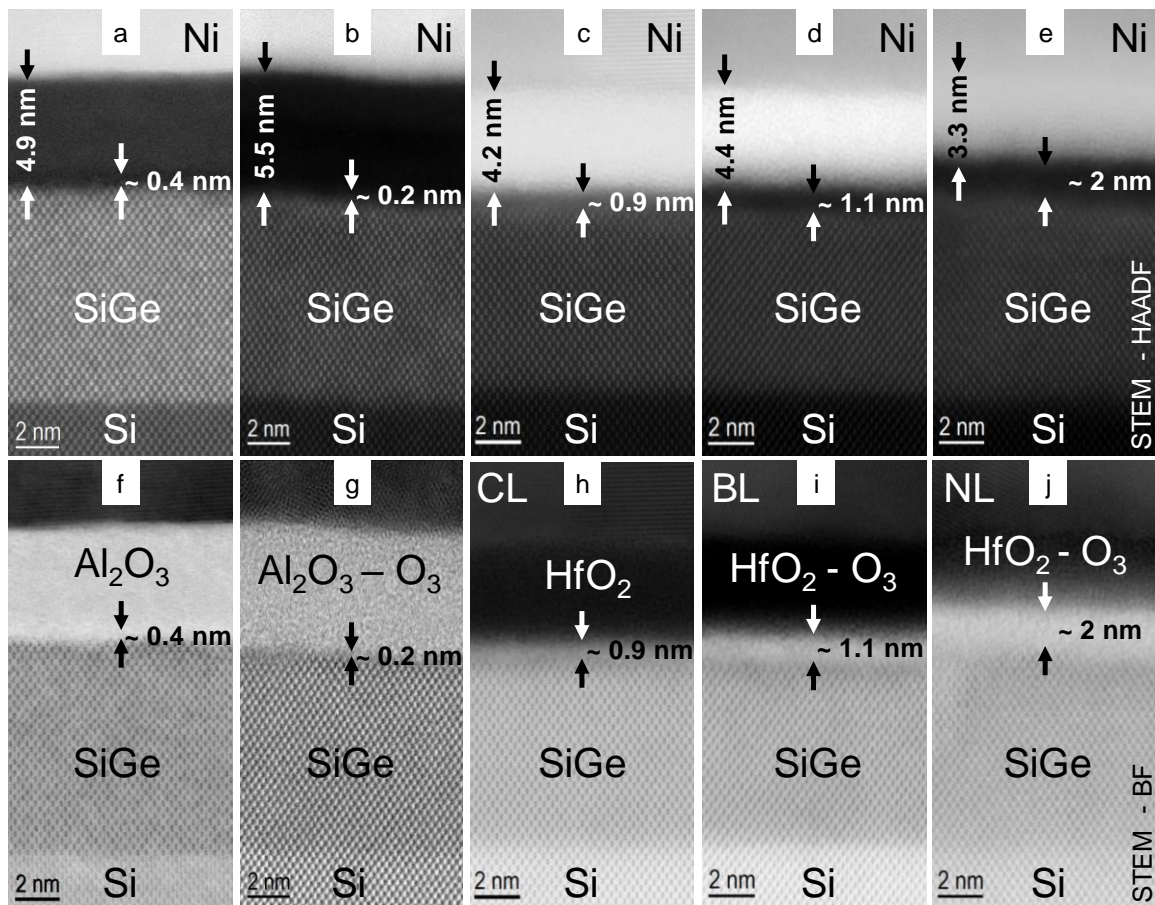
Figure 5.4 STEM HAADF and BF images of MOSCAPs (a, f) 45 cycles of Al_2O_3; (b, g) 5 cycles of Al_2O_3/60 sec O_3/40 cycles of Al_2O_3 (c, h) control device of 45 cycles HfO_2; (d, i) bilayer device with 5 cycles of HfO_2/60 sec O_3/ 40 cycles of HfO_2/Ni structure; (e, j) nanolaminate with 9 x (5HfO_2 + 5 sec O_3) ALD cycles. In these images, the oxide structures and regions are defined according to z contrast. The interfacial layer between SiGe and oxide are indicated with black and white arrows on corresponding STEM-HAADF and BF images. The control Al_2O_3 device had a 0.4 nm low z interface layer in comparison to < 0.2 nm thick IL in the ozone-Al_2O_3 device. In comparison to control device of HfO_2/SiGe (c&h), bilayer (d&i) and NL (e&j) showed thicker interfaces consistent ozone forming thicker oxide at the interface.

5.5 Compositional analysis of MOSCAPs

STEM-EELS compositional analysis of the selected devices along with associated structures are shown in figure 5.5. STEM-HAADF and BF field intensity graphs correlated with the EELS analysis are also shown. Note that these STEM images are a representation of similar areas where EELS analysis was performed but are not taken simultaneously with EELS due to experiment restrains. A multiple linear least square (MLLS) fitting procedure[76] is employed to resolve Al, Hf and Si spectroscopic overlay issues. The IL regions are shaded blue and located between the half max of oxygen and the half max Hf. For the Al_2O_3 sample, since there is electron beam induced damage seen in the middle of oxide, the half max of the Al is defined by extrapolation of max peak point for the Al signal which is estimated to be 75 (a.u.). The blue IL boundaries are confirmed by correlating the EELS with the corresponding STEM z contrast intensity graphs. The Si - Ge composition in IL is denoted with black and pink arrows respectively; the arrows points to the Si and Ge concentrations in the middle of the interlayer.

As shown in the control HfO_2 device in figure 5.5a, the Hf and O signals have offsets indicating a thick $Si_xGe_xO_x$ IL; the black and pink arrows show high Ge composition in this IL. In contrast, the control Al_2O_3 device in figure 5.5b has thinner interlayer because the Al and O signals decay in similar positions. The Al_2O_3 IL has only a small Ge signal (pink) indicating Si rich IL formation. Note that the EELS data indicates a significant Al component in the Al_2O_3/SiGe interlayer, so the IL may be $AlSiO_x$.

101
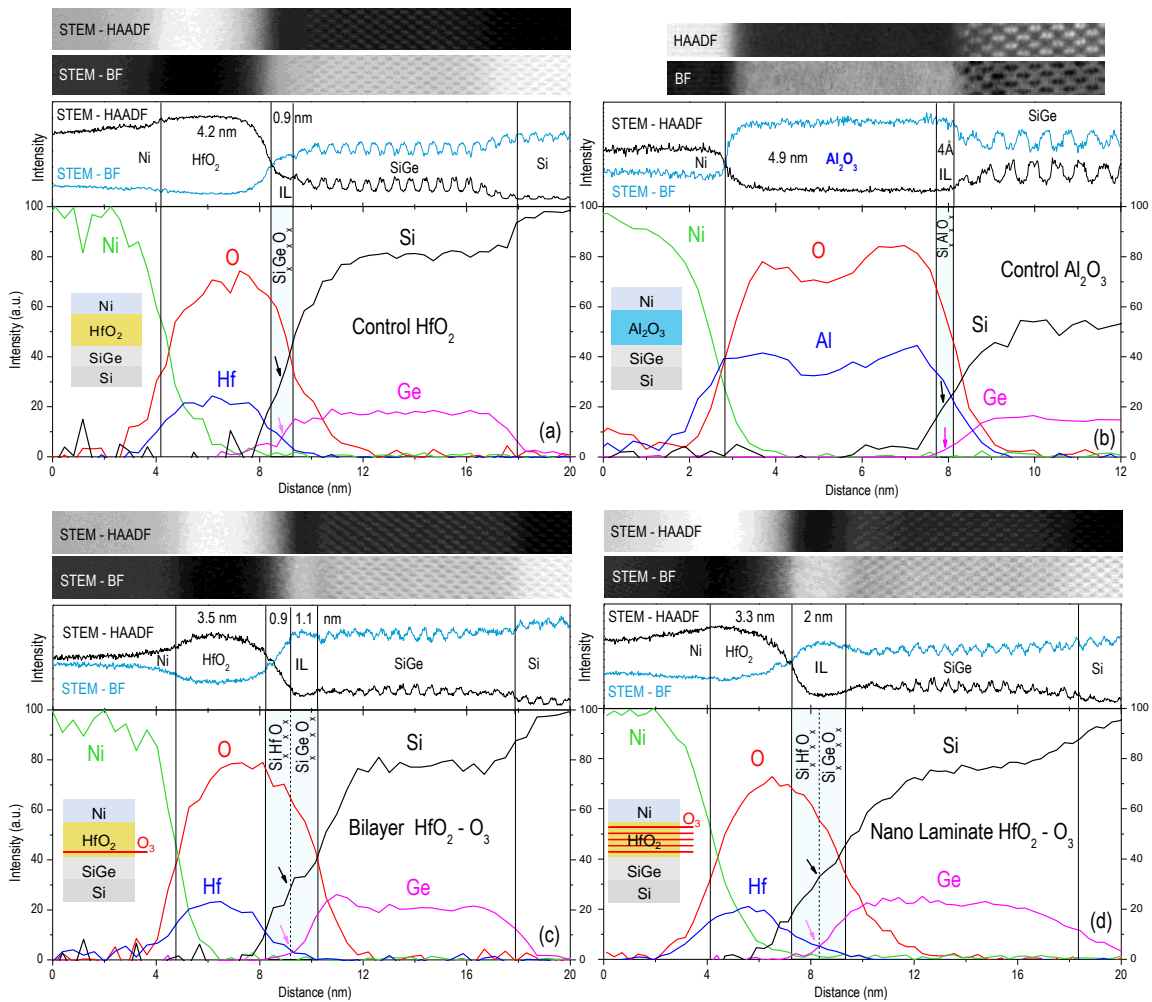
Figure 5.5 STEM- EELS analysis of MOSCAPs. (a) 45 cycles of HfO₂ control device; (b) 45 cycles of Al₂O₃ control device (c) bilayer device with 5 ALD cycles of HfO₂ / 60 sec O₃ / 40 ALD cycles of HfO₂ structure; (d) NL with 9 x (5HfO₂ + 5 sec O₃) ALD cycles devices. Insets illustrate the corresponding device structure. The graphs above the EELS data indicates the intensity of the STEM – HAADF and BF images. Note that the STEM images are not taken simultaneously with EELS due to experimental constrains. Correlation were made between EELS sampled area and STEM imaged area in scale to define the regions of the oxide. The compositions of the elements were averages areas of ~6 x 0.2 nm parallel to sample surface. The blue shaded areas correspond to the interlayer thickness and boundaries defined with the half peak values of the O and Hf signals. Comparison of the blue shaded areas of a vs c and d indicate the SiGe - HfO₂ interface layer was increased by ozone insertion. Black and pink arrows denote Si and Ge compositions in the I. Compared to control HfO₂, Al₂O₃ control device in b showed diminished Ge at the IL. The control HfO₂ device showed Ge tail in the interface (a) which diminished for the ozone dosed devices in c and d. Unlike NL ozone device in d, bilayer ozone device in c showed Ge accumulation close the SiGe. Si/Ge ratio was highest for the NL device indicating a Si rich interface

The ozone bilayer HfO_2 device shown in figure 5.5c has a larger offset between the Hf and O signals with diminished Ge signal in IL (pink arrow) in comparison to the control device in figure 5.5a, consistent with a thicker Si rich IL region. This ozone bilayer HfO_2 IL has a region which is Hf poor, so it is divided with a dashed line to distinguish regions of $Si_xGe_xO_x$ and $Si_xHf_xO_x$. In addition, the Si peak beyond half max of oxygen extends further into the gate oxide for the ozone bilayer HfO_2 (3 nm from the right edge of the blue region) compared to control HfO_2 (1.5 nm from the right edge of the blue region), consistent with ozone enhancing Si diffusion into HfO_2; the ozone enhanced diffusion of Si is confirmed by PES data below. Last, for ozone bilayer (figure 5c), a slightly increased Ge peak beneath the SiGe surface is seen, consistent with Ge pile up underneath the SiGe layer[15,63].

When ozone is dispersed into HfO_2 as shown in figure 5d, the Hf – O offset was increased along with similar $Si_xGe_xO_x$ and $Si_xHf_xO_x$ formation. Similar to bilayer ozone in figure 5.5c, the Si signal in the ozone nanolaminate (figure 5.5d) extended further into HfO_2 (3.8 nm from the right edge of the blue region), consistent with ozone enhancing Si diffusion into HfO_2 mostly in the IL region. Therefore, the ozone insertion into HfO_2 increases the IL thickness along with increasing the SiO_x concentration in the IL and maybe in HfO_2, whereas ozone decreases the IL thickness and does not change the Si diffusion into the gate oxide for Al_2O_3, which is consistent with Al_2O_3 being a better diffusion barrier to both GeO_x and SiO_x than HfO_2.
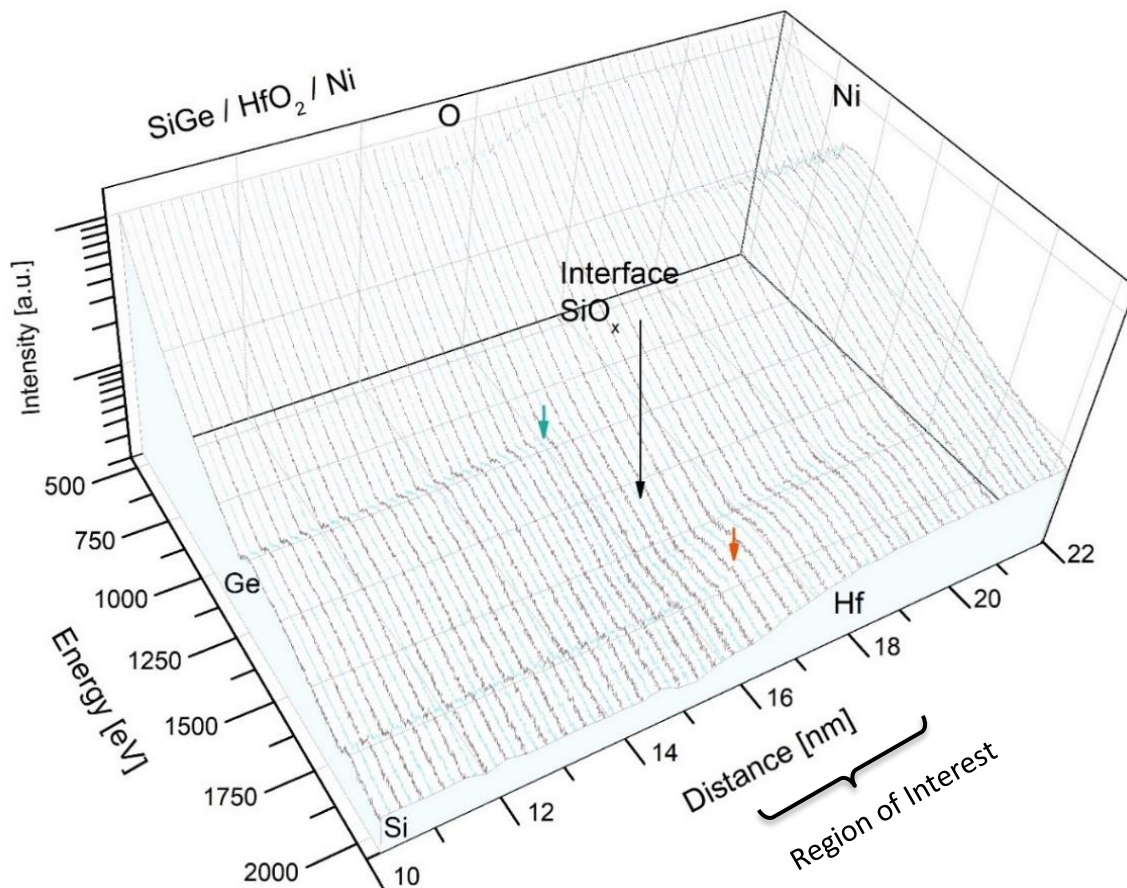
Figure 5.6 3D STEM-EELS analysis of 9 × (5HfO$_2$ + 5 sec O$_3$) NL device. Raw EELS data obtained at 200 keV from 9 x (5HfO$_2$ + 5 sec O$_3$) NL sample is shown in a 3D semi-log graph with the energy axis indicating the electron energy loss and corresponding intensity. The axis labeled with distance indicates location of the electron beam on the sample. The colored consecutive black and light blue lines indicate electron energy loss for the given location on samples and two colors chosen to enhance the image contrast. Each data line projects the energy loss averaged from areas of 5 × 0.2nm parallel to the sample surface. The peaks appear on the graphs corresponds to Si K edge (1839 eV), Ge L edge 1217 eV, Hf M edge 1662 eV, O K edge 532 eV, Ni L edge 885 eV. The black arrow indicates SiO$_x$ interface formation between SiGe and HfO$_2$. Orange and green arrows indicate the Si and Ge compositions on SiGe surface. The Ge signal decays earlier than Si as it approaches the HfO$_2$ layer.

For better illustration of the Si and Ge distributions, raw EELS data for HfO_2 with dispersed ozone (NL device) is shown in a 3D semi-log graph in figure 5.6. The elemental profiles of the oxide can be seen from the peaks arising after element specific edges due to electron energy loss; for example, Hf M edges at 1662 eV and the O K edge at 532 eV. The blue arrow indicates the $SiGe/HfO_2$ interface region. Tracing the Si and Ge signal from SiGe into HfO_2 region, Ge decay (green arrow) is observed earlier than the Si decay (orange arrow) consistent with a SiO_x rich IL formation.

Side by side comparison of interface region for HfO_2 devices with raw EELS data after proper background subtraction is shown in figure 5.7. Each color coded and numbered graphical line is an EELS spectrum at a given location on the sample with the corresponding beam spot size indicated in the graphs (note that 5 nm regions parallel to the SiGe surface are averaged). By tracing the Si K edge at 1839 eV and Ge L edges at 1217 eV from SiGe into HfO_2, it is seen at spectrum number 8 that Si and Ge signals decay simultaneously for the control HfO_2 device. In contrast, an earlier Ge decay is seen both in bilayer and NL device at spectrum 8. The only Si peak observed at spectrum line 9 for bilayer and NL devices indicate SiO_x IL formation. The data is consistent with the ozone increasing the Si content of the IL for both the bilayer and NL devices.
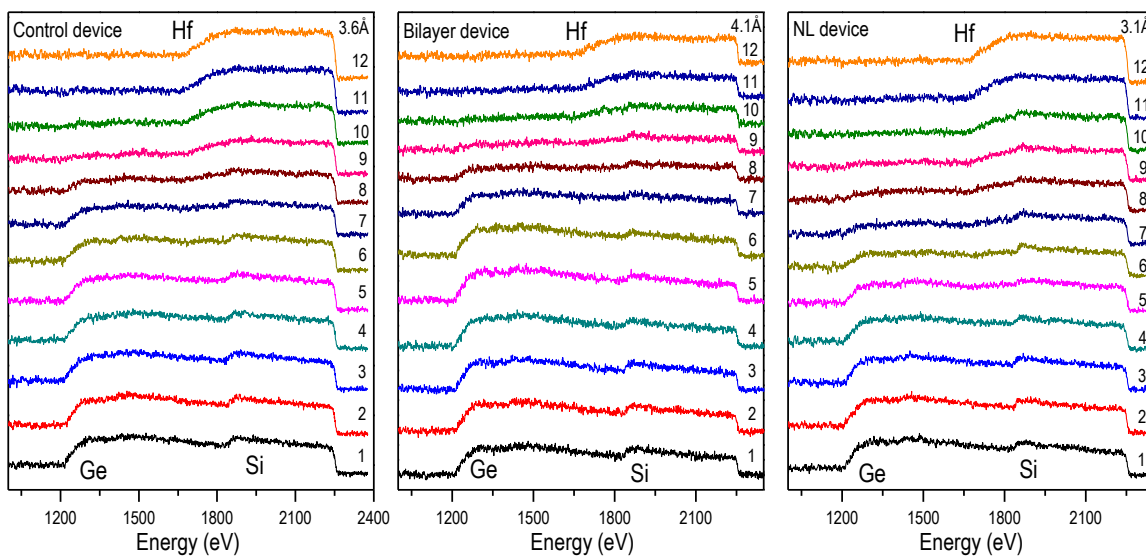
Figure 5.7 STEM-EELS raw data analysis of 9 × (5HfO$_2$ + 5 sec O$_3$) NL device. Raw data from region of interest in figure … shown after background subtraction. To increase the visibility of the peaks, 2D graph of raw EELS data with 1000-2350keV energy loss range is presented in graph below along with data for control and bilayer sample. After background subtraction, offsets were introduced between each curve to improve visibility. In comparison to control device, bilayer and NL devices shows Si peak even after Ge signal decays seen from spectrum lines labeled 7-11.

5.6 Depth Profiling of the MOSCAPs with ER-PES

It is hypothesized that ozone increases the Si content of the IL by depletion of Ge through oxidation of Ge which then diffuses to the surface of the oxides and sublimates. To prove the Ge diffusion hypothesis, ER-PES is employed after full gate oxide deposition since ER-PES has better compositional sensitivity especially for the topmost surface of the sample with low photon energy. ER-PES was chosen over angle resolved PES because ER-PES has fixed small spot experiment geometry, so the oxides could be probed between the metal pads.   In addition, ER-PES is weakly influenced by surface roughness which affects attenuation length due to angular dependence of overlayer thickness in AR-PES[53,83].

Compositions of the gate oxide at selected maximum nominal depth are obtained by monitoring Ge 3d, Hf 4f and Si 2p XPS lines with X-rays tuned to 150eV, 500eV and 1000eV. X-rays at 150 eV probe the topmost layers. The center region of the gate oxide and oxide/SiGe interface are probed with 500 eV and 1 keV X-ray energy, respectively. The Si and Ge composition in HfO_2 and at the interface are quantified using the constant kinetic energy PES method[83]. In this technique, compositional profiling of the same fixed maximum depth for several elements can be studied by tuning the X-ray energy such that the kinetic energies of the photo electrons for all the elements are similar. One of the drawbacks of the constant kinetic energy method is that the photon flux varies with incident kinetic energy. To avoid this issue, in the present study, similar ionization energies are employed for all the critical elements: Hf 4f 7/2 (14.2eV), Ge 3d 5/2 (29.2eV) and Si 2p 3/2 (99.4eV). Therefore, there are negligible differences in the kinetic energy of the photoelectrons (120.8eV versus 135.8eV) from different elements.
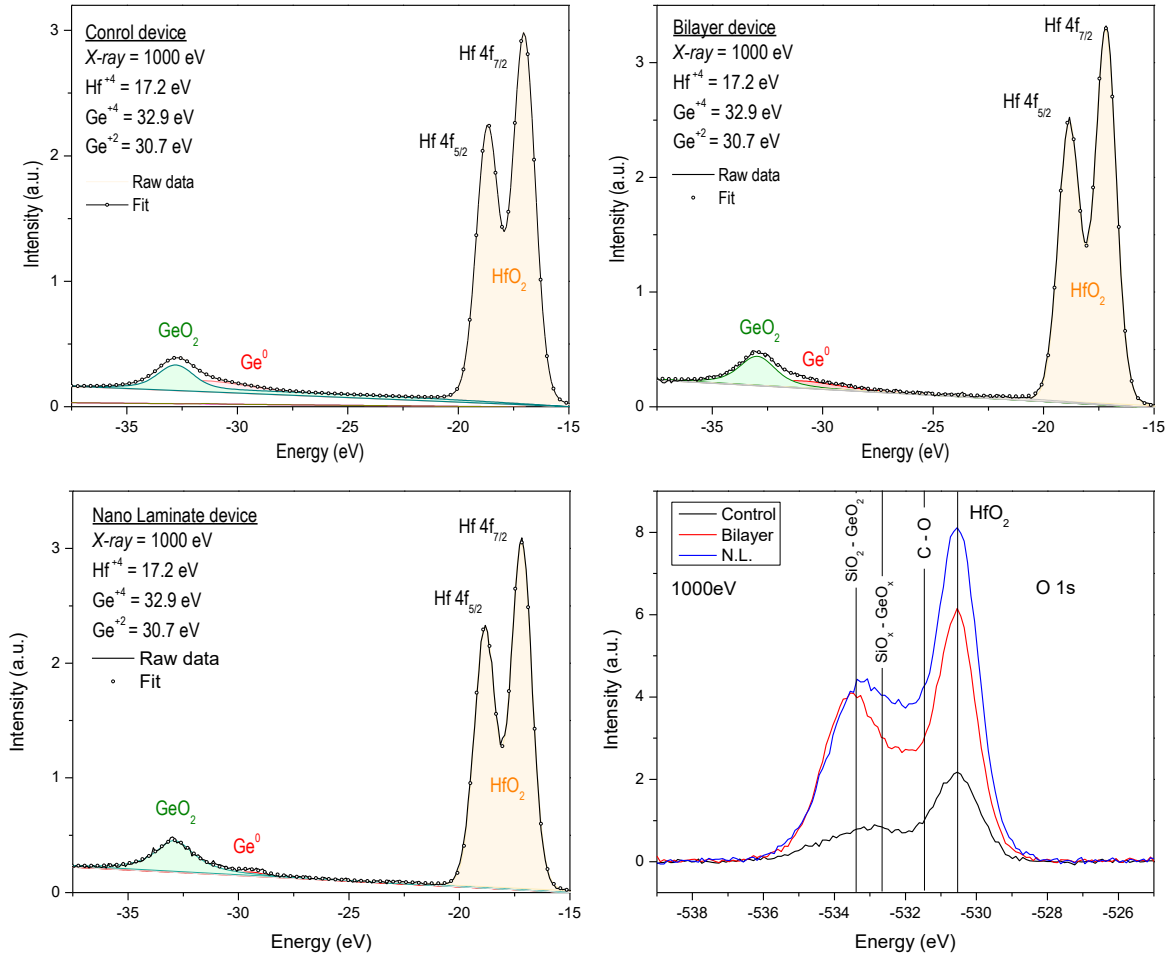
Figure 5.8 PES spectrum of MOSCAPs with 1000 eV Photons. The Ge and Hf spectra for 1000eV photons (λ: 26Å) for (a) 45 ALD cycles of HfO$_2$ control device, (b) the bilayer device with 5 ALD cycles of HfO$_2$ / 60 sec O$_3$ / 40 ALD cycles of HfO$_2$ structure and (c) the nanolaminate with 9 x (5HfO$_2$ + 5 sec O$_3$) ALD cycles devices. The fit for entire spectrum is shown with the raw data in black lines. The colored regions show the fit for the corresponding element. Distinct 1.6eV spin orbit splitting between Hf 4f 7/2 – 5/2 is seen. Metallic Ge^0 at 29 eV are seen for all the devices at 1000eV consistent with probing the SiGe bulk composition since the maximum probe depth is not a delta function. The broad peaks at 32.6eV and at 17.1 eV are defined as GeO$_2$ and HfO$_2$ (Hf^{+4} 7/2). (d) The graphs show O 1s spectrum taken at 1000eV for all devices. The peak located at 530.5eV indicates metal oxides and referred to HfO$_2$. Other peaks can be assigned for different metal oxides as well as several forms of C-O bonds. The peak at 533 is assigned to suboxides of Si or Ge which increase with ozone insertion as seen by comparison of bilayer and nanolaminate in contrast to control device. However, the probe depths for each film differ due to differences in the gate stack thicknesses and compositions; in addition, the interfaces are well past the nominal maximum depth probe cutoff.

Figure 5.8 shows the fits for the PES spectra for 1000 eV photons for the three critical samples: 45 ALD cycles of HfO_2 control device, the bilayer device with 40 ALD cycles of HfO_2/60 sec O_3/5 cycles of HfO_2/SiGe structure, and the nanolaminate device with 9 x (5 sec O_3 + $5HfO_2$)/SiGe ALD cycles. The fit for the entire spectrum is shown with the raw data in black lines. The colored regions show the fit for the corresponding element. Metallic Ge^0 spectral features at 29 eV are seen for all the devices at 1000eV, consistent with probing the SiGe bulk composition since the maximum probe depth is not a delta function. Figure 5.8 d shows the O 1s spectrum taken at 1000eV for all devices. The peak located at 530.5eV indicates metal oxides and results from HfO_2. The peak at 533eV is assigned to suboxides of Si or Ge which increase with ozone insertion as seen by comparison of the bilayer and nanolaminate devices in contrast to the control device. However, the probing depth for each film differs due to differences in the gate stack thicknesses and compositions; in addition, the interfaces are well past the nominal maximum probing depth cutoff. As shown in figure 5.10, it is easier to observe the metallic Si^0 than the metallic Ge^0 peak at 1000 eV photon energy even though both peaks originate from the SiGe substrate and the kinetic energies for these two peaks are similar; this is consistent with the interface being beyond the inelastic mean free path ($\lambda=1$) so there are elastic components with very different sensitivities than the non-scattered component of the signal (i.e the portion governed by λ).
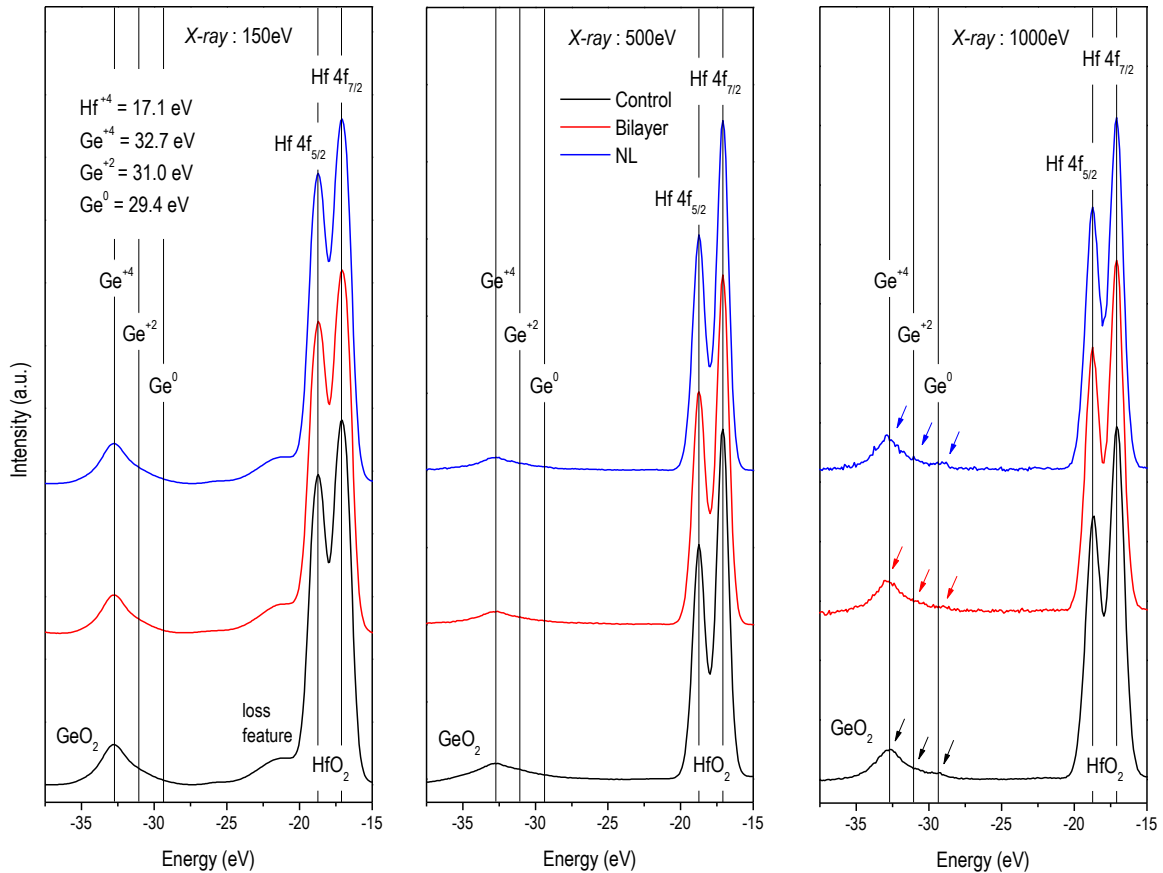
Figure 5.9 Ge and Hf spectrums of MOSCAP devices with ER-PES. Distribution of the Ge and Hf elements across the 45 cycles of HfO_2 control device (black), the bilayer device with 5 ALD cycles of HfO_2 / 60 sec O_3 / 40 ALD cycles of HfO_2 structure (red) and the nanolaminate with 9 x (5HfO_2 + 5 sec O_3) ALD cycles (blue) devices. The Ge 3d and Hf 4f spectra were taken in a single scan and normalized with respect to Hf 4f 7/2 for each energy to obtain relative intensity. Distinct 1.6eV spin orbit splitting between Hf 4f 7/2 – 5/2 is seen. Elements were probed with soft x-rays at 150 eV (λ: 7Å), 500 eV (λ: 17Å) and 1000 eV (λ: 26Å). Metallic Ge^0 at 29 eV are seen for all the devices at 1000eV consistent with probing the SiGe bulk composition. The broad peaks at 32.6eV and at 17.1 eV are defined as GeO_2 and HfO_2 (Hf^{+4} 7/2). All the oxidation states of Ge are indicated with arrows. For all the devices, GeO_x shows similar signal intensity at 150 eV indicating Ge out diffusion from SiGe layer through the HfO_2.

Figure 9 shows the full Ge and Hf PES spectra for the tree critical samples at three photon energies. Metallic Ge^0 at 29 eV are seen for all the devices at 1000eV, consistent with probing the SiGe bulk composition past the nominal maximum probe depth. The broad peaks at 32.7eV and at 17.1 eV are defined as GeO_2 and HfO_2 (Hf^{+4} 7/2). For all the devices, GeO_x shows similar signal intensity at 150 eV indicating Ge out diffusion from SiGe layer through the HfO_2. The GeO_x signal is at a minimum for 500 eV consistent with GeO_x having a higher relative concentration at the surface and at the IL; it is noted that changes in relative sensitivity with photon energy may also may a role in the GeO_x signal being at a minimum at 500 eV.

ER-PES compositional analysis of MOSCAP devices are shown in figure 10 Ge (a) and Si (b). The schematic drawing above the graphs constructed with STEM and EELS-EDS data illustrate the structure and the composition of the samples studied with ER-PES. Metallic Ge^0 at 29eV and Si^0 (3/2) peaks with spin orbit splitting at 99.4eV are seen for all the devices at 1000eV which indicates that the probing depth extends into the SiGe bulk. Broad peaks at 32.6eV and 103.1eV are defined as GeO_2 and SiO_2 respectively[84]. Additional analysis and controls are provided in the supplement. For all the devices, the 150 eV X-ray-energy probed GeO_x shows similar signal intensity for given energy, indicating Ge out diffusion from the SiGe layer through the HfO_2. Conversely, the variation in the Si^{+4} signal among the samples is pronounced. In comparison to the control device, the ozone exposed bilayer and NL samples exhibit higher SiO_2 peaks consistent with enhanced SiO_x IL composition as observed in the EELS samples.
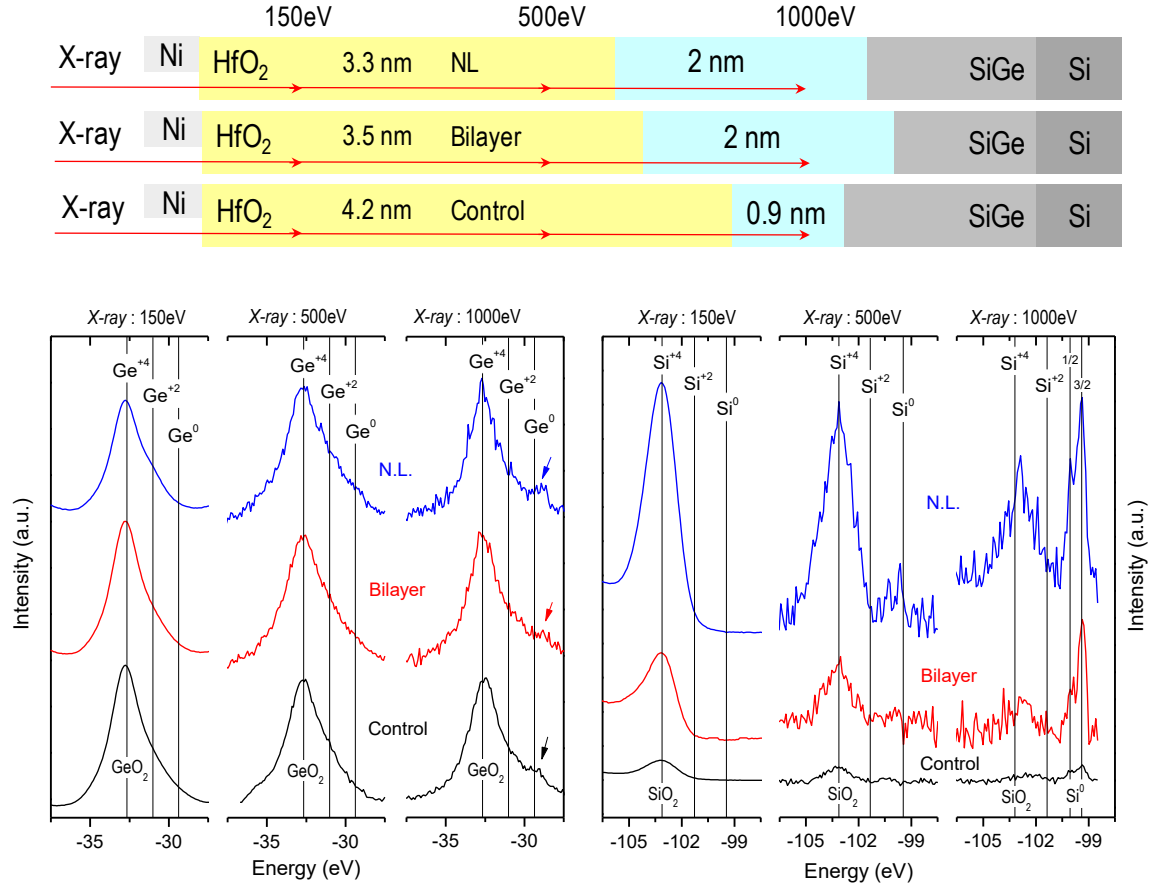
Figure 5.10 Ge and Si depth profiling on MOSCAP devices with ER-PES. The schematic drawing above the graphs constructed with STEM and EELS-EDS data to illustrate the structure and the composition of the samples studied with ER-PES. Distribution of the Si and Ge elements across the 45 cycles of HfO_2 control device (black), the bilayer device with 5 ALD cycles of HfO_2 / 60 sec O_3 / 40 ALD cycles of HfO_2 structure (red) and the nanolaminate with 9 x ($5HfO_2$ + 5 sec O_3) ALD cycles (blue) devices. The Si 2p, Ge 3d and Hf 4f signals were probed with soft x-rays at 150 eV (λ: 7Å), 500 eV (λ: 17Å) and 1000 eV (λ: 26Å). The Ge and Si peaks were normalized respect to Hf 4f spectra for each energy to obtain relative intensity. Metallic Ge^0 at 29 eV and Si^0 (3/2) at 99.4eV are seen for all the devices at 1000eV consistent with the SiGe bulk. The broad peaks at 32.6eV and 103.1eV are defined as GeO_2 and SiO_2. Ge^{+2} at 31eV and Si^{+2} at 101.3eV are indicated with black lines. For all the devices, the 150 eV GeO_x shows similar signal intensity for given energy indicating Ge out diffusion from SiGe layer through the HfO_2. Conversely, the variation in Si^{+4} signal among the samples is pronounced. For the 1000 eV data, in comparison to the control device, the elemental Si composition is higher for bilayer and NL device consistent with depletion of Ge from interface region and Si rich SiGe surface.

5.7 Conclusion

Kinetics of Ge diffusion into gate oxides and GeO desorption from the oxide surface are well-documented[15,19,61,86]. Kita et al and others report formation of volatile GeO due to oxidation of Ge at the interface of SiGe which diffuses through the gate oxide and desorbs from the surface as GeO[16,18,19]. Unlike SiO desorption from surfaces at high temperature (standard sublimation temperature ~780C), sublimation of GeO occurs at low temperature (standard sublimation temperature ~ 400C)[18,20]. GeO_x formation can induce significant Ge consumption from interface[16,17]. In addition, it has been shown that high pressure oxygen can suppress GeO desorption by forming relatively stable GeO_2 at the surface which is the underlying mechanism for the high quality IL on Ge substrates[4,79,80]; therefore GeO desorption can be enhanced at low pressure due transformation from GeO_2 into volatile GeO in an oxygen deficient environment[18,19]. The standard Gibbs free energy of Si oxidation is higher than that for Ge but for very reactive oxidants, such as atomic O, this difference may be less important. In sum, the Ge out-diffusion into the gate oxide and GeO desorption from the system can be controlled by tuning temperature, oxidant type, and oxidant concentration.

It is hypothesized that interface defect reduction by ozone insertion into HfO_2 gate is primarily induced by enhancement of GeO formation, followed by GeO diffusion through the gate oxide and sublimation of GeO from the gate oxide surface. This process can deplete Ge from SiGe top layer and forms a Si rich SiGe surface consistent with STEM-EELS data showing an Si rich IL and 150 eV ER-PES showing surface GeO_x. This process is Ge selective due to the difference in activation energy for GeO desorption and diffusion and the propensity of SiO_x to form a silicate instead of desorbing from gate oxides[20,58,87].

Al_2O_3 only gate oxide growth on SiGe is very effective for D_{it} reduction as a result of remote oxygen scavenging from interface and selectively reducing GeO_x, which is the primary source of interface defects. This process is driven by the highly oxygen reactive Al_2O_3 precursor, TMA, and differences in formation enthalpy of GeO_x and SiO_x; the defect reduction occurs by excess TMA diffusing into the oxide and reducing interface defects via oxygen scavenging. For ozone insertion into Al_2O_3, there are two complementary mechanisms to reduce D_{it}: 1) ozone selectively depletes Ge from the SiGe surface leaving an Si rich interface, while 2) Al_2O_3 ALD selectively scavenges oxygen from Ge which reduces the IL thickness and forms an ultra-low defect density (D_{it} 3.2×10^{11} $cm^{-2}eV^{-1}$) Al_2O_3 / SiGe interface. Ozone insertion into bilayer HfO_2-Al_2O_3/SiGe is not as effective as ozone insertion into only HfO_2/SiGe devices; this is consistent with the Al_2O_3 in the bilayer already partially decreasing the interfacial GeO_x and reducing the Ge out-diffusion since it is a good diffusion barrier[63].

It is hypothesized that the ozone dosed Al_2O_3 sample had exceptionally low D_{it} because two complementary mechanism of Dit reduction are active: 1) D_{it} reduction with ozone exposure and 2) D_{it} decrease with remote oxygen scavenging via top surface Al_2O_3 ALD. In contrast, for the HfO_2 only device exposed to ozone in figure 5.2, there is only a single D_{it} reduction mechanism.

For HfO_2, the most effective D_{it} reduction with ozone is found when ozone is dispersed into the HfO_2 gate oxide in a nanolaminate structure, consistent with the ozone oxidant continuing to generate interfacial GeO_x and its sublimation during the entire ALD process, thus adding the benefit of a continuous removal of Ge from the interface.

While ALD is usually modeled as a layer by layer process, for gate oxide deposition the data is more consistent with processes in which the interface continuously evolves during ALD and thus requires continuous defect reduction or post deposition defect reduction. This continuous defect reduction can be implemented by using an Al_2O_3/HfO_2 nanolaminate to getter oxygen from GeO_x continuously during ALD, or by using an ozone-HfO_2 nanolaminate to continuously deplete Ge from the IL by GeO sublimation during ALD, or by using a gettering gate to scavenge oxygen from GeO_x after ALD; however, in all cases these processes depend on facile diffusion of oxidants during or post ALD through the gate oxide.

5.8 Supplement

Elastic mean free path for photoelectrons can be longer than inelastic mean free path. For instance, elastic mean free path for electrons with 1285eV kinetic energy in HfO_2 is reported as 6.3 nm[1]. Therefore, the composition the HfO_2-SiGe interface can be probed through even 5 nm of HfO_2 even though the inelastic mean free path (λ) is only 3 nm. For the present experiment, the maximum kinetic energy is slightly less than 1000 eV which as shown in figure 5.1 has a $\lambda = 2.7$ nm but signals from below the 5 nm of oxide can be observed due to both elastic scattering and the fact that the escape probability for inelastically scattered electrons decays exponentially and does not have a sharp cutoff (see figure 5.10).

The intensity of the elemental spectrum is governed by $I = F(E) \times N \times \sigma(E) \times \lambda(E) \times K(E)$ where F = photon flux, N = atomic concentration, σ = scattering cross section, λ = inelastic mean free path, K= transmission function which is the detection efficiency of the energy analyzer[53,54,88]. To avoid complication of quantization due to change in photon flux which is a function of X-ray energy like other variables in the equation, the Si and Ge signal intensities are normalized with respect to the Hf 4f 5/2 signal.

There are a few additional factors which affect the compositional sensitivity for EELS and PES: (1) PES compositional sensitivity (~0.01% in ideal experiment) is 10× better than EELS (~0.1% in the ideal experiment); (2) overlapping edges of elements such as Si K edge and Hf M edge may prevent precise calculation of the composition for EELS data; (3) the sample volume of experiments in EELS is limited to the scanned area so the volume is ~0.0025μ^2 (5×10×50nm) while the sample volume is ~8μ^2 (0.005×40×40μm) for the PES

experiment, therefore the sensitivity of the PES experiment can be as high as $< \sim 1\%$ Ge or Si concentration in HfO_2; (4) While PES is a nondestructive method with high photon flux providing high spectrum intensity, the EELS signal is limited by low electron exposure to prevent beam damage on sample. However, PES has two severe limitations: (1) EELS only collects data at a fixed distance from the surface and only integrates the composition in the direction parallel to the semiconductor – oxide interface surface; therefore, the resolution in z (the direction perpendicular to the surface is mainly limited by just surface roughness. In contrast, PES inherently integrates between the nominal maximum probe depth and the surface of the oxide; (2) In PES, there is a theoretical maximum probe depth, but this is an oversimplification since it is material dependent and the probe sensitivity exponentially decays.

5.9 Acknowledgement

Chapter VI

Conclusion and Future Perspective

1) Elimination of defects at the oxide - SiGe interface by selective oxygen scavenging using highly oxygen reactive metal gettering gates has been shown. Low defect interface formation with a few monolayers of SiO on SiGe was demonstrated. The results suggest that gettering gates selectively scavenge oxygen from GeO_x due to low formation enthalpy in comparison to SiO_x. This process forms thinner interlayers which contains less GeO_x thereby reduces interface defects. The extremely thin interface with ultra-low defect densities between $SiGe/HfO_2$ proves that a thick IL is not necessary for low D_{it} devices.

2) Oxygen scavenging can be performed remotely away from the interface by using diffusion barriers to prevent decrease in total capacitance due to an increase in total gate oxide thickness. Lower interface defect formation with remote Pd/Ti/TiN gettering gates are induced by Si-rich interlayer shown by STEM-EELS analysis. While direct gettering Al-gated devices exhibited a C_{max} reduction due to formation of Al_2O_3 in contact with HfO_2, the Pd/Ti/TiN gated device exhibited a C_{max} enhancement as the oxidized metal layer (TiO_x) was separated from HfO_2 by a conductive diffusion barrier.

3) The mechanism for low defect interface formation with Al_2O_3 in comparison to HfO_2 gate dielectric was investigated. Oxygen scavenging induced by ALD precursor, TMA is the main reason for superior defect reduction in gate oxide constitutes of Al_2O_3 layers. During each TMA half cycle of Al_2O_3 ALD, TMA is dosed in excess

118

to provide sufficient TMA for reduction of additional chemical species after the surface hydroxyl groups are eliminated. This approach utilizes the difference in the heat of formation of SiO_x and GeO_x, achieving lower interface trap densities at the high-k / SiGe interface. Novel gate oxide structures were developed which suppress electronic defects at high-k/SiGe interfaces by employing an oxygen scavenging by TMA. Insertion of Al_2O_3 into the HfO_2 gate oxide removes a GeO_x component of the interlayer between the channel and the deposited gate dielectric oxides, and suggests that effective oxygen scavenging can be achieved with TMA exposure during ALD. This TMA based oxygen scavenging technique is most effective when the Al_2O_3 layers are uniformly distributed across the HfO_2 in a nanolaminate structure, but it also is effective when the Al_2O_3 ALD deposition occurs on top of the HfO_2. Although metallic Al remains more effective at oxygen scavenging, deposition of metallic Al on the gate oxide induces a much larger C_{max} reduction, demonstrating the benefit of TMA remote oxygen scavenging.

4) Elimination of electronic defects with selective surface oxidation between oxide and SiGe interface by ozone insertion into gate oxide was demonstrated. Experiments show enhancement of Si interface composition with ozone insertion into gate oxide. The mechanism hypothesized to be formation of GeO by ozone followed by GeO diffusion through the gate oxide and sublimation of GeO from the gate oxide surface. This process can deplete Ge from SiGe top layer and forms Si rich SiGe surface. It is Ge selective due to difference in activation energy for GeO desorption and diffusion and the propensity of SiO_x to form a silicate instead of desorbing from gate oxides[20,58,87].

Discovery of ferroelectricity in HfO_2 received significant attention due to several immediate applications such as optical modulators, ferroelectric (FE) memory devices due to its scalability and ease of process integration into CMOS[89]. Because of high intrinsic carrier mobility and tunability of the bandgap, SiGe based ferroelectric devices would be preferred to Si based devices once the low defect interfaces can be formed between SiGe and ferroelectric oxides. The techniques developed for dielectric oxide / SiGe interface in this dissertation can be used to eliminate interface defects due to similar chemistry of the dielectric and ferroelectric HfO_2. Several preliminary experiments were performed to investigate this idea in Zr doped HO_2 ferroelectric oxide with novel hetero oxide growth method from single source mixture of $HfCl_4$ and $ZrCl_4$ (HZO) precursor.

Stabilization of ferroelectricity in HfO_2 obtained via doping several elements such as Al, Y, Gd, Si was shown in previous reports with narrow dopant composition window[90]. Conversely, Zr doped HfO_2 or ZrO_2-HfO_2 (HZO) solid mixtures have shown to induce ferroelectricity in broad stoichiometry range[91]. The variation of composition window for stabilization of ferroelectricity in HfO_2 is lock of explanation and furthermore, how small the grains can be while sustaining FE state is still mystery. The latter is critical for device applications especially in CMOS transistors which requires <20 angstrom thick gate oxides. Alternated dosing from separate dopant (Al, Ga, Si, Zr) and HfO_2 ALD precursor sources to form a nanolaminate solid solution to induce FE state in HfO_2 is common technique. However, the alternating precursor process brings complications for oxygen sensitive substrates such as SiGe in which interfacial defect control becomes challenging since each precursor (especially oxidants) has an optimal pulse time for interface defects (D_{it}) minimization. Alternative fabrication technique for FE HfO_2 was investigated in preliminary

experiments in which a single source mixture of HfCl$_4$ and ZrCl$_4$ (HZO) was used; the technique relies upon the vapor phase composition being a simple function of the solid-state composition.
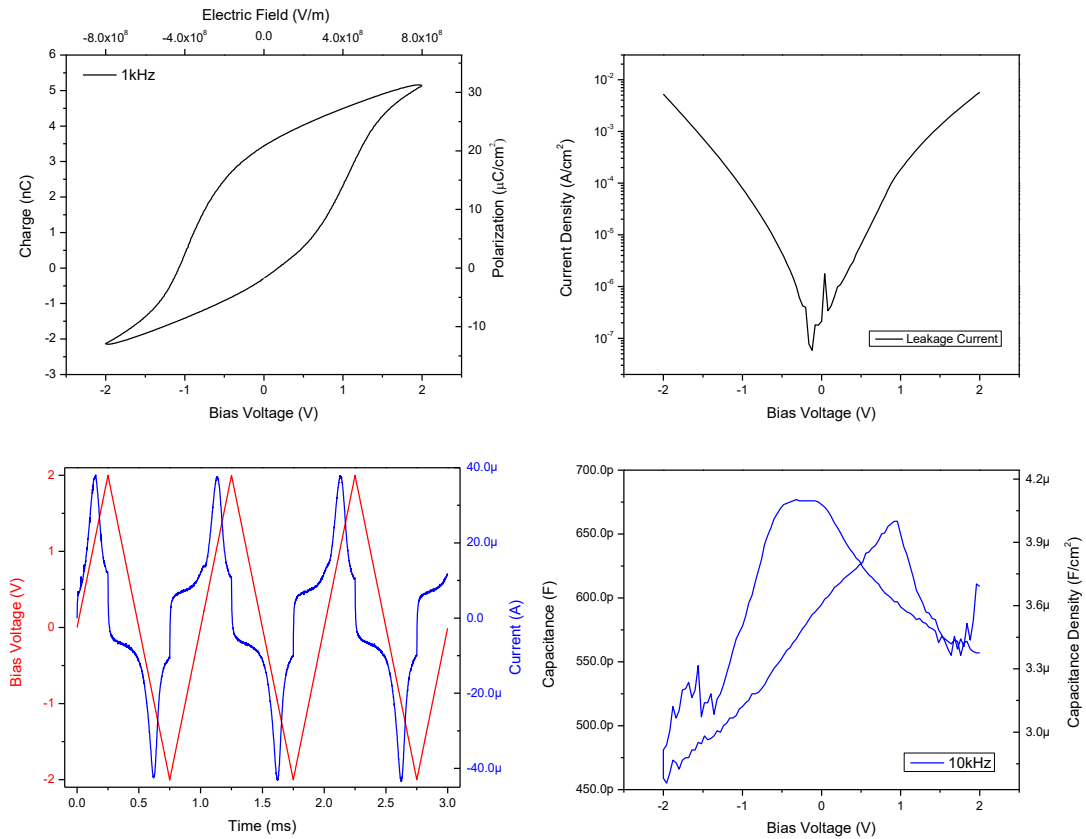
Figure 6.1 Electrical analysis of the Ni / Hf$_x$Zr$_x$O$_x$ / TiN / Si device. (a) FE hysteresis of the device obtained with integrated current from triangular pulse at 1kHz. (b) Low leakage current of $5x10^{-5}$ (A/cm^2) across the FE oxide was obtained. (c) Triangular voltage pulse at 1kHz (red) and corresponding current response obtained from the device indicates FE behavior where the current lacks behind the voltage. (d) Capacitance characteristic of the FE device between -2V to 2V. Nonlinear characteristics is seen rises from change in polarization state by applied bias.
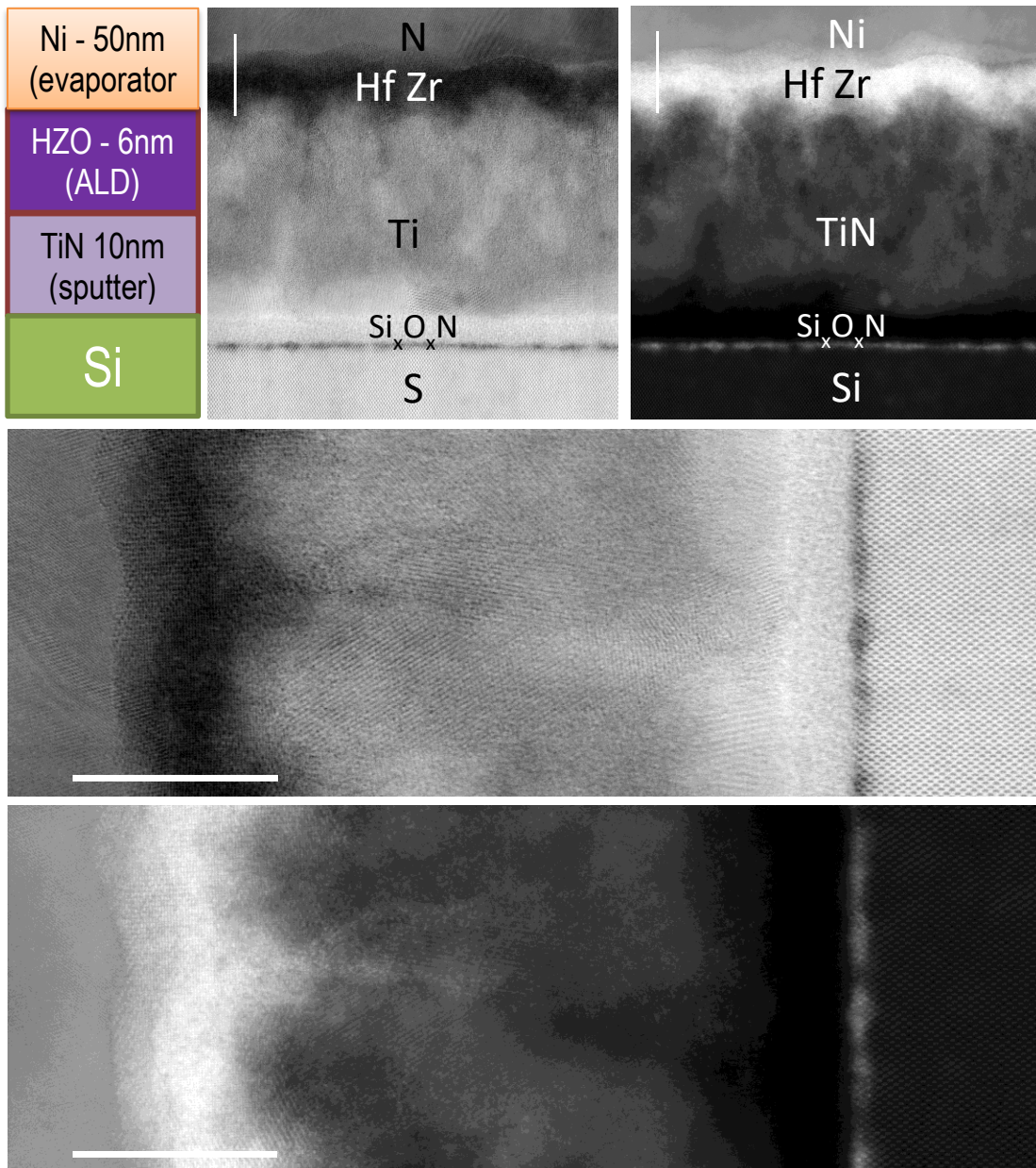
Figure 6.2 Structure and STEM analysis of Ni / Hf$_x$Zr$_x$O$_x$ / TiN / Si device. (a) Schematics of Ni / Hf$_x$Zr$_x$O$_x$ / TiN / Si device. (b-e) BF and HADAAF STEM image of the device. Sputtered TiN forms rough surface prior to ALD grown HZO. Repeated pattern of polycrystalline HfZrO$_2$ layers is seen. In some areas, it follows the pattern from TiN-Si substrate and Ni crystal in other locations.
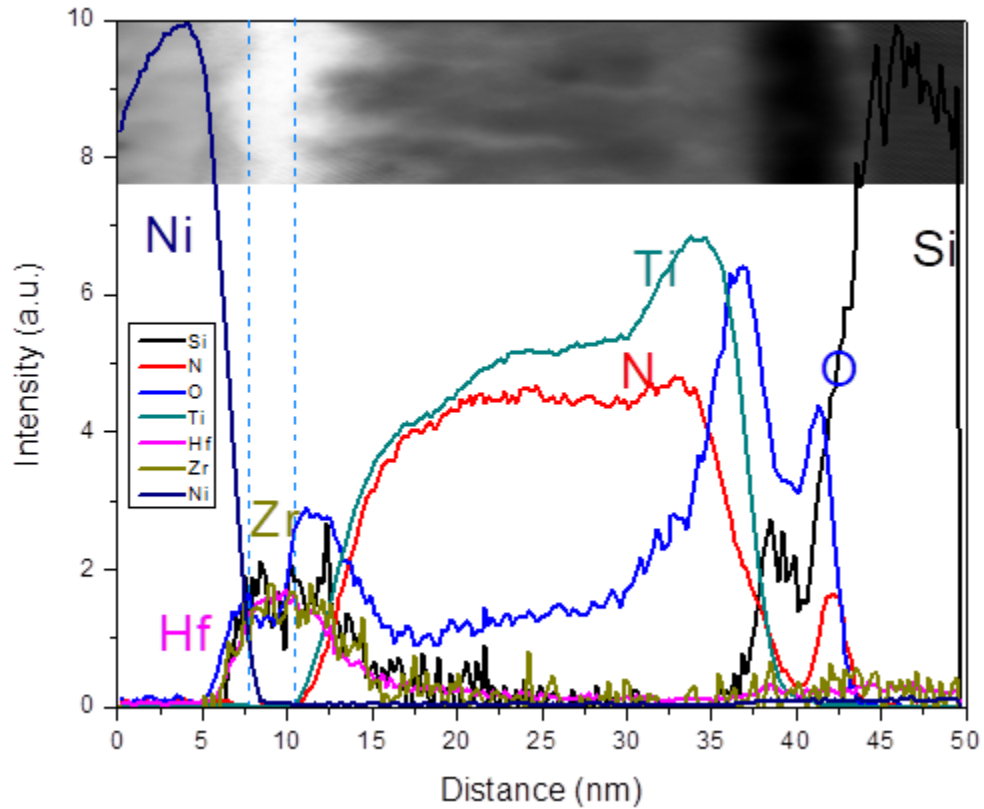
Figure 6.3 STEM EELS analysis of Ni/HfZrO₂/TiN/Si MIM capacitor. In this STEM image, the z contrast coincides with the EELS compositional analysis of the elements. The intermixing between the FE HfZrO₂ and TiN-Ni electrodes is seen.
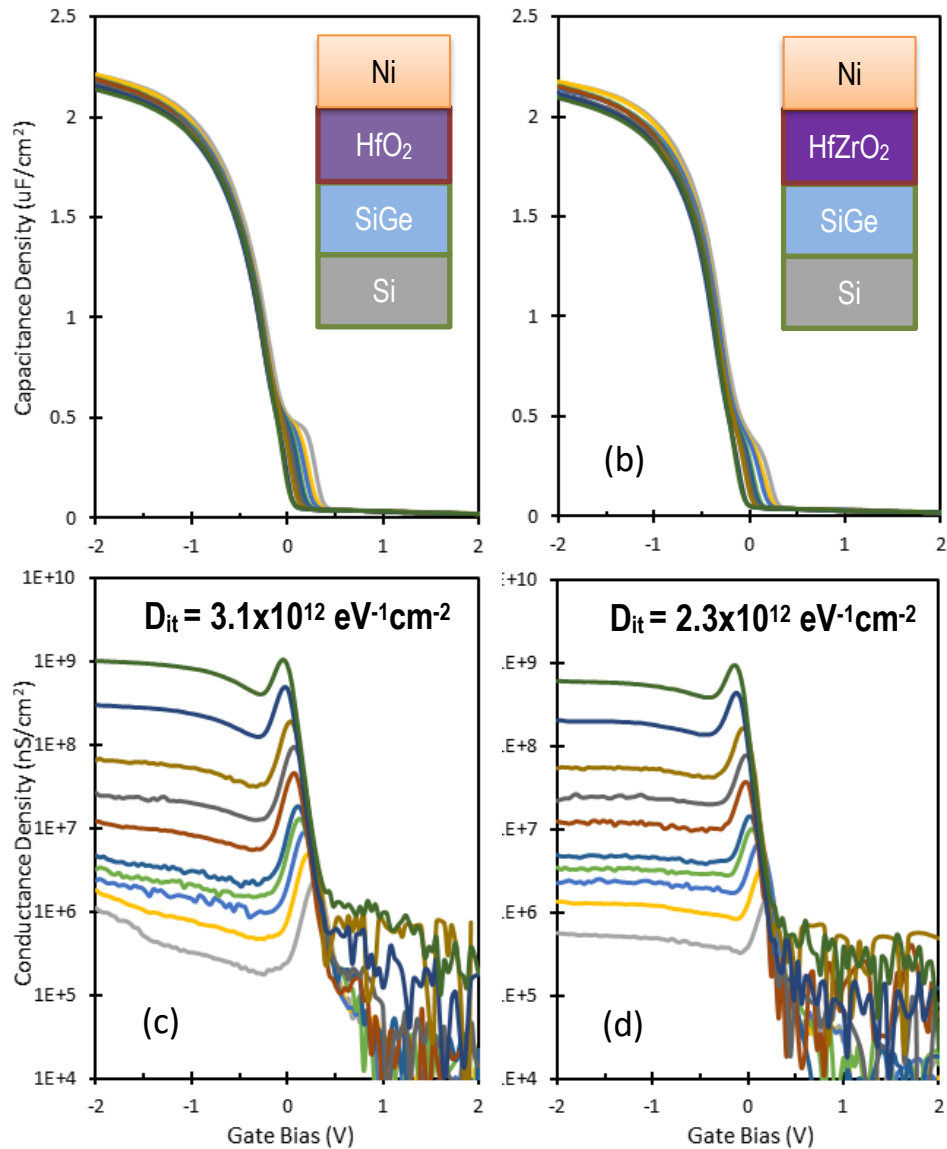
Figure 6.4 C-V and G-V graphs of MOSCAPs with HfO$_2$ and HfZrO$_2$ (from 10 kHz to 1 MHz) Insets in C-V graph illustrate device structures. MOSCAP device with HfO$_2$ and HfZrO$_2$ gate oxide exhibit very similar depletion capacitance and corresponding conductance peak indicates similar defect density obtained at the SiGe/oxide interface. Inset peak D$_{it}$ values were calculated with the conductance model confirms the very similar interface defects formation in both devices.

The ferroelectric properties were investigated in a MIM structure with TiN and Ni electrode and high remnant polarization of 25uC/cm^2 was obtained as shown in figure 6.1. Structural and compositional analysis with STEM-EELS showed polycrystalline HfZrO$_4$ FE oxide intermixing at the interfaces with Ni and TiN as seen in figure 6.2 and 6.3.

Interface defects investigated with MOSCAPs of HfZrO$_2$ oxide on Si$_{0.3}$Ge$_{0.7}$ (100) which is fabricated from single source precursor. Accumulation and depletion capacitance are almost identical to the characteristics of pure HfO$_2$ control devices on Si$_{0.3}$Ge$_{0.7}$ (001) as shown in figure 6.4. This result indicates the similar low defect interface formation between oxide and ferroelectric HfO$_2$ grown on SiGe. Therefore, the methods developed for elimination of the interface defects on oxide / SiGe interface can be applied to ferroelectric HfO$_2$ / SiGe interface.

References

1   Powell, C. J. & Jablonski, A. Dependence of calculated electron effective attenuation lengths on transport mean free paths obtained from two atomic potentials. *Surface and Interface Analysis* **38**, 1348-1356, doi:doi:10.1002/sia.2460 (2006).

2   2.0, I. T. R. f. S. International Technology Roadmap for Semiconductors 2.0. (2015).

3   Hashemi, P. *et al.* in *2014 IEEE International Electron Devices Meeting.* 16.11.11-16.11.14.

4   Ando, T. *et al.* High Mobility High-Ge-Content SiGe PMOSFETs Using Al2O3/HfO2 Stacks with In-Situ O3 Treatment. *IEEE Electron Device Letters* **38**, 303-305, doi:10.1109/LED.2017.2654485 (2017).

5   Lu, D. Silicon Germanium FinFET Device Physics, Process Integration and Modeling Considerations. *ECS Transactions* **64**, 337-345, doi:10.1149/06406.0337ecst (2014).

6   Zhang, L. *et al.* Interface Engineering for Atomic Layer Deposited Alumina Gate Dielectric on SiGe Substrates. *ACS Applied Materials & Interfaces* **8**, 19110-19118, doi:10.1021/acsami.6b03331 (2016).

7   LeGoues, F. K., Rosenberg, R., Nguyen, T., Himpsel, F. & Meyerson, B. S. Oxidation studies of SiGe. *Journal of Applied Physics* **65**, 1724-1728, doi:10.1063/1.342945 (1989).

8   Chagarov, E. A., Kavrik, M. S., Fang, Z., Tsai, W. & Kummel, A. C. Density-functional theory molecular dynamics simulations of a-HfO2/a-SiO2/SiGe and a-HfO2/a-SiO2/Ge with a-SiO2 and a-SiO suboxide interfacial layers. *Applied Surface Science* **443**, 644-654, doi:https://doi.org/10.1016/j.apsusc.2018.02.041 (2018).

9   Cho, M.-H. *et al.* Interfacial characteristics of HfO2 films grown on strained Si0.7Ge0.3 by atomic-layer deposition. *Applied Physics Letters* **84**, 1171-1173, doi:10.1063/1.1647703 (2004).

10   Mitard, J. *et al.* in *2010 International Electron Devices Meeting.* 10.16.11-10.16.14.

11   Sardashti, K. *et al.* Nitride passivation of the interface between high-k dielectrics and SiGe. *Applied Physics Letters* **108**, 011604, doi:10.1063/1.4939460 (2016).

12   Huang, J. *et al.* Surface NH3 anneal on strained Si0.5Ge0.5 for metal-oxide-semiconductor applications with HfO2 as gate dielectric. *Applied Physics Letters* **88**, 143506, doi:10.1063/1.2191468 (2006).

13   Sardashti, K. *et al.* Sulfur passivation for the formation of Si-terminated Al2O3/SiGe(001) interfaces. *Applied Surface Science* **366**, 455-463, doi:https://doi.org/10.1016/j.apsusc.2016.01.123 (2016).

14   Cho, M. H. *et al.* Interfacial characteristics of HfO2 films grown on strained Si0.7Ge0.3 by atomic-layer deposition. *Applied Physics Letters* **84**, 1171-1173, doi:10.1063/1.1647703 (2004).

15   Lu, N. *et al.* Ge diffusion in Ge metal oxide semiconductor with chemical vapor deposition HfO2 dielectric. *Applied Physics Letters* **87**, 051922, doi:10.1063/1.2001757 (2005).

16   Oh, J. & Campbell, J. C. Thermal desorption of Ge native oxides and the loss of Ge from the surface. *Journal of Electronic Materials* **33**, 364-367, doi:10.1007/s11664-004-0144-4 (2004).

17   Wang, S. K. *et al.* Desorption kinetics of GeO from GeO2/Ge structure. *Journal of Applied Physics* **108**, 054104, doi:10.1063/1.3475990 (2010).

18   Hansen, D. A. & Hudson, J. B. The adsorption kinetics of molecular oxygen and the desorption kinetics of GeO on Ge(100). *Surface Science* **292**, 17-32, doi:https://doi.org/10.1016/0039-6028(93)90387-Y (1993).

19   Kita, K. *et al.* in *2009 IEEE International Electron Devices Meeting (IEDM).* 1-4.

20   Prabhakaran, K., Maeda, F., Watanabe, Y. & Ogino, T. Distinctly different thermal decomposition pathways of ultrathin oxide layer on Ge and Si surfaces. *Applied Physics Letters* **76**, 2244-2246, doi:10.1063/1.126309 (2000).

21   Prabhakaran, K. & Ogino, T. Oxidation of Ge(100) and Ge(111) surfaces: an UPS and XPS study. *Surface Science* **325**, 263-271, doi:https://doi.org/10.1016/0039-6028(94)00746-2 (1995).

22   Bardeen, J. Surface States and Rectification at a Metal Semi-Conductor Contact. *Physical Review* **71**, 717-727, doi:10.1103/PhysRev.71.717 (1947).

23   Many, A. & Grover. *Semiconductor surfaces*. (Elsevier, 1965).

24   Garrett, C. G. B. & Brattain, W. H. Physical Theory of Semiconductor Surfaces. *Physical Review* **99**, 376-387, doi:10.1103/PhysRev.99.376 (1955).

25   Taur, Y. & Ning, T. H. *Fundamentals of Modern VLSI Devices*. (Cambridge University Press, 2013).

26   Nicollian, E. H. & Brews, J. R. *MOS (Metal Oxide Semiconductor) Physics and Technology*. (Wiley, 2002).

27   Fleetwood, D. *et al.* Border traps: issues for MOS radiation response and long-term reliability. *Microelectronics Reliability* **35**, 403-428 (1995).

28   Engel-Herbert, R., Hwang, Y. & Stemmer, S. Comparison of methods to quantify interface trap densities at dielectric/III-V semiconductor interfaces. *Journal of Applied Physics* **108**, 124101, doi:doi:http://dx.doi.org/10.1063/1.3520431 (2010).

29   Lin, T. D. *et al.* Realization of high-quality HfO2 on In0.53Ga0.47As by in-situ atomic-layer-deposition. *Applied Physics Letters* **100**, -, doi:doi:http://dx.doi.org/10.1063/1.4706261 (2012).

30   Han-Ping, C. *et al.* Re-examination of the extraction of MOS interface-state density by C – V stretchout and conductance methods. *Semiconductor Science and Technology* **28**, 085008 (2013).

31   Schroder, D. K. *Semiconductor Material and Device Characterization*. (Wiley, 2006).

32   Chagarov, E. A. & Kummel, A. C. in *Fundamentals of III-V Semiconductor MOSFETs*   93-130 (Springer, 2010).

33   Kresse, G. & Furthmüller, J. Efficient iterative schemes for ab initio total-energy calculations using a plane-wave basis set. *Physical Review B* **54**, 11169-11186 (1996).

34   Chagarov, E. A., Porter, L. & Kummel, A. C. Density-functional theory molecular dynamics simulations of a-HfO2/Ge(100)(2 × 1) and a-ZrO2/Ge(100)(2 × 1) interface passivation. *The Journal of Chemical Physics* **144**, 084704, doi:10.1063/1.4941947 (2016).

35   Ceresoli, D. & Vanderbilt, D. Structural and dielectric properties of amorphous h-k oxides: HfO2, ZrO2 and their alloys. *Physical Review B* **74**, 125108 (2006).

36   George, S. M. Atomic Layer Deposition: An Overview. *Chemical Reviews* **110**, 111-131, doi:10.1021/cr900056b (2010).

37   Barna, Á., Pécz, B. & Menyhard, M. TEM sample preparation by ion milling/amorphization. *Micron* **30**, 267-276, doi:https://doi.org/10.1016/S0968-4328(99)00011-6 (1999).

38   Mayer, J., Giannuzzi, L. A., Kamino, T. & Michael, J. TEM Sample Preparation and FIB-Induced Damage. *MRS Bulletin* **32**, 400-407, doi:10.1557/mrs2007.63 (2007).

39   Egerton, R. F. *Electron Energy-Loss Spectroscopy in the Electron Microscope*. (Springer US, 2011).

40   Hillier, J. & Baker, R. F. Microanalysis by Means of Electrons. *Journal of Applied Physics* **15**, 663-675, doi:10.1063/1.1707491 (1944).

41   Haider, M. *et al.* Electron microscopy image enhanced. *Nature* **392**, 768, doi:10.1038/33823 (1998).

42   Nellist, P. *et al.*   159-164.

43   Colliex, P. C. & Jouffrey, B. Diffusion inelastique des electrons dans un solide par excitation de niveaux atomiques profonds. *The Philosophical Magazine: A Journal of Theoretical Experimental and Applied Physics* **25**, 491-511, doi:10.1080/14786437208226818 (1972).

44   Egerton, R. F. A simple electron spectrometer for energy analysis in the transmission microscope. *Ultramicroscopy* **3**, 39-47, doi:https://doi.org/10.1016/S0304-3991(78)80005-9 (1978).

45   Batson, P. E. Simultaneous STEM imaging and electron energy-loss spectroscopy with atomic-column sensitivity. *Nature* **366**, 727, doi:10.1038/366727a0 (1993).

46   Pennycook, S. J. in *Advances in Imaging and Electron Physics* Vol. 123 (eds Peter W. Hawkes, Pier Georgio Merli, Gianluca Calestani, & Marco Vittori-Antisari) 173-206 (Elsevier, 2002).

47   Muller, D. A., Tzou, Y., Raj, R. & Silcox, J. Mapping sp2 and sp3 states of carbon at sub-nanometre spatial resolution. *Nature* **366**, 725, doi:10.1038/366725a0 (1993).

48   Chen, Z. *et al.* Quantitative atomic resolution elemental mapping via absolute-scale energy dispersive X-ray spectroscopy. *Ultramicroscopy* **168**, 7-16, doi:https://doi.org/10.1016/j.ultramic.2016.05.008 (2016).

49   D'Alfonso, A. J., Freitag, B., Klenov, D. & Allen, L. J. Atomic-resolution chemical mapping using energy-dispersive x-ray spectroscopy. *Physical Review B* **81**, 100101, doi:10.1103/PhysRevB.81.100101 (2010).

50   Xu, W., Dycus, J. H., Sang, X. & LeBeau, J. M. A numerical model for multiple detector energy dispersive X-ray spectroscopy in the transmission electron microscope. *Ultramicroscopy* **164**, 51-61, doi:https://doi.org/10.1016/j.ultramic.2016.02.004 (2016).

51   Briggs, D. & Seah, M. P. Practical surface analysis by Auger and X-ray photoelectron spectroscopy. *D. Briggs, & M. P. Seah,(Editors), John Wiley & Sons, Chichester 1983, xiv+ 533* (1983).

52   Hollander, J. M. & Jolly, W. L. X-ray photoelectron spectroscopy. *Accounts of Chemical Research* **3**, 193-200 (1970).

53   Merzlikin, S. V. *et al.* Resolving the depth coordinate in photoelectron spectroscopy – Comparison of excitation energy variation vs. angular-resolved XPS for the analysis of a self-assembled monolayer model system. *Surface Science* **602**, 755-767, doi:https://doi.org/10.1016/j.susc.2007.12.005 (2008).

54   Jablonski, A. & Powell, C. J. Information depth and the mean escape depth in Auger electron spectroscopy and x-ray photoelectron spectroscopy. *Journal of Vacuum Science & Technology A* **21**, 274-283, doi:10.1116/1.1538370 (2003).

55   Nayak, D. K., Kamjoo, K., Park, J. S., Woo, J. C. S. & Wang, K. L. Wet oxidation of GeSi strained layers by rapid thermal processing. *Applied Physics Letters* **57**, 369-371, doi:10.1063/1.103694 (1990).

56   Prabhakaran, K., Maeda, F., Watanabe, Y. & Ogino, T. Thermal decomposition pathway of Ge and Si oxides: observation of a distinct difference. *Thin Solid Films* **369**, 289-292, doi:https://doi.org/10.1016/S0040-6090(00)00881-6 (2000).

57   AlKaabi, K., Prasad, D. L. V. K., Kroll, P., Ashcroft, N. W. & Hoffmann, R. Silicon Monoxide at 1 atm and Elevated Pressures: Crystalline or Amorphous? *Journal of the American Chemical Society* **136**, 3410-3423, doi:10.1021/ja409692c (2014).

58   NIST. NIST Chemistry WebBook, SRD 69. (2017).

59   Kim, H., McIntyre, P. C., On Chui, C., Saraswat, K. C. & Stemmer, S. Engineering chemically abrupt high-k metal oxide∕silicon interfaces using an oxygen-gettering metal overlayer. *Journal of Applied Physics* **96**, 3467-3472, doi:10.1063/1.1776636 (2004).

60   Choi, C. & Lee, J. C. Scaling equivalent oxide thickness with flat band voltage (VFB) modulation using in situ Ti and Hf interposed in a metal/high-k gate stack. *Journal of Applied Physics* **108**, 064107, doi:10.1063/1.3481453 (2010).

61   Hosoi, T. *et al.* Ge diffusion and bonding state change in metal/high-k/Ge gate stacks and its impact on electrical properties. *Microelectronic Engineering* **109**, 137-141, doi:https://doi.org/10.1016/j.mee.2013.03.115 (2013).

62   Wilk, G. D. & Wallace, R. M. Electrical properties of hafnium silicate gate dielectrics deposited directly on silicon. *Applied Physics Letters* **74**, 2854-2856, doi:10.1063/1.124036 (1999).

63   Ogawa, S. *et al.* Insights into thermal diffusion of germanium and oxygen atoms in HfO2/GeO2/Ge gate stacks and their suppressed reaction with atomically thin AlOx interlayers. *Journal of Applied Physics* **118**, 235704, doi:10.1063/1.4937573 (2015).

64   E. H. Nicollian, J. R. B. *MOS (Metal Oxide Semiconductor) Physics and Technology*. (Wiley-Interscience, 1982).

65   Yuan, Y. *et al.* A Distributed Bulk-Oxide Trap Model for Al2O3 InGaAs MOS Devices. *IEEE Transactions on Electron Devices* **59**, 2100-2106, doi:10.1109/TED.2012.2197000 (2012).

66   Campbell, T. *et al.* Dynamics of Oxidation of Aluminum Nanoclusters using Variable Charge Molecular-Dynamics Simulations on Parallel Computers. *Physical Review Letters* **82**, 4866-4869 (1999).

67   Asahara, R. *et al.* Comprehensive study and design of scaled metal/high-k/Ge gate stacks with ultrathin aluminum oxide interlayers. *Applied Physics Letters* **106**, 233503, doi:10.1063/1.4922447 (2015).

68   Chen, H. P. *et al.* Interface-State Modeling of Al2O3 InGaAs MOS From Depletion to Inversion. *IEEE Transactions on Electron Devices* **59**, 2383-2389, doi:10.1109/TED.2012.2205255 (2012).

69   Choong Hyun, L. *et al.* Ge/GeO 2 Interface Control with High-Pressure Oxidation for Improving Electrical Characteristics. *Applied Physics Express* **2**, 071404 (2009).

70   Zhang, Q. *et al.* Germanium Incorporation in HfO2 Dielectric on Germanium Substrate. *Journal of The Electrochemical Society* **153**, G207-G210, doi:10.1149/1.2160432 (2006).

71   Kwak, I. *et al.* HfO2/Al2O3 Nanolaminate on Si0.7Ge0.3(100) Surface by Thermal Atomic Layer Deposition. *Meeting Abstracts* **MA2018-02**, 1080 (2018).

72   Kavrik, M. S. *et al.* Ultralow Defect Density at Sub-0.5 nm HfO2/SiGe Interfaces via Selective Oxygen Scavenging. *ACS Applied Materials & Interfaces* **10**, 30794-30802, doi:10.1021/acsami.8b06547 (2018).

73   Hua, W. *et al.* Ge outdiffusion effect on flicker noise in strained-Si nMOSFETs. *IEEE Electron Device Letters* **25**, 693-695, doi:10.1109/LED.2004.834884 (2004).

74   Hinkle, C. L. *et al.* GaAs interfacial self-cleaning by atomic layer deposition. *Applied Physics Letters* **92**, 071901, doi:10.1063/1.2883956 (2008).

75   Milojevic, M., Contreras-Guerrero, R., Lopez-Lopez, M., Kim, J. & Wallace, R. M. Characterization of the "clean-up" of the oxidized Ge(100) surface by atomic layer deposition. *Applied Physics Letters* **95**, 212902, doi:10.1063/1.3268449 (2009).

76   Leapman, R. D. & Swyt, C. R. Separation of overlapping core edges in electron energy loss spectra by multiple-least-squares fitting. *Ultramicroscopy* **26**, 393-403, doi:https://doi.org/10.1016/0304-3991(88)90239-2 (1988).

77   Nan, J. Electron beam damage in oxides: a review. *Reports on Progress in Physics* **79**, 016501 (2016).

78   Reed, T. B. Free energy of formation of binary compounds: an atlas of charts for high-temperature chemical calculations. *MIT Press [1971]* (1971).

79   Zhang, R., Iwasaki, T., Taoka, N., Takenaka, M. & Takagi, S. in *2011 Symposium on VLSI Technology - Digest of Technical Papers.* 56-57.

80   Mukhopadhyay, M., Ray, S. K., Maiti, C. K., Nayak, D. K. & Shiraki, Y. Electrical properties of oxides grown on strained SiGe layer at low temperatures in a microwave oxygen plasma. *Applied Physics Letters* **65**, 895-897, doi:10.1063/1.112193 (1994).

81   Satake, T. *et al.* Auger electron, electron energy loss, secondary electron emission and secondary ion mass spectroscopic studies on the oxidation of hafnium at room temperature. *Journal of the Chemical Society, Faraday Transactions* **89**, 3611-3618, doi:10.1039/FT9938903611 (1993).

82   Iacona, F., Kelly, R. & Marletta, G. X-ray photoelectron spectroscopy study of bombardment-induced compositional changes in ZrO2, SiO2, and ZrSiO4. *Journal of Vacuum Science & Technology A* **17**, 2771-2778, doi:10.1116/1.581943 (1999).

83   Girard-Lauriault, P.-L., Gross, T., Lippitz, A. & Unger, W. E. S. Chemical and Elemental Depth Profiling of Very Thin Organic Layers by Constant Kinetic Energy XPS: A New Synchrotron XPS Analysis Strategy. *Analytical Chemistry* **84**, 5984-5991, doi:10.1021/ac300585q (2012).

84   Schmeisser, D. *et al.* Surface oxidation states of germanium. *Surface Science* **172**, 455-465, doi:https://doi.org/10.1016/0039-6028(86)90767-3 (1986).

85   Morant, C., Galán, L. & Sanz, J. M. An XPS study of the initial stages of oxidation of hafnium. *Surface and Interface Analysis* **16**, 304-308, doi:doi:10.1002/sia.740160163 (1990).

86   Oniki, Y., Koumo, H., Iwazaki, Y. & Ueno, T. Evaluation of GeO desorption behavior in the metal/GeO2/Ge structure and its improvement of the electrical characteristics. *Journal of Applied Physics* **107**, 124113, doi:10.1063/1.3452367 (2010).

87   Uematsu, M. Self-diffusion and impurity diffusion in silicon dioxide. *Journal of Phase Equilibria and Diffusion* **26**, 547-554, doi:10.1007/s11669-005-0049-9 (2005).

88   Jablonski, A. & Powell, C. J. Effective attenuation lengths for quantitative determination of surface composition by Auger-electron spectroscopy and X-ray photoelectron spectroscopy. *Journal of Electron Spectroscopy and Related Phenomena* **218**, 1-12, doi:https://doi.org/10.1016/j.elspec.2017.04.008 (2017).

89   Böscke, T. S., Müller, J., Bräuhaus, D., Schröder, U. & Böttger, U. in *2011 International Electron Devices Meeting.* 24.25.21-24.25.24.

90   Martin, D. *et al.* Ferroelectricity in Si-Doped HfO2 Revealed: A Binary Lead-Free Ferroelectric. *Advanced Materials* **26**, 8198-8202, doi:doi:10.1002/adma.201403115 (2014).

91   Müller, J. *et al.* Ferroelectricity in Simple Binary ZrO2 and HfO2. *Nano Letters* **12**, 4318-4323, doi:10.1021/nl302049k (2012).